CHALMERS
UNIVERSITY OF TECHNOLOGY

Spaceborne Signals of Opportunity for Reflectometry and Scatterometry

An overview study with experimental results of an implemented passive reflectometry system using Ku-band TV-DBS opportunity signals indicating soil moisture measurement prospects

Master's thesis in Communication Engineering

PATRIK BENNET
FRANS-ERIK ISAKSSON

Department of Space, Earth and Environment
CHALMERS UNIVERSITY OF TECHNOLOGY
Gothenburg, Sweden 2020

Master's thesis 2020

Spaceborne Signals of Opportunity for Reflectometry and Scatterometry

An overview study with experimental results of an implemented passive reflectometry system using Ku-band TV-DBS opportunity signals indicating soil moisture measurement prospects

PATRIK BENNET
FRANS-ERIK ISAKSSON

CHALMERS
UNIVERSITY OF TECHNOLOGY

Department of Space, Earth and Environment
Chalmers University of Technology
Gothenburg, Sweden 2020

Spaceborne Signals of Opportunity for Reflectometry and Scatterometry
An overview study with experimental results of an implemented passive reflectometry system using Ku-band TV-DBS opportunity signals indicating soil moisture measurement prospects
PATRIK BENNET
FRANS-ERIK ISAKSSON

Supervisor: Jacob Christensen, RUAG Space Gothenburg
Examiner: Rüdiger Haas, Department of Space, Earth and Environment

Department of Space, Earth and Environment
Chalmers University of Technology
SE-412 96 Gothenburg
Telephone +46 31 772 1000

Cover: Mega-constellations showing thousands of low Earth orbit satellites providing many opportunity signal candidates for passive reflectometry and scatterometry Earth observations. **© ESA - ScienceOffice** [1]

Typeset in LaTeX
Gothenburg, Sweden 2020

Spaceborne Signals of Opportunity for Reflectometry and Scatterometry
An overview study with experimental results of an implemented passive reflectometry system using Ku-band TV-DBS opportunity signals indicating soil moisture measurement prospects

PATRIK BENNET
FRANS-ERIK ISAKSSON
Department of Space, Earth and Environment
Chalmers University of Technology

Abstract

This master's thesis is carried out in two main parts. The first part is a compilation of literature studies of the general passive reflectometry and scatterometry principles, techniques, capabilities and needs. The second part, motivated by arguing the results of the previous, consists of an implemented agriculture soil moisture PAssive Reflectometry and Interferometry System (PARIS) experiment using Ku-band TV Direct Broadcasting Satellite (TV-DBS) opportunity signals. It includes the definition of the experiment setup as well as the derivation of a system model indicating the expected performance. It also covers the process of designing, implementing and verifying the PARIS RF hardware front-end and signal processing software, generating the Delay-Doppler Map (DDM) measurement results. The experiment was performed at the World Heritage Grimeton Radio Station where the PARIS was installed at 120 meters height in an antenna tower overlooking the surrounding agriculture. The results show that the Ku-band TV-DBS PARIS is able to clearly detect the signal at all four measurement areas investigated, even when that differs from the expected region of specular reflection. The measurements Signal-to-Noise Ratio (SNR) varies in between about 10 to 24 dB, while the system model expect it to be exponentially distributed around 18.5 dB. The signal scattering is concluded to consist of both significant specular and diffuse parts, possibly allowing for simultaneous measurements of the the whole system antenna beam coverage area independent of the direction of observation. Future prospects of a Ku-band TV-DBS soil moisture PARIS is extrapolated from the experiment results and discussed, with focus put on three thought products - a stationary installation overlooking agriculture, a drone-carried monitoring system as well as a Low-Earth Orbit (LEO) small satellite Earth Observation (EO) constellation.

Keywords: Remote sensing, passive reflectometry, passive scatterometry, spaceborne signals of opportunity, SOOP, soil moisture measurement, passive reflectometry and interferometry system, PARIS, Earth observation, EO, Ku-band reflectometry, TV-DBS opportunity signals, delay-Doppler map, DDM.

Acknowledgements

For various reasons this project have required us to include and involve many people, be it for guidance, sponsorship, help understanding or practical help. This section is made to give credits to those who helped us by contributing in some way and give them a special thanks.

Starting out where we began with RUAG Space where we performed the thesis. We have been given a lot of support, opportunities and more so was included as a part of RUAG Space since the beginning of our thesis. First and furthermost we would like to show our gratitude towards our supervisor Jacob Christenssen who has been a fantastic support providing us with encouraging words, invaluable discussions and guidance at every step on the way. Furthermore, Jacob allowed us to borrow the *lab* (horse trailer) we used at Grimeton Radio Station.

Next, our go-to guy and former class-mate Mikael Lager provided us with fruitful discussions and an immense support when we was designing hardware and looking for instruments to use at Grimeton. Mikael always took an extra step every time he helped us, getting us instruments and providing with a large variety of support. Continuing with the other great supporters from RUAG Space with Anders Carlström who was with us since the beginning giving feedback on our work with the physics of the system and provided us with guidance during our weekly meetings.

Next, Patrik Sandin who always had faith in our ideas and provided us with economical means to realize our experiment. Also, Hans Corin helped us by providing some confidence regarding the potential EMC issues at Grimeton by giving us some time to discuss with him. Also a large thanks to Dennis Kleen for saving us troubles by reviewing our hardware design and provided us with some discussions. Our gratitude to Jan Broman for discussions regarding a sampling source which led to using an Oscilloscope. Before we had decided on a plan Heinz Fragner from RUAG Space GmbH helped us guide the thesis into something that was of interest to both RUAG Space and us, pointing us into a much more interesting area than the initial.

After spending a total of five years at Chalmers University of Technology the place has become a second home. First out our gratitude goes to our examiner Rüdiger Haas who we felt was more like a supervisor as he was a constant support during our whole thesis.

Besides Rüdiger we also had meetings and discussions with Albert Monteith and Lars Ulander regarding experiment setups, hardware, geometeris and connecting this to passive radar setups. Finally, a thanks to Thomas Eriksson for the fruitful discussion on the requirements regarding phase-synchronization in our experiment system.

There were some sponsors who played a vital role in making the experiment a possibility instead of just a dream. Starting with the World Heritage Grimeton Radio Station, the historical radio station where we performed our experiment. If they did not allow us to place our hardware in their antenna we would not have the results we did. Besides that they where optimistic and supportive the whole time and provided us with a large amount of hospitality during our stay there. A special thanks to Cornelia Magnusson (SA6AND) and Anders Larsson (SA6CYL) for being

an important part in our project.

When we designed the system we quickly came to the conclusion that some of the hardware required was not something bought of a shelf and thus we established contact with Swedish Microwave (SMW) and LEAX Arkivator. We wrote an email to Olle Carlsson about our little experiment in hope that he could provide us with sponsorship from SMW, we got so much more. SMW sponsored us with some vital hardware parts while Olle took it further by reviewing our hardware design and helped us avoid several issues.

Once the experiment was getting closer, we came to the bitter conclusion that we had no antennas as the requirements on them was a bit too specific to make it simple. We contacted Tomas Östling at LEAX Akrivator who met us with interest and invited us to their office. After a brief discussion LEAX Arkivator provided us with the last piece of the puzzle required to perform our experiment and even took it a step further with providing us with some wave guide components that was a large help during our system verification tests.

Once we had hardware we also required a way to install it and thus came into contact with Per Blomstrand at ProAccess who helped us by partially sponsoring a high-altitude certification on a short notice. Later due to some issues we ended up having to hire high-altitude workers anyway where ProAccess for a discounted prize provided us with Julian Håkansson and Oskar Sandberg, whom both proved to be great additions to the team.

The fraternity and ham-radio club ETA at Chalmers provided us with some instruments and hardware. Furthermore, the members Johan Karlsson (SA6JKK), Max Sikström (SA6BBC), David Johansson (SA6DGJ), Simon Björklund and Joel Bjurström (SA6MTU) provided helpful discussion regarding software designed radios, receivers, microwave hardware, high-altitude safety and antenna connections.

Lastly, our love and gratitude goes to the coffee machines at RUAG Space, for giving us energy every morning.

Patrik Bennet & Frans-Erik Isaksson, Gothenburg, September 2020

Contents

List of Figures

List of Tables

List of Acronyms

ADC analogue to digital converter
AWGN additive white Gaussian noise

B-PSK binary phase shift keying
BB base-band

CCI co-channel interference
CDMA code division multiple access
CYGNSS cyclone GNSS

DDM delay-Doppler map

EM electromagnetic
EMC electromagnetic compatibility
EMI electromagnetic interference
ESA European Space Agency

FDMA frequency division multiple access
FPGA field programmable gate array

GEO geo-stationary Earth orbit
GLONASS globalnaja navigatsionnaja sputnikovaja sistema
GNSS global navigation satellite system
GNSS-R GNSS-reflectometry
GPS global positioning system
GRAS GNSS receiver for atmospheric sounding

HPF high-pass filter

ICI inter-carrier interference
iGNSS-R interforometric GNSS-R
IPT interference pattern techniques
ISI inter-symbol interference
ITU International Telecommunication Union

LEO low Earth orbit
LHCP left hand circular polarized
LNA low-noise amplifier
LNB low-noise block down converter
LO local oscillator

LOS line of sight
LPF low-pass filter

MEO medium Earth orbit

NASA National Aeronautics and Space Administration
NRCS normalised radar cross section

OFDM orthogonal frequency division multiplexing

P-RAS passive reflectometry and scatterometry
PARIS passive reflectometry and interferometric system
PRETTY passive reflectometry and dosimetry
PRN pseudo-random noise

Radar radio detection and ranging
RAS reflectometry and scatterometry
RB radar brightness
RCS radar cross section
RHCP right hand circular polarized
RO radio occultation
RS remote sensing
RTS real time system

SAR synthetic aperture radar
SDMA space division multiple access
SDR software defined radio
SMW Swedish Microwave AB
SNR signal to noise ratio
SOOP signals of opportunity

TDMA time division multiple access
TEC total electron content
TLE two line element

VLEO very low Earth orbit

WAF Woodward ambiguity Function
WGS84 world geodetic system 84

1
Introduction

Remote sensing is a term that was introduced in the 1960s by Evelyn Pruitt and refers to a measurement from a distance in contrast to a contact sensor. A common photograph is an example of a remote sensing measurement of different wavelengths of visible electromagnetic radiation (light). Today there are a large variety of remote sensing applications and some of those are used for Earth observations, where measurements of our little blue planet are made for various purposes. [2]

Earth observation has made a large impact on different areas of our society such as satellite positioning, weather forecasts and a general increase in knowledge regarding our planet. Today these systems produce a huge variety of data for various purposes. But most of these systems are active systems that were designed for Earth observations whereas this thesis will consider exploiting systems not made for it. The single prominent such passive reflectometry system is the cyclone GNSS (CYGNSS) constellation which exploits global navigation satellite system (GNSS) signals to extract information about oceanic wind speed [3].

Current active systems, including CYGNSS, use approaches that require knowledge about the signal which limits the possible signals of opportunity (SOOP) but in 1993 Manuel Martín-Neira proposed a different approach. In his paper he suggested the passive reflectometry and interferometric system (PARIS) concept using GNSS signals for ocean altimetry. He later confirmed his idea in an experiment published in his paper 2001 [4]. Since this approach uses a direct signal in additional to the reflected it opens up a large variety of possible signal candidates.

Today, there are no (known to us) active spaceborne PARIS systems even if there are demonstrations that proved the technology [5]. But in the upcoming year a proof-of-concept satellite developed by RUAG Space GmbH, TU Graz and Seibersdorf Laboratories called passive reflectometry and dosimetry (PRETTY) will be launched which will provide an active system where a lot of details regarding this types of systems can be proven [6]. It could provide the next step of development for remote sensing and Earth observations, where different fields could possibly develop from this type of technique.

1.1 The Reflectometry and Scatterometry Science and Technology – Old and New

Reflectometry and scatterometry are techniques that are important in Earth observations to make various measurements and the possibility to perform observations with passive measurements based on signals of opportunity can make it possible to

make use of small, compact receivers that have a low power requirement. As a reflectometry system uses reflected electromagnetic waves to indicate physical properties where for a passive reflectometry instrument the source of that wave is a signal of opportunity. Today there are a lot of signals transmitted from satellites in different orbits.

The opportunity signals transmitted by satellites are not meant for Earth observations but could in theory be used for it, albeit they might not be optimally designed for it as they differ in characteristics (e.g. carrier frequency, bandwidth and shape) and whether or not they are well known. Thus, comparing an active and a passive reflectometry system there are benefits and technical challenges to both types of systems.

Passive systems have some major benefits besides requiring specific geometries and a opportunity signal source. Firstly, the frequency spectrum is a limited and it is an expensive resource. Hence, recycling frequency bands and reusing the frequencies for Earth observations is an economical approach. Next, in spaceborne applications the cost of launching any payload into space is high and as a result the weight is of concern when designing an instrument and a passive instrument uses similar hardware as an active one but without the transmitter part, thus making it possible to make it both smaller and more light. Also, active instruments use more power due to the transmission requiring power which in power-limited situations can be a major issue. In spaceborne applications, power usage can cause an increase in the energy-storage required and thus further increase the weight for an active instrument. Lastly, an active system is focused around one specular reflection point while a passive system can have multiple as is the case for GNSS-reflectometry (GNSS-R).

Some challenges concerning the use of passive reflectometry instruments revolve around the SOOP, firstly the signal might not be known or have some features that require estimations which can be problematic since the signal to noise ratio (SNR) might be low. Furthermore, the signal power is not designed to be reflected back into space and can therefore be far below the thermal radiation radiated from the surrounding area. This can severely limit the system, as sufficient SNR is required both for detecting the signal and for resolving parameters used to derive some characteristic of interest. Also, as the SOOP sources are not variable there are geometric requirements that depend on the system. Lastly, the field of passive reflectometry and scatterometry is relatively new and has yet to be explored to a high degree.

1.2 Social, Ethical and Ecological aspects

As an engineer or scientist it is very important to consider the implications ones work can have on the world. Considering social, ethical and ecological aspects are important since there might be unintended negative repercussion that could have been avoided.

There is a seen possibility to improve future Earth observations with passive systems in terms of resolution, revisit time and coverage. This could notably improve some aspects of our daily life with information regarding soil-moisture, droughts, floods or data that could improve weather forecasts. Furthermore, this thesis is

focused on a relatively new branch of science which can have a large potential for improvement.

Today, the use of reflectometry and scatterometry techniques plays an important role in agriculture, weather forecasting, climate research and many other fields. Improving this technology could provide many benefits and might be an important step to further improve our society. It could also prove to be beneficial in fields not yet realised as the technology becomes more available.

Looking towards the use of passive instruments, the development of technologies that does not require to occupy their own frequency band is important as the amount of bandwidth is limited and becoming more and more scarce. But the passive measurements involve recording, analysing and knowing much about the transmitted signals of opportunity. This signal could be a communication message containing sensitive information. Thus handling this data could become important since the signals contain information transmitted from somewhere, albeit it would probably be encrypted.

Lastly, there are strong connections between a passive reflectometry and scatterometry (P-RAS) system for Earth observations and a passive radar system since they are in many ways the same type of system. A passive multi-static radar could be used for Earth observations, the major difference is the objects of interest. An Earth observation system used to measure soil-moisture would be interested in the clutter that a radar deems a disturbance and source of error.

To conclude, there are many possible benefits from improving the field of P-RAS while there are also some potential negatives. Regarding the data, the systems generally are designed such that the information transmitted is not saved since it does not contain anything of interest for an Earth observation system. Regarding military applications, this could be used for good as there are many resources focusing on military radar and they have to deal with the clutter which is of interest to many Earth observation applications.

1.3 Aim

This thesis aims at to investigate prospects of passive reflectometry and scatterometry using general spaceborne opportunity signals, with emphasis on identifying other promising signal sources in addition to the extensively researched GNSS systems. Furthermore, there is a wish to briefly summarize the possible techniques and consider if the requirements on these techniques limit their uses for opportunity signals. Lastly, to support the conclusions drawn and to possibly further explore the subject, it is intended to define and perform an experiment using a passive reflectometry and/or scatterometry technique aimed to investigate an application of interest.

1.4 Problem Description and Objectives

The aim described in the previous section will be achieved by completing the following objectives.

- Describe the principles of scatterometry and reflectometry measurements including general techniques.
- Describe passive reflectometry and scatterometry techniques.
  - Analyse and find key characteristics of signals for passive reflectometry and scatterometry.
  - Consider possible signals of opportunity sources for passive reflectometry and scatterometry.
- Describe the capabilities of passive reflectometry and scatterometry (i.e. to observe physical properties from measurements).
- Consider operational, scientific and humanitarian demands, wants and needs where passive reflectometry and scatterometry capabilities have and could prove beneficial.
- Evaluate in practice, by defining and implementing (an) experiment(s), the prospects of some spaceborne signal of opportunity candidate(s) and/or signal traits for passive reflectometry and scatterometry applications.

1.5 Limitations

As in every project the scope requires limitations due to constraints such as time and money. In this section some limitations are stated that was relevant to make the scope of the project more managable.

The constraints on the practical experiment was mainly in time, economy and knowledge. Firstly, an optimal platform would have been spaceborne and moving (i.e. a satellite) but due to time and economical constraints this was not plausible. The second best platform would have been an airborne platform which also was not plausible for the same reasons. Instead the focus was on a stationary platform at high altitude (an antenna tower at Grimeton radio station).

1.6 Method – Study, Explore and Conclude

The method is aimed to derive a clear structure to achieve the aim of the thesis. For simplicity, the thesis was divided into three main phases as is described in the following subsections.

1.6.1 Study the principal overview of passive reflectometry and scatterometry

The first four of the five previously described objectives are achieved through performing a literature study. This is thereby covering the four main areas: principles, techniques, applications and needs of passive reflectometry and scatterometry. Each of those areas do in turn consist of a number of essential subjects, which are thereby seen relevant to cover.

The P-RAS principles study is to cover the following four main subjects:

- Evaluate signal sources and properties to analyse SOOP characteristics as well as identifying related factors/effects potentially limiting the system.

- Consider the effects of electromagnetic wave propagation in the atmosphere and surface scattering effects on a candidate signal and its meaning for the system performance.
- Summarise the basics of a bi- and multi-static radar system, since that is the type of measurement system used for P-RAS.
- A brief summary of potential noise and interference issues, together with possible ways to suppress the effect of those on the system performance.

Furthermore, the P-RAS techniques and applications areas of study is seen to be strongly interconnected and consist of the three subjects:

- Describe different P-RAS technique approaches.
- Cover the associated resulting observables in general terms and, if possible, their quality measures.
- Summarise possible P-RAS applications, such as soil moisture or cryosphere measurements, for the identified techniques.

Lastly, the applications can be connected to the capabilities of the system and the seen demands and needs for those.

1.6.2 Explore passive reflectometry and scatterometry through an experiment

A P-RAS experiment is sought to be performed to further the understanding of the science and technology and to explore its possibilities. This is accomplished in seven main steps, accordingly:

- Identify and motivate a meaningful aim, purpose and scope of an experiment, including e.g. the choice of technique to explore, SOOP to use and application to investigate.
- Design an experiment setup, including rough outlines of the geometry, hardware and software requirements and physics.
- Perform a detailed pilot study of the experiment expected results, to indicate its plausibility.
- Design and implement a P-RAS software processing solution.
- Design and implement a P-RAS RF-frontend hardware solution.
- Verify the system function through tests and simulations.
- Perform the experiment and discuss the implications of the acquired results.

1.6.3 Conclude experiment, applications and capabilities

Finally, the knowledge and experience gathered throughout the previous literature study and experiment activities would be connected and concluded as to:

- Evaluate the experiment results in connection with the expected theoretical performance.
- Connect the study and experiment results to the thesis aim and objectives.
- Discuss the possible conclusions that can be drawn from interpreting the results, connecting those to a thought spaceborne system.
- Perform a discussion to provide basis for possible future studies that could further the field of P-RAS.

2

A Study of Passive Reflectometry and Scatterometry Principles

Since the use of GNSS-R in remote sensing (RS) applications was first envisioned around 1990 and Martin-Neíra introduced the PARIS concept there has been a lot of progress in the field. Today there are working satellite constellations in orbit [3] and more that have their launch planned [6] that uses GNSS-R techniques that implement and expanded on those envisioned by Martin-Neíra in 1993 [7].

To review the possibilities of P-RAS, other SOOP than those the GNSS constellations will be reviewed from the limiting factors of different reflectometry and scatterometry (RAS) techniques. This will be approached by first describing the basics of reflectometry, bistatic radar, satellite geometry, delay-Doppler map (DDM) followed by different relevant reflectometry techniques.

2.1 Signal of Opportunity Sources

This section will describe different sources for SOOP, i.e. signals are not designed for reflectometry but can be used for it using some techniques. In this thesis-work satellite providing SOOP are mainly considered from the categories; geo-stationary Earth orbit (GEO) broadcasting satellites and low Earth orbit (LEO) telecommunication satellites. There are additional categories that might be worth noting, but they will at most be mentioned as the scope of the thesis is limited..

2.1.1 GNSS signals

The demand for precise and reliable global navigation services is increasing and spaceborne such systems have proven to be excellent for those purposes. For a long time American Global positioning system (GPS) and Russian globalnaja navigatsionnaja sputnikovaja sistema (GLONASS) systems has been dominating the GNSS services, but due to increased demand from advances in technology and national integrity many other systems are soon to be operational. The current major GNSS systems in orbit are GPS, GLONASS, the European Galileo and the Chinese BeiDou, with a planned total of about 120 satellites in medium Earth orbit (MEO). There are also regional systems like the Indian NAVIC and Japanease QZSS and probably more to come [2].

The GNSS signal properties are constructed to be similar for all such systems, since it is favourable for a single receiver to be able to track as many satellites as

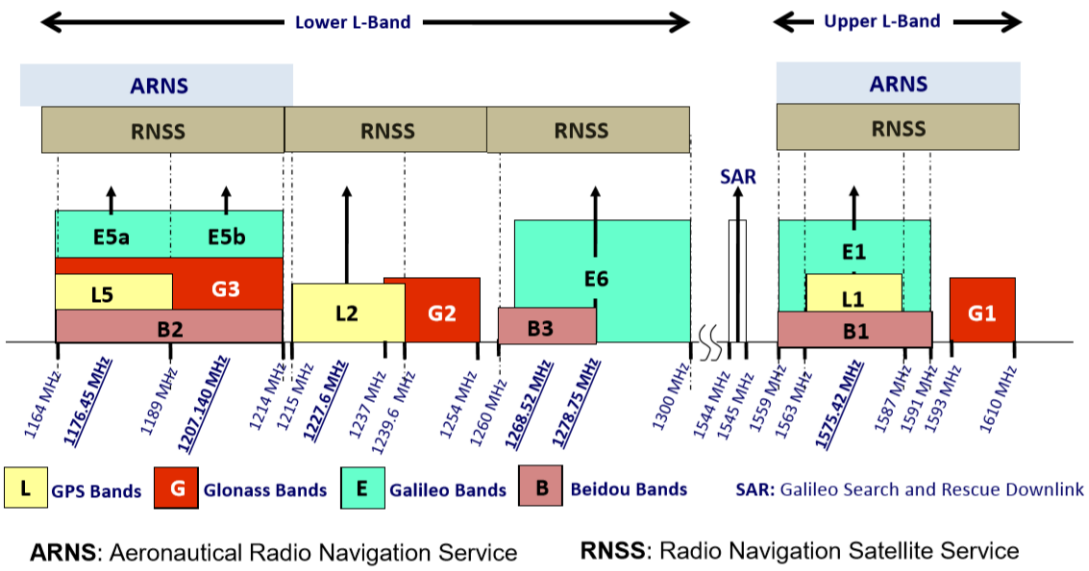

Figure 2.1: Block diagram over Galileo, GPS, GLONASS and BeiDou navigational frequency bands. Taken from *GNSS Data Processing Volume I: Fundamentals and Algorithms* by Subirana, Zornoza, and Hernández-Pajares with permission from the Author J. Sanz [8].

possible independent of which system they belong to. The signal carriers are all located at L-band and most of the systems use CDMA (spread spectrum) to share the same bandwidth resources. This is part of the reason why the GNSS signals are useful as opportunity sources for reflectometry applications, as they are today used for radio occultation (RO) and GNSS-R [2].

In general, a GNSS signal frame is structured in the following way. At the most underlying layer, a sequence of binary phase shift keying (B-PSK) modulated chips constructs a repeating pseudo-random noise (PRN) code. A sequence of codes is in turn used to carry a navigation information message at a relatively low bit rate, again using B-PSK modulation. One GNSS satellite often transmits several codes at different rates or orthogonal in phase in parallel for a given carrier as well as on several carriers, as indicated Figure 2.1. A more thorough description of the GPS, GLONASS, Galileo and BeiDou signals and systems is described in [8].

Only considering the GPS as the others are similarly designed after it, the L1, L2 and L5 signals all contain a 1023 sequence length PRN C/A-code based on a 1 MHz chip rate using 2 MHz bandwidth [8]. There is also an encrypted Y-code (P-code times W-code) at 10 MHz chip rate using a 2 MHz bandwidth [8]. The GPS signal is transmitted continuously at a power specified as at a minimum of -15.7 dBm [2]. In practise, the actual transmit power can be up to about 3 dB higher.

In short, it can be concluded that the GPS, Galileo, GLONASS and BeiDou systems signals have properties which makes them useful for reflectometry purposes. This was expected as GNSS signals are already used in the CYGNSS constellation and will be used in more planned future systems, besides they are also used for RO by

for example the GNSS receiver for atmospheric sounding (GRAS) instrument. The GNSS systems are appropriate for reflectometry because they are well documented, the satellite position, system and signal structure are known. Finally, the geometry is favourable for some types of reflectometry techniques with a MEO orbit, constant global coverage and a large number of satellites [2].

2.1.2 Geostationary broadcasting satellite signals

There are many satellites in geostationary orbit (GEO) that continuously transmit signals for TV and Radio applications etc. These signals are well known and designed to be easy to locate with a stationary receiver on the Earth surface (high SNR), which is a favourable characteristic [9]. Besides that there is a almost global coverage with continuous broadcasting towards all populated continents, there are a large set of possible customers without the need to construct and maintain much infrastructure.

Most GEO broadcasting satellites considered transmit on the Ku- and C- band, this is regulated by the International Telecommunication Union (ITU). These satellites transmit with large bandwidths, 40 MHz bandwidth [10] windows including the guard-bands. But as there are many parallel channels they can be used together to get multiple such bandwidths getting very wide band signals, assuming that the same satellite transmits in adjacent bands.

These satellites are in a stationary orbit around Earth and could be described as hovering above a spot at the equator. This makes it relatively simple to derive the position of the satellite to calculate signal paths for finding a specular point, more on this in Section 2.3.2. In general, as they are in such a distant orbit it is a beneficial geometry with the limitation that they do not illuminate the polar areas of the Earth.

To summarize, geostationary satellite signals are interesting to P-RAS since they are well documented and have a favourable geometry for certain applications. The constantly transmissions with high power, bandwidth and coverage also provide it with possible uses. The carrier frequencies might cause issues due to free space loss while it also provides a beneficial type of scattering. More on scattering in Section 2.3.

2.1.3 Low Earth orbit telecommunication satellite signals

The first successful launch of a satellite into a LEO orbit was Sputnik 1 by Russia and today those orbits are used for large variety of applications [2]. A common type of transmission from LEO orbit is burst-transmissions for telecommunication where there is a specific user somewhere on Earth [2]. The type of constellations that are mainly considered in this report are so called mega constellations (planned and in orbit) such as Starlink, Project Kuiper, and OneWeb. The LEO orbit allow for short revisit times, global coverage and relatively low SNR.

The LEO telecommunication satellite are considered to transmit on different frequency bands assigned by the ITU, such as X-, Ku- and Ka-band, but there are also plans for other such frequency bands as the V- and E-band. These systems often use burst-transmissions together with directive antennas and high power to provide

a robust system with high throughput. Mind that there are many such systems and more are coming, just the Kuiper system is planning over 3000 satellites [11] and Starlink is planning about 12 000 satellites [12]. With so many satellites and systems there are also bound to be variations in how these systems are designed, which needs to be taken into account when designing a reflectometry system.

The is a large variety of LEO satellites, but a number of them could possibly be used for P-RAS. The amount of present and future satellite systems could be a major benefit providing multiple sources while the variations between them could cause issues with differences or similarities (interference). Also, the geometry could cause issues for certain types of techniques, more on this in Section 3.1.

2.2 Signal Properties

The general structure of satellite signals can be said to have much in common, such as polarization and often consisting of amplitude- or phase-modulated root-raised cosine pulse sequences. There are also some significant differences, e.g. carrier, bandwidth, coding, mode and content of transmission, which are further described in this section.

2.2.1 Polarization

First, all propagating signals have a polarization, which can be altered through interactions with different media. It is initially determined by the source of transmission, where the antenna is usually designed to yield a certain polarization. As a property of the signal, it is often described using the Stokes vector described as

$$\vec{S} = \begin{pmatrix} S_0 \\ S_1 \\ S_2 \\ S_3 \end{pmatrix} = \begin{pmatrix} \langle E_{0x}^2 \rangle + \langle E_{0y}^2 \rangle \\ \langle E_{0x}^2 \rangle - \langle E_{0y}^2 \rangle \\ \langle 2E_{0x}E_{0y}cos(\phi_y - \phi_x) \rangle \\ \langle 2E_{0x}E_{0y}sin(\phi_y - \phi_x) \rangle \end{pmatrix}, \tag{2.1}$$

where S_0, S_1, S_2 and S_3 are the total signal energy as well as $\hat{x}$ or $\hat{y}$ linear, $\pm 45°$ linear and right-hand circular degrees of polarization respectively. E_{0x} and E_{0y} are the Cartesian electric field amplitude components orthogonal to the plane wave propagation direction and ϕ_x and ϕ_y are the phases of those components. The Stokes vector is often normalized by the signal energy such that S_0 always is one, for polarization interpretation purposes (e.g. $S_3 = -1$ then implies a pure left-hand circular polarization) [13].

2.2.2 Signal modulation

For a given polarization, each signal is modulated in amplitude and phase (in-phase cosine and quadrature sine components added in the signal since those pulse shapes are orthogonal) to either provide detection capabilities or to convey information within a certain bandwidth around a certain carrier frequency. For telecommunication purposes a root-raised cosine (RRC) pulse shape is used to modulate the

signal since it allows for T_s orthogonal symbol rates for a given bandwidth and limited pulse duration. This pulse shape is ISI-free (inter-symbol interference) after matched filtering where it becomes a raised cosine [14], [15]. Do mind that active microwave remote sensing systems often use a chirp pulse shape, i.e. linear frequency modulation (LFM), due to its excellent pulse compression capabilities [13]. A modulated signal can in general be expressed as

$$s(t) = \Re\{u(t)e^{j2\pi f_c t}\}, \tag{2.2}$$

where f_c is the carrier frequency and $u(t)$ the baseband signal. This can in turn be further described by

$$u(t) = \left(\sum_{n=1}^{N} a_n e^{j\phi_n}\delta(t - nT_s)\right) * g(t), \tag{2.3}$$

using a pulse shaping filter $g(t)$ and a complex symbol train with amplitude a_n and phase ϕ_n of N symbols with time intervals T_s.

For the RRC pulse shaping case, the symbol timing interval T_s is given by the inverse double-sided bandwidth B and the system-specific roll-off factor α as [15]

$$T_s = \frac{(1+\alpha)}{B}. \tag{2.4}$$

In these systems a known sequence of symbols, e.g. a preamble or code, is used to provide detection capabilities of the signal. The code can in turn also be used to carry information symbols orthogonal to the specific other code sequences, hence allowing code-division multiple access (CDMA) schemes to be used for system time and bandwidth resource-sharing purposes. In this case the underlying symbols of the sequence are commonly referred to as chips to avoid confusion. Although, since some CDMA schemes are not always perfectly orthogonal, but only almost so, they give rise to an interference noise floor limitation. This is prominent for e.g. pseudo-random noise (PRN) codes used in GNSS where about 0.1 % to 6.2 % of a signals power interfere between codes [2]. The code time interval is then given as the code length times the chip time interval.

When the purpose is rather to detect the pulse arrival time than to convey information at high rates efficiently, which generally is the case for e.g. radar systems, a chirp pulse shape is often used. This pulse shaping filter can be expressed as

$$g_{chirp}(t) = \frac{1}{\sqrt{T_p}} I(0 < t < T_p) e^{j\pi\gamma t^2}, \tag{2.5}$$

in terms of the pulse duration T_p, the rectangular function I and the chirp rate γ.

An important property (or rather quality measure) of signals for detection and ranging applications is the pulse compression capability. This is often expressed as described by

$$\frac{T_p}{\delta t_{3dB}} = BT_p, \tag{2.6}$$

where the result is the ratio of the signal pulse width T_p and correlation peak 3-dB width in time δt_{3dB}. The result is as seen a multiplication of the bandwidth and pulse time duration and the measure is hence called the time-bandwidth product. A high value is desirable due to the fact that the energy of the pulse can be spread in time and hence ease on transmission power demands for a certain resolution and required SNR. It turns out that pulse compression by the time-bandwidth product factor can in general be achieved for as good as any modulation format [16].

Signal detection is generally performed using a filter matched to the signal pulse shape as well as by correlating the result with the signals known certain pilot or code sequence, if such are used. The process can be described by the convolution

$$s_{detect}(t) = s(t) * s^{C}_{known}(-t), \tag{2.7}$$

for an analysed signal $s(t)$ where a signal structure $s_{known}(t)$ is searched for. The detection threshold of the energy observed in $s(t)$ should be set such that to optimize a sought false detection versus missed detection probability ratio. Frequency and timing offsets and distortions give rise to mismatch in the correlation, which can (if expected) be accounted for by using parallel filtering streams separated in the parameter space by the 3-dB width of the optimal correlation peak for respective parameter.

2.2.3 Channel fading effects

Some important main distortion effects can be said to affect the signal, to different extent depending on the system and propagation environment, before it reaches the system receiver. Carrier frequency offsets may occur due to Doppler shifts and clock errors, symbol timing offsets due to analogue to digital converter (ADC) clock errors, and phase offsets due to system delay, signal path distance and the channel impulse response. The impulse response may also not be flat in frequency within the signal bandwidth, which might be crucial for large bandwidth (wideband) signals. For narrow bandwidth (narrowband) signals the frequency response can be assumed to be flat. The channel frequency response coherence bandwidth B_c can be approximated as the inverse of the root-mean square (RMS) channel scatterer timing difference τ_{rms} according to [14]

$$B_c \approx \frac{1}{\tau_{rms}}. \tag{2.8}$$

Wide- or narrowband signal cases are determined by whether the bandwidth is much larger or smaller than this coherence bandwidth [14].

Especially important for a moving non-line of sight (NLOS) system (as in the spaceborne reflectometry case) is that the signal is prone to experience fading effects, causing the channel to completely decorrelate at worst at the order of a wavelength movement in position [14]. A rough approximation of this signal channel coherence time, T_c, can be given as

$$T_c \approx \frac{\lambda}{2|v_{specular}|}, \tag{2.9}$$

where λ is the signal carrier wavelength and $v_{specular}$ the velocity of the specular point projected on the ground surface between the transmitter and receiver systems, which is hence dependent on both their respective velocities and the geometry of the environment, assuming a stationary multipath environment.

This also has the implication that the statistical properties of the channel causes the received signal power to vary according to an exponential distribution random process with its mean at the expected signal power [14]. Coherent signal acquisition and integration is hence only possible within a coherence time. As seen in Equation 2.9, it can be noted that high carrier frequencies in combination with large transmitter and receiver velocities implies a short coherence time.

2.3 EM Wave Propagation and Scattering Effects

For any signal, the reason it can used in the field of RAS is because of the effect the environment has on it. As a signal travels, absorption, reflection and scattering affect the signal properties and these changes can be tied to properties of the media or reflecting and scattering surfaces. This section will aim to describe the basics of absorption, reflection and scattering and where they appear.

2.3.1 Atmospheric scattering and absorption

Opacity is a ratio of how much of the incoming energy that does not pass through the medium and it is affected by processes such as scattering, absorption and reflection. Measuring the opacity can be useful to calculate how much of the incoming radiation is expected to pass through a medium, or if the medium is well known to calculate the amount of incoming radiation. This can be used for various things such as identifying what type of particles are present in the medium [13].

When considering (atmospheric) scattering it is common to talk about three types of scattering. Firstly, Rayleigh scattering when the wavelength is much smaller than the particle size. Secondly, Mie scattering when the wavelength is similar to the particle size. Lastly, Non-selective scattering when the wavelength is much larger than the particle size. In all cases, the type of scattering is an approximation used to model scattering and this process is complex [2], [13]. As George Box (University of Wisconsin-Madison) stated in 1976: all models are wrong, but some are useful [17].

Rayleigh scattering is an approximation that is valid for scattering against particles that are much smaller than the wavelength, such as molecules in the case of microwaves. The scattering is approximately isotropic and thus has no directivity. An example of this scattering is the blue colour of the sky. Since Rayleigh scattering affects shorter wavelengths more, blue light is scattered more than the longer wavelengths like red or yellow causing more blue light to be scattered towards the Earth's surface. The proportionality of the Rayleigh scattering pattern can be described by

$$\beta_r(\theta, \lambda) \propto \frac{1}{\lambda^4}(1 + \cos^2\theta), \tag{2.10}$$

where λ is the wavelength of the electromagnetic (EM) and θ is the angle to the reference line due to the changing path in a non-static case [2], [13].

Mie scattering is caused by particles that have a size that is similar to the wavelength. This type of scattering is generally not isotropic and thus has a directivity. The scattering pattern varies as described by

$$\beta_r(\theta, \lambda) \propto \lambda^m f(\theta),\ m \in (-2, 0.6). \tag{2.11}$$

Generally Mie scattering occurs in the lower atmosphere where the presence of large particles such as dust, pollen and clouds are more common. An effect of Mie scattering is the colour of smoke and smog (air polution) [2].

The last type of atmospheric scattering is called non-selective scattering and is the result of scattering from particles or objects of much larger size than the wavelength. This type of scattering is generally isotropic and affects most wavelengths in a similar way. Once again looking at an everyday example, the clouds get their white colour from the non-selective scattering of visible light. Since it causes isotropic scattering to a similar degree to most frequencies non-selective scattering cause similar amounts of all wavelengths to be scattered which causes the white colour [2].

Atmospheric absorption is a process where energy from an incoming EM is absorbed by a media. According to the Beer-Lambert law the absorption is proportional to the length of the path through the medium for the EM and the concentration of the absorbing species in the medium. Similar to Rayleigh scattering, this effect is also inversely proportional to the wavelengths, hence a lower wavelength causes more energy to be absorbed. A notable effect from this is the red sky caused by the sun setting and rising can be explained by atmospheric absorption. This is since the setting sun has a longer path through the atmosphere and larger wavelengths such as red are less affected by absorption. Thus even though the blue is more scattered it is also more absorbed, thus causing the red colour of the setting and rising sun [2], [13].

Figure 2.2 shows the frequencies or wavelengths of the electromagnetic spectrum that pass through the atmosphere. This shows how the atmosphere protects living organisms from dangerous high-energy EM such as X-Rays and Gamma waves while allowing us to make use of the visible spectrum to see. Lastly, the radio window allows for communication through the atmosphere using radio waves and microwaves. The microwave frequency region is located at a transit from a transparent to an opaque atmosphere. The opaqueness frequency dependence can thus be used as a remote sensing tool, by through spectroscopy inferring the content of substances in the atmosphere.

2.3.1.1 Atmosperic layers

The atmosphere is divided into different layers with different characteristics. The layers from the ground and up are; troposphere, stratosphere, mesosphere and thermosphere. Between these layers there are transition layers, such as the tropopause between the troposphere and the stratosphere. Besides those layers, the ionosphere

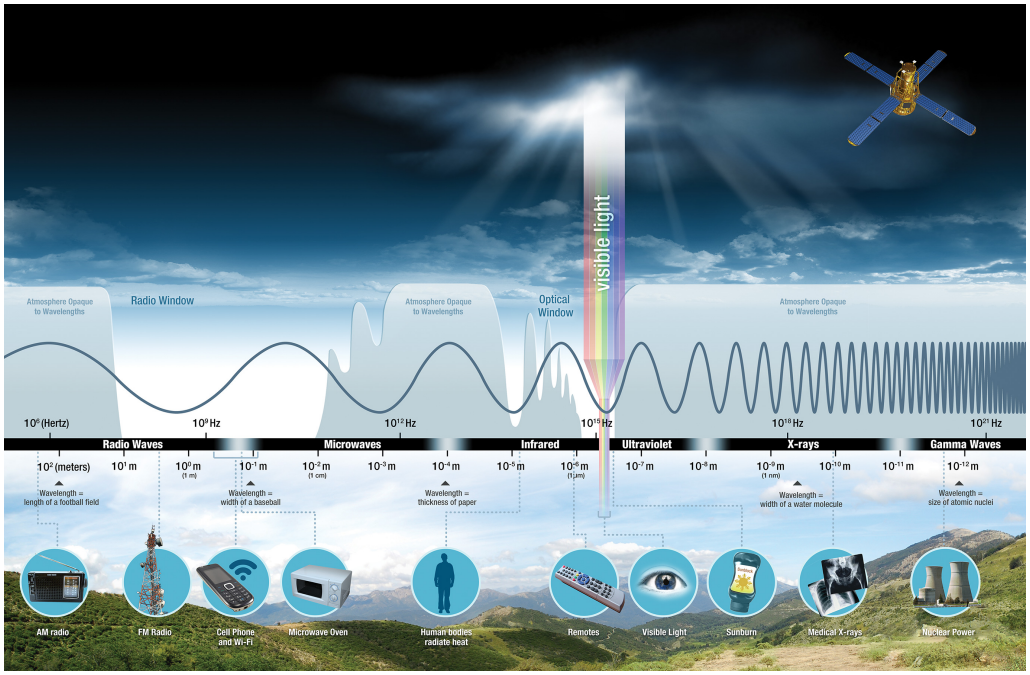

Figure 2.2: Illustration that shows how different wavelengths of the electromagnetic spectrum can pass through the atmosphere. As seen in the figure, most frequencies does not pass through the atmosphere, but two important *windows* are around the optical window and the radio window. Looking close the line with frequency and wavelengths are shown to illustrate how the wavelength is inversely proportional to the frequency. The figure also illustrates different sources of the different frequencies. Taken from [18].

spanning from the mesosphere to the thermosphere and the ozone layer in the stratosphere are two important parts of the atmosphere. [13]

When the the atmosphere is not the object of interest for a measurement it instead becomes a source of errors. To handle this there are different atmospheric models, one common approach is to only consider the troposphere and ionosphere. These two are are often referred to as the neutral atmosphere (troposphere) and the active atmosphere (ionosphere) where the neutral atmosphere consists of neutral gases while the active atmosphere consists of ionised plasma [13].

The neutral atmosphere mainly consists of carbon dioxide, nitrogen and water vapour. It is commonly further divided into the dry and the wet part part of the atmosphere. The dry part of the atmosphere is relatively homogeneous and unchanging besides changing as a function of the pressure. The wet part, so called since it is the affect of water vapour, varies a lot as the water in the troposphere varies, due to weather, seasons, etc. [13], [19].

The ionosphere is an ionised part of the atmosphere that varies in depth from 70 km to a few hundred kilometres that can have a large impact on the propagation of microwaves that passes through the atmosphere. One such effect that is important for applications such as navigation and altimeter is the delay caused by the ionosphere, with a 10 GHz signal a typical delay is about 0.1 m or 0.01 m for measurements made during the day respectively the night. This is due to the group delay difference caused by the radiation from the sun ionising the gas in the ionosphere resulting in an increased total electron content (TEC) [13] .

This delay is described by

$$t = \frac{z}{c} + \frac{e^2}{2\epsilon_0 m_e \omega^2 c} \int N dz, \tag{2.12}$$

where on the right-hand side $\frac{z}{c}$ is the travel time for light in vacuum, e is the electron charge, ϵ_0 is the electric permittivity of free space, m_e is the electron mass, ω is the angular frequency of the EM, c is the speed of light and $\int Ndz$ the integration of the electron density N [13].

There are four more general aspects of the ionosphere that could be important for different types of measurements, as they are the main effects on an EM passing through the atmosphere. Firstly, the ionosphere is dispersive since the refractive index is frequency dependant, thus it can be shown that the group velocity differs from the phase velocity. Secondly, it is also absorptive since the refraction index is a complex number where the imaginary part is called the extinction coefficient and describes how the medium absorb energy from the EM. Thirdly, it is also birefringent and thus has a refraction index with two distinct values which allows the possibility of two different ray paths where each different one would have a separate phase and group velocity, furthermore this also depends on the polarization. Lastly, it is anisotropic which means that the direction of measurement changes the result of the measurement [19].

Lastly an important note, the ionosphere places a lower limit on what frequencies can be transmitted through the atmosphere as it becomes increasingly opaque with frequencies below a threshold. This is due to dielectric constant of plasma and the resulting plasma frequency. To be prices, the ionosphere is opaque for frequencies

below the plasma frequency which depends on the TEC or more specifically the electron density of the plasma. According to [13] the maximum normal plasma frequency should be around 9 MHz and [20] notes a similar limit at 10 MHz. [20] also points out that the ionospheric influence on frequencies below 1 GHz can be significant [13], [20].

2.3.2 Surface scattering - reflection

As an EM reaches the boundary between two media, such as a ground or water surface, besides being scattered, absorbed and transmitted through the medium, some part of the EM can also be reflected. When a single beam is reflected off a *smooth* surface it is ideally called a specular reflection. A reflection point that is the closest reflected path between two points is called the specular reflection point. Depending on the surface roughness and inclination between incoming signal and reflecting surface there might be directional and diffuse scattering (generally both) [13].

The albedo (r) is related to the emissivity (ε) by the relation $r = 1 - \varepsilon$ where the emissivity describes how similar an object is to a perfect black body. The approximation that a surface is a perfect blackbody ($\varepsilon = 1 \longrightarrow r = 0$) would mean that no energy would be reflected from the surface. This does not hold true for common objects as most objects have an emissivity that is slightly less than 1. In the case where an EM is reflected off a surface, hemispherical albedo is defined as the average value of r over the hemisphere of possible incidence directions [13].

The albedo of a surface, be it directional or diffuse, is of great importance in the field of RS as is implied by the name; reflectometry. Albedo is also called reflectivity and it is the ratio of total and scattered power [13]. The scattering can be used to identify different characteristics of a surface. There are many scattering models and while it seems to be a simple concept it is a complex process that makes it complicated to design good models.

In the case of a surface that is very smooth in comparison to the wavelength it will act as a mirror and a specular reflection will occur causing the incoming EM rays to be reflected in a single direction. The surface smoothness can be described by the Rayleigh roughness criteria as

$$\Delta h < \frac{\lambda}{8 \cos \theta_0}, \tag{2.13}$$

where Δh is the root mean square deviation of the surface height, λ is the wavelength of the EM and θ_0 is the angle between zenith and the incoming ray (i.e. the incidence angle). Figure 2.3 illustrates the parameters of this criteria [13].

2.4 Bi- and Multi-Static Radar

The concept of RAS is closely related to how a radio detection and ranging (Radar) works, in the specific case of spaceborne passive reflectometry it is more specifically related to a bistatic radar. In some cases Multistatic radar might be more accurate

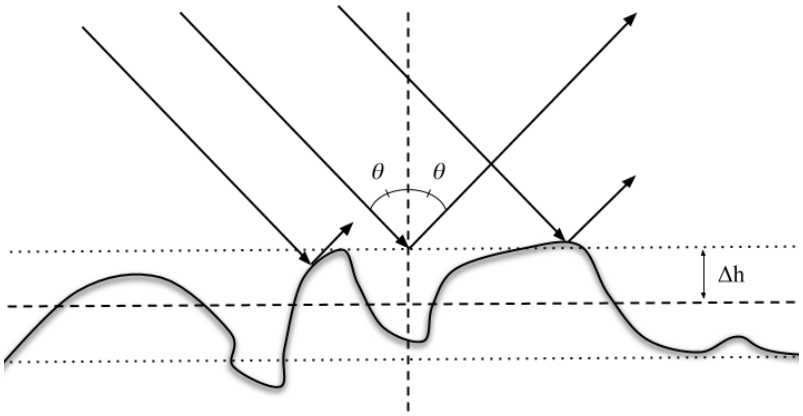

Figure 2.3: An illustration of surface roughness, where θ is the signal incidence angle and Δh is the standard deviation offset of the surface.

but the general concept is the same albiet simplified for bistatic radar. Thus describing a general spaceborne RAS system from the perspective of a bistatic radar is a natural approach. Details regarding the basics of a Radar can be found in any source describing Radar in basic terms.

A bistatic radar is similar to a monostatic radar but with some modifications. This can be seen in the bistatic radar equation, which can be expressed as

$$P_R = \underbrace{\underbrace{\frac{P_T \cdot G_T}{4\pi R_1^2}}_{|\vec{P}||_{target}} \cdot \sigma_b \frac{1}{4\pi R_2^2}}_{|\vec{P}||_{R_x}} \cdot \underbrace{\frac{G_R \cdot \lambda^2}{4\pi}}_{A_{eff,R_x}} \cdot L, \tag{2.14}$$

where P_R and P_T are received respectively transmitted power. G_R and G_T are the receiver respectively transmitter antenna gain. R_1 is the range from the transmitter and the reflection point while R_2 is the range between the receiver and the reflection point. λ is the wavelength of the carrier frequency and lastly σ_b is the bistatic radar cross section. Also, note that $|\vec{P}||_{target}$ and $|\vec{P}||_{R_x}$ are the pointing vector at the target respectively the receiver, while A_{eff,R_x} is the effective antenna area of receiving antenna [2].

Considering the bistatic radar geometry described by Figure 2.4, the transmitter transmits in the direction of the target where the EM is reflected towards the receiver, in the RAS case the reflection point on the ground. The amount of scattering from a target is based on the radar cross section (RCS) which is connected to the reflectivety and roughness of a surface or target. The RCS (σ_{RCS}) describes the ratio of incoming and outgoing power from isotropic scattering on a target and is defined as

$$\sigma_{RCS} = \lim_{r \to \infty} 4\pi r_0^2 \frac{P_{R_x}}{P_{T_x}}, \tag{2.15}$$

where the electromagnetic wave described is in the far-field regime as stated by the limit in the equation [2], [21].

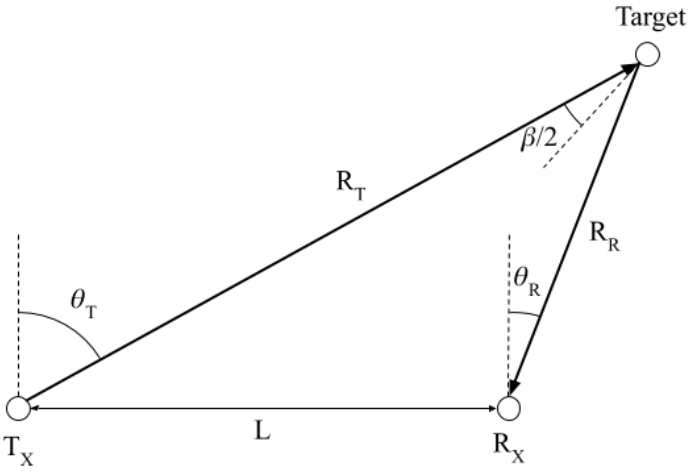

Figure 2.4: A bistatic Radar geometry, where the main positions are the transmitter, *Target* and the receiver. The distance R_T (distance between transmitter and *Target*), R_R (distance between *Target* and receiver) and L (distance between transmitter and receiver). Also, various angles and the speed of the transmitter and receiver is also marked.

Assuming isotropic scattering of a rough surface can be a poor assumption, since the scattering of a rough surface has multiple phase centres and thus might not be isotropic. To better describe the true RCS of a surface without clear boundaries, such as the ground or sea, the left side expression is introduced in

$$\sigma_0 = \frac{\langle \sigma_{RCS} \rangle_{cell}}{A_{cell}} \longrightarrow \beta_0 = \frac{\langle \sigma_{RCS} \rangle_{cell}}{A_{slant,cell}}, \tag{2.16}$$

which is describing the average RCS per unit resolution cell (σ_0). In the equation $\langle \sigma_{RCS} \rangle_{cell}$ describes the spatial averaging of the RCS over a number of observations in a resolution cell and lastly A_{cell} is the resolution cell area on the ground [2].

The RCS described by σ_0 is correct but has a topography-dependence and in the case where knowledge of the local topography is available another variable is suggested by the right side of Equation 2.16. β_0 is different from σ_0 in that it is scaled according to the unit area of the slant range resolution cell and is therefore avoiding the dependence of topography at the expense of requiring knowledge regarding the topography. The resulting variable β_0 is called radar brightness (RB) and is scaled according to the angle $\beta = \Theta_T - \Theta_R$ according to Figure 2.4 that describes the geometry from a 2D perspective. The connection between σ_0 and β_0 can be seen from two aspects by describing their relation as [2], [22]

$$\sigma_0 \approx \frac{\beta_0}{\sin(\Theta_i)} = \frac{\beta_0}{\sin(\Theta_{i,flat} - \alpha_{slope})} \longrightarrow \sin(\Theta_i) \approx \frac{A_{cell}}{A_{slant,cell}}. \tag{2.17}$$

Looking back to the bistatic radar Equation 2.14 and the difference regarding the bistatic RCS, the RCS has different approximations depending on the geometry. Three regions are described by [2]; the Pseudo-monostatic region, the bistatic RCS region and the forward-scattering region. Details regarding these regimes are not

described but in general the pseudo-monostatic regime is valid when $\beta < 5°$, the bistatic RCS region is valid when $5° < \beta < 175°$ and the forward-scattering region is valid when $175° > \beta > 180°$ [2].

2.5 Geometry and Delay-Doppler Maps

In the case of spaceborne P-RAS the geometry is mainly based around three points; the SOOP satellites transmitter, the specular reflection point or reflection point on the Earth and lastly the receiver satellite. In the specific case of PARIS a direct signal is used in addition to the reflected signal. Thus it requires the receiver to be inside the antenna beam of the transmitted signal hence limiting the interferometric approach to only work in certain geometries. A resulting geometrical limit is the transmitter satellite orbit, if the transmitter satellite has a lower orbit the direct signal will not reach the receiver as long as the beam does not reach above the horizon. In this case as there is no possibility for a direct signal there is no possibility of an interferometric approach.

Since reflectometry models reflections to identify characteristics regarding the surface, being able to resolve different cells on the ground is important. To resolve different points on the ground two different dimensions are considered; delay and Doppler. When a signal is reflected, the resulting forward scattering from different points are scattered in the direction of the receiver. These different points can be differentiated as they have a different path-length or delay depending on the radial distance from the specular reflection point as can be seen in Figure 2.5. Next, the signal-path changes as the satellites move with respect to each other causing a Doppler shift. This Doppler shift can be resolved providing iso-Doppler lines depending on the movement of the two satellites.

Together the iso-Delay circles and iso-Doppler lines can be used to construct a DDM which can be used find specific points on the ground. An important note regarding the DDM is that each iso-Doppler line crosses the iso-Delay contours twice, causing an ambiguity where these two points cannot be differentiated. [2] states that there is no way of solving this issue except for aiming the receiving antenna beam away from the specular point to attenuate the ambiguity.

The delay and the Doppler can be calculated using the expressions

$$\tau = \frac{R_T(t) + R_R(t)}{c} \tag{2.18}$$

and

$$R_R(t) = \frac{(R_T(t) + R_R(t))^2(t) - L^2}{2((R_T(t) + R_R(t)) + L \cdot \sin(\Theta_R))} \tag{2.19}$$

together with

$$f_D = -\frac{1}{\lambda}\frac{\partial}{\partial t}\left(R_T(t) + R_R(t)\right), \tag{2.20}$$

where τ is the delay, $R_T(t)$ is a distance between transmitter and the target, $R_R(t)$ is a distance between the target and receiver and lastly c is the speed of light.

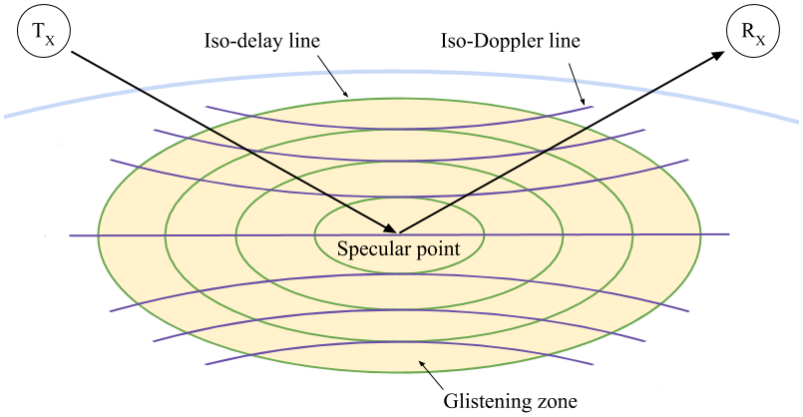

Figure 2.5: A DDM illustration around the specular point from the perspective of a bi-static geometry of two satellites. Around the specular point the iso-delay is shown by ovals and the iso-Doppler is shown by the bent lines in the along track. These ovals and lines can be separated as they are of different delay and Doppler-shift and by using these different reflection points on the ground can be resolved.

$R_R(t)$ is described by Equation 2.19 where L is the distance between the transmitter and the receiver and Θ_R is the look angle or angle of arrival of the receiver as seen in Figure 2.4. In Equation 2.20, the additional variable λ is the wavelength [2].

As the DDM provides iso-Delay contours and iso-Doppler lines, these can be fitted to a model of the Earth to provide accurate descriptions of the separate points according to the topography. An issue that arises is that the Earth is not a simple-static shape but rather a complex and slowly changing shape, depending on the application this might be more or less of an issue. A counter to these potential issues are models of the Earth's shape to describe the geometry around the specular reflection point that can be connected to the DDM to differentiate different areas. There are many models of the Earth ranging from flat Earth models to complex ones but a commonly used in GNSS applications is the world geodetic system 84 (WGS84) [2].

2.6 General Noise and Interference Issues

Measurements are prone to a variety of error-sources that cause errors, noise or interference. In the case of P-RAS there are error sources such as; model error, speckle noise, thermal noise, phase noise and interference. Other types of noise do exist and are sometimes of great importance but are not covered, in some cases these require coverage.

Every type of system has a temperature that creates a thermal noise floor, in some applications this floor is negligible but for reflectometry this noise can be a large noise term. Thermal noise comes from black-body radiation. This is radiated by the system, atmosphere, Earth surface, and everything in between. For the specific case of reflectometry, the antenna is most likely aimed at the ground which has a high temperature relative to the sky which cause the thermal noise floor to be

much higher than when the antenna is looking towards something cooler.

Thermal noise can be handled in different ways Some common ways of affecting it is system design, filtering and coherent integration. The antenna size affects mainly the signal power but not the noise power, thus relatively speaking the noise can be limited by increasing the antenna size and thus directivity. To avoid adding the system temperature to the noise it is important to optimize the the system, one such way is by using Friis formula to design it in a way that avoids adding additional notable thermal noise from the system.

Another important step of the design is before analogue to digital conversion, where any power at frequencies above the Nyquist frequency is aliased into the sampled bandwidth. This can be avoided by using filters before sampling thus limiting the aliased power to be negligible. Lastly, another way of countering additive white Gaussian noise (AWGN) from thermal sources or other sources is coherent integration.

Depending on the application, phase noise or frequency errors could cause major issues. Reflectometry most likely uses a cross-correlation to find power at different delays and Doppler frequencies. Phase noise and frequency errors cause the correlation to be decrease or disappear in severe cases. Depending on the technique there are different ways of countering these issues. When implementing an interferometric system the phase and frequency errors are only an issue if the error is different between the direct and reflected signal. Hence the interferometric case can handle drifting phase and frequency errors quite well by synchronizing the two signals.

Next we need to take care of the speckle noise. Sspeckle noise is the result of a signal taking multiple paths, thus at the receiver a super-position of multiple phases arrives causing constructive and destructive interference at the receiver. This results in a multiplicative noise called speckle. The power of this type of noise is based of the signal power [13], [16].

Handling the speckle noise is of great importance since it can potentially ruin valuable data. Thus when designing a system it needs to be taken into account. In radar imaging systems such as synthetic aperture radar (SAR) speckle noise is handled by creating multi-look images, where the coherent integration is followed by an incoherent integration. This use of the raw data causes some losses in spatial resolution but can remove the majority of the speckle noise [13], [16].

Lastly the topic of interference, it is not a noise source but instead an unwanted signal that looks like the signal in some way. There are different types of interference. Some types as described from the perspective of a communication system are; co-channel interference (CCI), inter-symbol interference (ISI) and inter-carrier interference (ICI) [14]. Depending on the SOOP sources used for spaceborne P-RAS the type of interference that causes the most issues could differ but a major limiting factor could be CCI. A case where this could be an issue is where the signal transmitted towards the Earth uses space division multiple access (SDMA) based of the surface. It might not be spatially orthogonal in space anymore. Handling this type of issue will differ between systems, in the case of GNSS the code division multiple access (CDMA) codes used are known and make them quasi-orthogonal at the cost of having a interference floor. Other systems might use SDMA, orthogonal frequency division multiplexing (OFDM) or time division multiple access (TDMA)

where each case have positive and negative effects.

3

A Study of Passive Reflectometry and Scatterometry Techniques, Applications and Needs

In the field of remote sensing there are a plethora of techniques for retrieving physical characteristics regarding various objects of interest. As this thesis focuses on signals from satellites it is bound to aim the focus towards the part of the spectra commonly used for satellite communications - microwaves. These techniques are based of the ones used in GNSS-R as that is the type of system we are intending, but with a different opportunity source.

3.1 Approaches to passive Reflectometry

Performing P-RAS can be done in a number of different ways and the most prominent discovered in the study will be summarized in this section. In general, all considered approaches differ in how they attain the reference signal s_X but are similar besides that point. The approaches are regenerative, reconstructive, interferometric and partially interferometric. Firstly, the regenerative approach generates s_X locally from knowing the signal well enough to reconstruct it. Secondly, the reconstructive approach generates part of s_X locally but also regenerates other parts of the signal based on coding. Thirdly, the interferometric approach records a direct signal as s_X instead of generating it which reduces the requirements on knowledge on the signal. Forth and lastly, the partial interferometric approach is the same as interferometric but knowledge of the signal structure is used to improve the SNR. An important note is that all these techniques are the basis for different GNSS-R techniques but are described in a more general manner. The specific GNSS-R techniques are described in [2].

A coherent correlation can be computed as

$$Y(t, \tau, f_D) = \int_{t}^{t+T_c} s_R(t') s_X^*(t' - \tau) e^{-j2\pi(f_c + f_D)t'} dt', \tag{3.1}$$

where the reflected signal (s_R) is correlated with the reference signal (s_X). In the equation t is the current time, τ is the delay, f_D is the Doppler shift, T_c is the coherent integration time and f_c is the carrier frequency. [2] describes three approaches for GNSS-R that are considered for the use with a general SOOP, assuming the

approaches requirements are fulfilled [2].

Speckle noise is another issue that can be handled by an non-coherent integration. This integration is described by

$$\mathbb{E}\{|Y(\tau, f_D)|^2\} \approx \frac{1}{N} \sum_{n=1}^{N} |Y(t_n, \tau, f_D)|^2 , \tag{3.2}$$

where the coherent integration is averaged over a number of views. Due to the multiplicative nature of speckle noise the averaging can remove the noise as the signal should converge towards the mean [2].

3.1.1 The regenerative approach

The regenerative approach generates a local copy of the reflected signal based on being able to predict it. Since this approach depends on predicting the signal there is a large requirement revolving around a priori knowledge which causes the approach to be limited to signals that are almost completely known, thus ruling out most types of signals. If sufficient information to predict the signal is achieved the remaining complexity is relatively low when comparing with other techniques.

As the regenerative approach is not dependant on a direct signal, it is much less geometry dependant since the receiver (satellite) does not need to be inside the direct antenna beam of the transmitter. Considering that one of the major limiting factors for using SOOP can be the geometry of the satellites or the antenna beams this could theoretically allow additional SOOP candidates. Another important limitation is the SNR of the signal s_X, in other approaches with a recorded signal this is limited while for the regenerative approach the SNR could be described as infinite [2].

In the specific case of GNSS-R the known public codes makes this approach suitable but it is also limited to only using those codes, thus limiting the bandwidth available comparing to the maximum available when using the complete GNSS signal. Another notable advantage worth mentioning when constructing a local copy of the reflected signal is that the SNR can become ideal and tend towards infinity. Lastly, a downside caused by using a lower bandwidth is that the delay and Doppler dynamics are increased [2].

Today this type of systems has been tested and implemented multiple times, albeit the spaceborne systems are fairly new it is a growing niche when considering spaceborne RS. One such system is the satellite constellation CYGNSS which consists of 8 satellites that aim to study hurricanes and wind speed by measuring GNSS signals scattered from the ocean surface [3]. This system uses the regenerative approach to perform GNSS-R (only GPS).

3.1.2 The reconstructive approach

The reconstructed approach as described for GNSS-R is similar to the regenerative approach but it also uses semi-codeless techniques to reconstruct the P-code [2]. Since the approach allows the use of the P-code it can make use of more bandwidth and thus providing the possibility to improve the resolution for certain techniques when comparing to just using the C/A-code. A disadvantage is that the system is

more complex and the processing causes loss in SNR, this loss is described differently in [2] and [23] but could be an issue.

In a more general case, this could be interpreted as using a part of the signal to track the signal while decoding the full signal to create a fresh copy to correlate with. In theory this could allow previously not usable SOOP with semi-predictable or high-SNR to become viable candidates for the approach. Such an implementation could be based on how a repeater works or a curve fitting based on the waveform and modulation type.

This approach places additional requirements to allow the reconstruction of the signal P(Y) and have also been implemented in the instrument PYCARO carried by the stratospheric balloon [23]. The system managed to successfully reconstruct the P(Y) code which has not been done in a similar setting before and thus it is step towards proving the usefulness of the technique [23].

3.1.3 The interferometric approach

The interferometric approach is also known by the name PARIS and allows a signal that is virtually unknown to be used as a SOOP for P-RAS. This approach is based of a transmitter to produce the SOOP and a receiver that receives both the direct signal and a reflected version of the signal, which places more requirements on the geometry than the previous two methods. Besides the geometry requirements, [24] claims that the system also is more complicated to implement than the regenerative approach [24].

This provides a major benefit in the form of not requiring extensive knowledge about the signal thus allowing virtually any signal to be used as a SOOP. This opens up the possibility for signals with higher SNR and larger bandwidth than the common GNSS SOOP implemented today [2].

A system that intends to implement the interferometric approach in a space-borne environment is the PRETTY instrument that will be launched in 2021 [6]. Considering airborne systems using the interferometric approach, the instrument IEEC PIR and PIR-A was successful at implementing the PARIS concept [2]. Also worth noting is the implementation using GEO broadcasting satellites discussed in the paper makes use of other SOOPs than GNSS [25].

3.1.4 The partial interferometric approach

The partial interferometric approach is based of the interferometric approach with the addition that it used a priori knowledge to improve the SNR of the direct signal. According to [2] the result is an improved resolution but at the cost of a SNR loss and worse dynamics for delay and Doppler. They described no notable systems that have implemented this type of system yet [2].

3.2 Observables of Passive Reflectometry

In reflectometry most likely a DDM is the aim as it gives spacial resolution and most measurements are made to determine a characteristics of a limited area and thus it

is generally the main objectives of the system. To make such a map a measurement need to be performed and sampled, this is the measurement of a voltage by an ADC (analog to digital converter) and this voltage is the observable of the system. [2] describes the observables in GNSS-R system as the waveform, the waveform peak amplitude or the polarization [2].

The different applications are described in Section 3.3 and they make use of these different observables to derive information. Starting with the DDM as it contains most of the information and thus is a rather complete observable, from it most information can be derived or estimated. The waveform is a cross-section of the DDM in the direction of the delay and it contains the minimum information required for altimeter derivations from the peak of the derivative. Next, the waveform peak amplitude is the peak value of the waveform and contains the minimum information regarding scattering that is required for applications such as wind speed, soil moisture and biomass. Lastly, the ratio between left hand circular polarized (LHCP) and right hand circular polarized (RHCP) contains information that can be used to derive parameters, e.g. wind speed [2].

3.3 Applications

In 1993 Martin-Neíra proposed the use of GNSS-R for altimetry [7], this was one among many types of applications that could meet needs or provide help for different types of fields. Besides altimetry there are today many other applications for GNSS-R where a general P-RAS system could possibly provide improvements and this chapter tends to discuss what applications that exists. Worth remembering is that passive reflectometry is a relatively new field that has yet to be fully explored, perhaps there are major improvements to be discovered by exploring the possibilities.

Besides techniques to sample raw data the data is sampled for a reason, the applications which leads to a need or want from some part of society. While the technique is important in how we manage to sample the data the application-specific parts derive how to process the data, which could differ largely but in many cases it can also overlap.

3.3.1 Altitude measurements

An altimeter is a measurement instrument made to measure the altitude above a set level, in the case of a spaceborne altimeter system the measurement is the distance from transmitter satellite to receiver satellite. A P-RAS system can be used as an altimeter but deriving how it compares with a classic altimeter depends on a lot of parameters. A modern improvement to altimeters are phase altimeters, where the phase information is kept and used to improve the resolution of the measurement [2].

Altimeters have many possible applications but they differ in the requirements, for example it could require absolute altitude or relative altitude with a a 10 mm or 100 m resolution. Applications are various but include ocean levels, tides and snow depth.

3.3.2 Soil moisture measurements

A spaceborne soil moisture measurement can derive the amount of water in the top layer of soil, the top layer depth depends on specifics of the system. Soil moisture measurements have a wide range of applications and is arguably the most interesting application of P-RAS since the technology is mature and it has a lot of potential economic incentives. There are multiple ways to measure soil moisture and here concepts based on interference pattern techniques (IPT) and scatterometry are considered [2].

IPT approaches are based of finding the Brewster angle for the reflected signal, as $\Gamma_v(\theta_{(Brewster)}) = 0$. This can then be related to the soil moisture and the fluctuation amplitude is related to the reflection coefficient and this can be used to make soil moisture maps along the strips of ground defined by the reflection point. An important note by [2] is that this technique requires the satellite to move a notable fraction of its orbit, which may take some time and thus technique this is not feasible for moving spaceborne applications [2].

A scatterometry based approaches make use of the ground reflection which is related to the permittivity ε_r which in turn is affected by the amount of water in the soil. This technique does not require a stationary platform and has been implemented on both airborne and spaceborne platforms for the GNSS-R [2].

3.3.3 Vegetation parameter measurements

A spaceborne system to measure vegetation parameters could be used for measuring vegetation height or the amount of biomass. This mainly have applications in forestry, but as it shares a lot with the soil moisture measurements it is more interesting even if there are limited applications.

The IPT approaches can also be used to provide information on vegetation, assuming attenuation and scattering are weak enough such that the coherent component and ground reflection are detectable. In the example presented by Emery, Camps, and Rodriguez-Cassola this can be used to estimate average vegetation height [2].

A scatterometry based approaches make use of the change in reflectivity Γ which in turn is affected by the amount of biomass. [2] describes a calculated sensitivity of 15 dB per 100 t/ha and makes a reference to the study [26] that agrees with this theoretic sensitivity. This also is dependant on changes in roughness and soil moisture but can still be used to evaluate biomass in areas where there is information regarding these two parameters [2].

3.3.4 Cryosphere measurements

A spaceborne system can be used for a number of cryosphere applications such as; sea ice thickness, sea ice permittivity and dry snow substructure. These measurements are mainly for scientific and meteorological interest. Since the different applications require different types of systems the specifics differ quite a bit, but phase alimeters, IPT or scatterometry systems all have a use in some cryosphere field and could thus be the secondary part of a system.

Measuring sea ice thickness can be used from an altimetric measurement as the carrier phase can be tracked of the reflected signal. Also with an altimetry implementation, dry snow substructures in Antarctica and Greenland can be measured for frequencies that dry snow are transparent to such as the L-Band that GNSS use. This can be done by using multi-layer models to find the dielectric constant gradient which can give information on the most reflective layers [2].

Looking again at scatterometry implementations, the sea ice permittivity and surface roughness are the main variables of the reflection coefficient which relates to the peak power of the reflected EM. Hence a scatterometry model with a priori knowledge about the roughness can be used to derive sea ice permittivity.

3.4 Connecting to Operational, Scientific and Humanitarian Needs

While connecting the possible measurements to needs would require an extensive market research by observing what others have considered it is possible to get a rough outline of what needs that exists out there. [27] made an market analysis based on GNSS-R measurements made using drones, though different from a satellite based system there are still similarities when it comes to the market and possible uses [27].

The market research focused on soil-moisture measurements from a drone, where the they considered three main factors when valuing the market potential. The market potential was evaluated, would the product be able to provide any revenue. Next, the market attractiveness was considered where competition, legal issues and others things where taken into account. Lastly, the complexity was an important factor as the complexity with for example technology or competition increases risk [27].

Soil moisture applications such as irrigation (agriculture), flood/drought (insurance and dam management) and hydrological validation all have good prospects according to [27] and this alone it could motivate looking further into the techniques. But soil moisture measurements often use techniques that can be used for other applications too. One such example is scatterometry where the dielectric constant is considered and measurements of this could be used in different forward models depending on area to find characteristics such as soil moisture, sea surface roughness or the amount of bio-mass in a given area.

4

An Agriculture Soil Moisture PARIS Experiment Using Ku-Band TV-DBS Opportunity Signals

This chapter covers the process of defining, modelling, implementing and performing a seen relevant passive reflectometry experiment. The results are analysed and used to infer the prospects of the techique in question through discussion.

4.1 Defining the Experiment

When trying to define an at the same time purposeful and realistic reflectometry experiment to perform, which explores the prospects of using an opportunity signal for Earth observation, there are quite some factors to consider. Those can be identified as deciding on the type of technique to use, application to investigate, picking a suiting signal source and not least to find a proper measurement setup area. Also, the choices should be made such that to optimise scientific gain and industry interests using the given time and budget resources.

First, looking to the choice of technology (see specifics in Section 3.1), current systems such as the CYGNSS are already using the regenerative approach to map sea winds [3] and the PRETTY mission aims to evaluate the interferometric approach for altimetry [6], both using GNSS opportunity signals [2]. An experiment using X-band Direct-Broadcast Satellite (DBS) signals for sea surface altimetry using the interferometric approach was performed [25]. Quite some extensive research is already being done on regenerative reflectometry systems using GNSS opportunity signals. Therefore, an experiment aimed at investigating the prospects of the interferometric approach (i.e. a PARIS) using some other source is seen to yield more innovative results, possibly expanding on current knowledge.

Continuing onto choosing an application to investigate - as previously mentioned, the applications of current systems and which research is mainly focused on are sea surface wind speed mapping and altimetry. Studies of CYGNSS measurements acquired over land masses have also indicated relative soil moisture mapping to be prominent using GNSS signals [28], while there seem to be no current dedicated such systems yet. Furthermore, a market study (for drones) has concluded various soil moisture measurement applications to be attractive remote sensing applications [27].

Meanwhile, the passive reflectometry technology potentially offers greater coverage and much shorter revisit times than the current active remote sensing systems. Also, soil moisture measurements are derived mainly from the energy or SNR observable of the processed result, making it one of the more "straightforward" applications to implement. Motivated by this, the focus of this experiment is chosen to be set towards a soil moisture mapping application. Although a calibrated such system is out of the scope of this thesis due to its complexity, just to bring indications on its prospects is considered desirable to explore the potential of possible future systems.

Then, it is needed to identify an appropriate opportunity signal source to use with the technique for this application. Some interesting properties to consider are e.g. the carrier frequency, bandwidth, transmit power, source orbit and availability of this signal. A large bandwidth and transmit power are mainly wanted to provide a good enough resolution and signal detectability respectively, while the preferred carrier frequency and availability of a source is to be determined more by scientific or industry interests. The orbit and availability in turn determine the possible coverage of a system using the signal in question. Current research revolves mainly around the use of “lower” carrier frequencies, such as that of GNSS signals at about 1.2 to 1.6 GHz, but those signals have a relatively small bandwidth compared to many higher carrier frequency systems in orbit, such as mobile communications or TV-DBS satellites, which transmit at X-band and above. Also, planned telecom satellite mega constellations such as SpaceX’s Starlink or Amazon’s Kuiper system are supposed to use Ku-, K-, Ka- and even V-band for large bandwidth communications [11], [12]. This indicates a scientific and industrial interest of evaluating the prospects of using higher carrier frequency signal sources for reflectometry and scatterometry applications. Still, the experiment is seen to be limited to a stationary setup due to available time and budget. Also, due to the purpose of simplification of setup and evaluation, a GEO signal source is seen as the most prominent candidate. The opportunity source decided on is hence the Ku-band TV broadcasting signals of Astra 4A located at a carrier frequency around 11.9 GHz [10]. It has channel bandwidths of 33 MHz with 40 MHz allocated for the channel and a total of 52 Ku-band transponders [29]. The satellite is covering most of Europe within its transmission beam. Bear in mind that there are other very similar opportunity signal candidates available as well, with different TV-DBS transmitting to most of the landmasses of the Earth.

Lastly, a suitable and available area where to perform the experiment at is needed, which is easier said than done. After quite some consideration, contacts were established with the World Heritage Grimeton Radio Station and they agreed on allowing us to install the experiment setup in one of their six 127 meters high antenna towers. The antenna towers span a total of 2.2 km, which resemble the last remaining active long wave transmitter in the world (hence it being announced a world heritage) [30]. The radio station is located nearby the city of Varberg at the Swedish west coast and the area is pretty much optimal for this specific experiment. The ground area around the towers is flat and covered with agricultural fields and grazing cattle, while the towers themselves provides the height needed to both resolve a significant ground area in size (possibly observing several resolution delay lines) and to separate direct path leakage correlation with that of the resolved area in

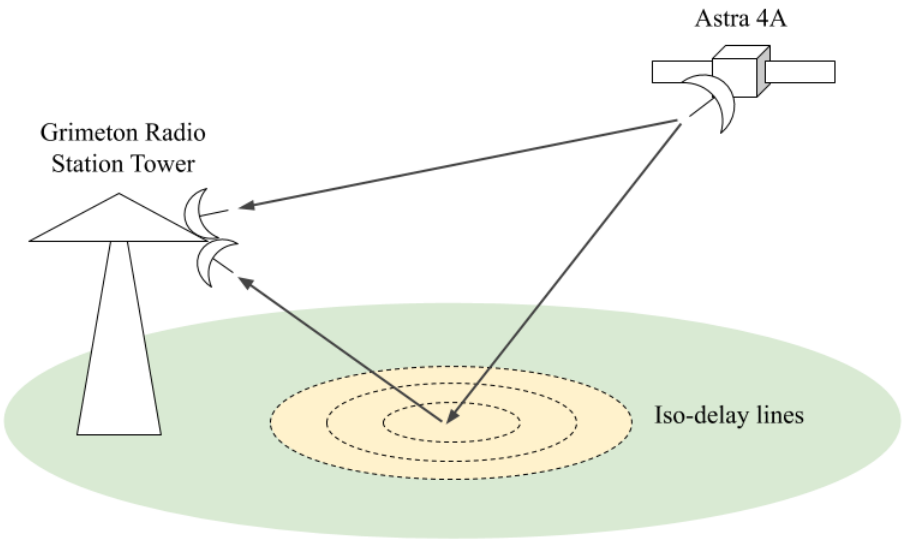

Figure 4.1: A basic visualisation of the experiment setup. As can be seen, two parabolic antennas are mounted on top of the Grimeton Radio Station antenna tower, at a height of 120 m above the ground surface. One antenna is aimed directly at Astra 4A, collecting the direct signal from the satellite, while the other is aimed at the ground, acquiring any reflected signal. The size and location of the objects in the figure are not in relative scale.

the delay map. There are of course many precautions to take when installing and running an experiment literally inside of an over 100-meter-high active 200 kW transmitter, both regarding EMC and personal safety. Further details on this is covered throughout the later more technical sections.

To summarize, as the title of this chapter suggests, a PARIS technique system using the Ku-band opportunity signals of the GEO TV-DBS Astra 4A is designed and implemented and its prospects for measuring agriculture soil moisture is tested experimentally. The basic experiment setup idea is visualized in Figure 4.1. This is seen to connect to the purpose of this thesis by providing both experimental results and experience to evaluate the system models and the PARIS technique, exploring its potential for soil moisture mapping using Ku-band opportunity signals. The resulting conclusions can then be connected to the broader picture, extrapolating indications on what performance to be expected from e.g. an imagined future LEO small satellite Earth observation constellation using this technique for soil moisture mapping.

The experiment is accomplished as described in the following sections of this chapter. It starts with an initial pilot study of the experiment prospects, which is providing the theoretical foundation and pinpointing its feasibility together with the expected results. It then continues onto describing the design and implementation of the system hardware and software. Then follows some system verification tests, before presenting the results from the experiment at Grimeton Radio Station. Thereafter, the results are analysed and discussed, and possible conclusions are drawn.

4.2 Experiment Pilot Study

To investigate the feasibility of performing the experiment at Grimeton Radio Station, its expected results are indicated by creating a full theoretical system model as a foundation to estimate those. Parts that need to be taken into account in this model are the setup geometry, the resolution cell size and location and the effects of atmospheric propagation and surface reflection on the signal. Also included is an analysis of the resulting bi-static radar system, the expected receiver front-end performance and calculations of the noise and signal power levels. Finally, the digital system is characterised by analysing the effects of the coherent and non-coherent integration processing techniques. By connecting all these parts, an end measurement result SNR is estimated, which puts foundation for the expected system performance. Just to indicate if measurements seem possible to obtain or not in this experiment setup is considered a desired result. To simplify the calculations, emphasis is put on deriving this result for the special case of a measurement setup observing the specular reflection point on the ground.

As many realistic assumptions about appropriate properties are needed for e.g. the system hardware components, such as the antenna gain and 3-dB main lobe width and the possible sampler memory depth, to yield an end result, the general system hardware design (see Section 4.3) was developed in parallel with this study. Although, the modelling is made such that different component parameters are kept general, allowing for system component (especially antennas) end result effect and requirement analysis.

Before delving into the modelling, some initial general parameters can be specified for this experiment setup. Those are summarized in Table 4.1 and consists of some physical constants, angles from Grimeton Radio Station to Astra 4A derived from their coordinates and a couple of signal properties, such as carrier frequency, bandwidth and equivalent isotropically radiated power (EIRP) [10].

Table 4.1: List of some general experiment parameters. The different angles are derived from the Grimeton Radio Station coordinates 57.105 N, 12.388 E.

Parameter	Value	Description
c	$3 \cdot 10^8$ m/s	Approx. speed of light
k_B	$1.38 \cdot 10^{-23}$ $\frac{m^2 kg}{s^2 K}$	Approx. Boltzmann constant
ϕ_ε	24.74°	Elevation angle, `https://satlex.de`
θ	189.09°]	Azimuth angle, `https://satlex.de`
θ_G	57.105°	Grimeton latitude
r_{GEO}	42156 km	GEO orbit radius
r_e	6370 km	Earth radius
f_1	11.881 GHz	Astra 4A carrier frequency 1
f_2	11.919 GHz	Astra 4A carrier frequency 2
λ	2.52 cm	Astra 4A carrier wavelength
EIRP	50 dBW	Astra 4A channels EIRP
B	33 MHz	Astra 4A channel bandwidth

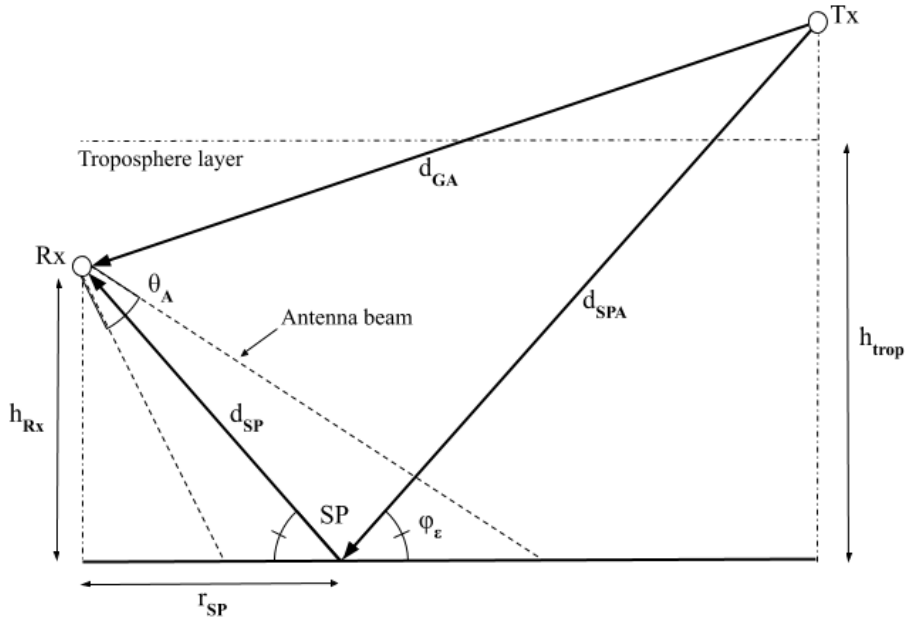

Figure 4.2: An illustration of the experiment setup geometry, where Rx is the point of the receiver antennas, Tx the seen signal opportunity source TV-broadcasting satellite Astra 4A and SP the specular point of reflection on the ground.

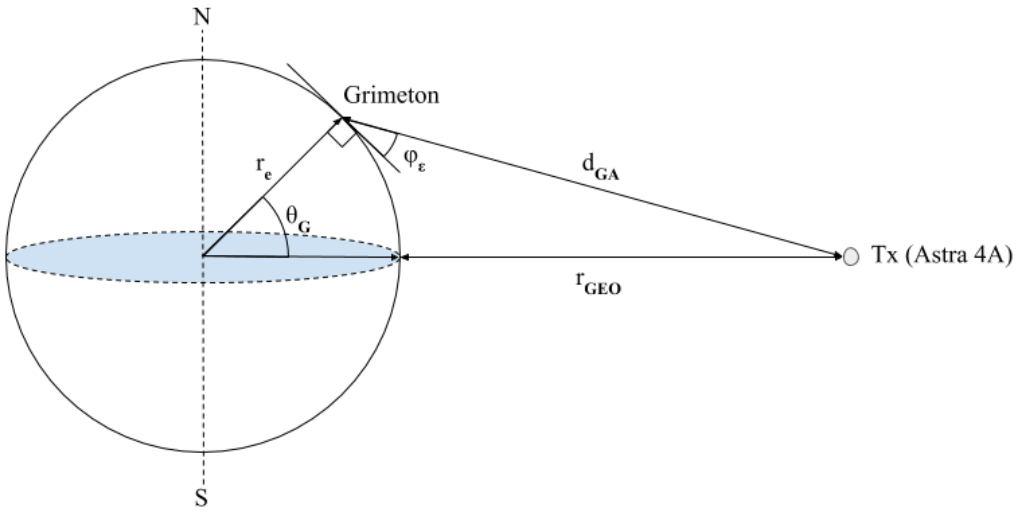

Figure 4.3: An illustration of the zoomed-out view of the measurement setup, with G being the point on the Earth surface where the Grimeton radio station is located and A the point in geostationary orbit of the TV-broadcasting satellite Astra 4A.

4.2.1 Geometry calculations

The experiment setup geometry models are illustrated in figures 4.2 and 4.3, as observed in a "near-ground" and "out-in-space" perspective respectively. Given the height of the receiver above ground h_{Rx}, the respective elevation and azimuth angles to the satellite, ϕ_ε and θ, as well as the Grimeton latitude θ_G, the different distances d_{SP}, r_{SP}, d_{GA} and d_{SPA} can using trigonometry be expressed as

$$d_{SP} = \frac{h_{Rx}}{\sin \phi_\varepsilon}, \tag{4.1}$$

$$r_{SP} = \frac{h_{Rx}}{\tan \phi_\varepsilon}, \tag{4.2}$$

$$d_{GA} \approx \sqrt{r_{GEO}^2 + r_e^2 - 2 r_{GEO} r_e \cos \theta_G}, \tag{4.3}$$

$$d_{SPA} \approx d_{GA}, \tag{4.4}$$

where d_{SP} is the distance from the receiver to the specular reflection point center and r_{SP} the corresponding range projected onto the ground plane. d_{GA} and d_{SPA} are the distances from receiver and specular reflection point center to the signal source satellite Astra 4A, respectively. For the purposes of this study d_{SP} and d_{SPA} can be approximated as being equal, while Equation 4.3 is also a sufficient approximation with an uncertainty greater that the difference between those two distances. Some computed values of the parameters covered in this section are concluded in Table 4.2.

Table 4.2: Values of some experiment setup geometry parameters.

Parameter	Value	Description
h_{Rx}	120 m	Assumed
h_{trop}	10 km	Assumed
d_{SP}	287 m	Equation
r_{SP}	260 m	Equation
d_{GA}	39 065 km	Equation
d_{SPA}	39 065 km	Equation

4.2.2 Resolution cell calculations

Since the experiment setup is stationary, there are only iso-delay lines and no iso-Doppler lines present. The two main factors defining the resolved area around the specular point is hence the signal bandwidth B and the antenna beam width θ_A. If the resolution defined by the antenna beam is smaller than that of the bandwidth, the resolution is said to be beam-limited and vice versa bandwidth-limited if this is not the case.

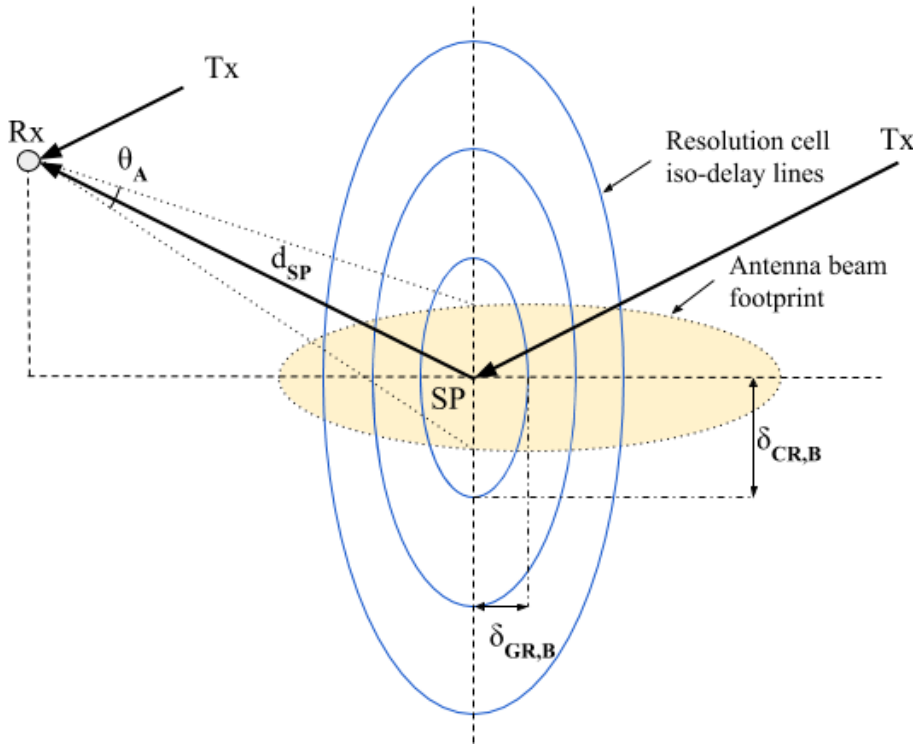

Figure 4.4: An illustration of the expected principal shape of resolution cells within the resolved area (ground area covered by the antenna beam footprint) in the experiment. Since the experiment is stationary, no iso-Doppler lines are present. This is basically a birds view of the SP point region in Figure 4.2. δ_{CR} is marked as the bandwidth-limited cross-range radius of the specular iso-delay ellipse, but the cell is clearly limited in cross-range by the antenna beam footprint.

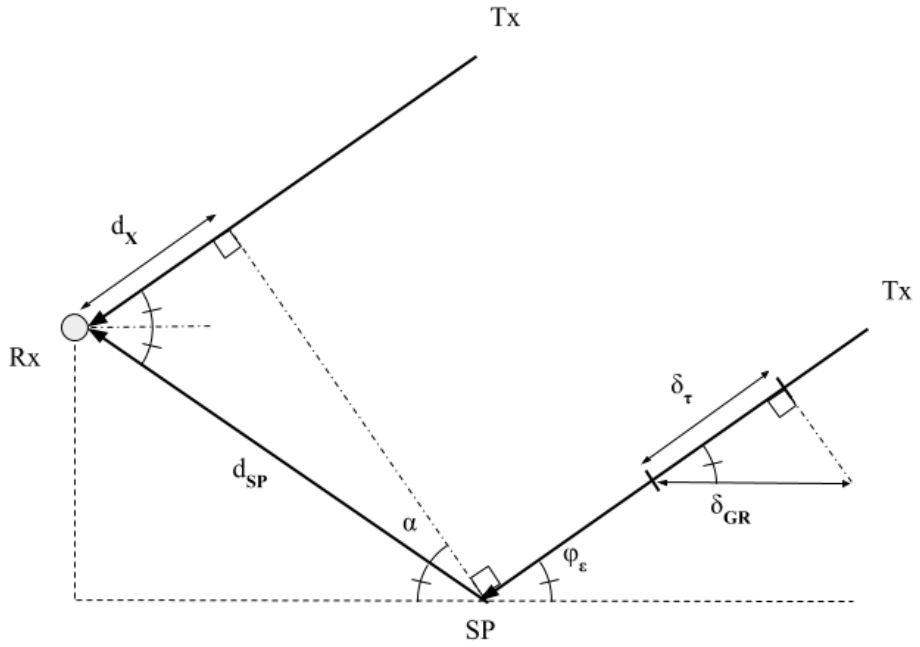

(a) An illustration of the bandwidth-limited ground range resolution.

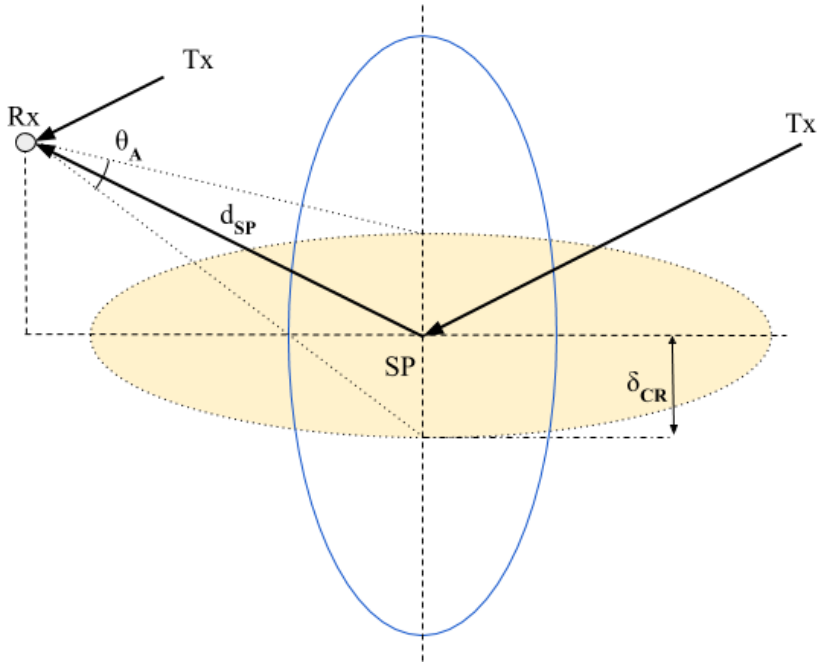

(b) An illustration of the beam-width-limited cross range resolution.

Figure 4.5: Illustrations of beam and bandwidth limitations of resulution cells in cross respectively ground range.

A probable resolution cell appearance for this experiment is illustrated in Figure 4.4 and this is used to derive the resolution cell equations. To determine the ground-range resolution δ_{GR} and cross-range resolution δ_{CR} dimensions as shown in the figure, the beam and bandwidth resolution cell limitations of in each dimension is calculated. To start with, assuming a antenna beam width of 5.8°, the beam limited ground and cross range resolution dimensions δ_{GR,θ_A} and δ_{CR,θ_A} can be approximated as

$$\delta_{GR,\theta_A} \approx \frac{d_{SP}\sin(\theta_A/2)}{2}\left(\frac{1}{\sin(\phi_\varepsilon+\theta_A/2)}+\frac{1}{\sin(\phi_\varepsilon-\theta_A/2)}\right)\approx 36 \text{ m}, \tag{4.5}$$

$$\delta_{CR,\theta_A} = d_{SP}\tan(\theta_A/2) = 14.5 \text{ m}, \tag{4.6}$$

where d_SP is the distance from the receiver to the specular point and ϕ_ε the elevation angle to the signal source satellite. The beam-limited cross-range resolution case is shown in Figure 4.5b.

In turn, the bandwidth-limited ground range and cross range delay resolution, $\delta_{GR,B}$ and $\delta_{CR,B}$, require some more steps derive expressions for. There are three beam-limited resolution domains that need be transformed in between. As is illustrated in Figure 4.5a, the ground range resolution δ_{GR} is dependent on the slant range resolution δ_τ. However, the slant range resolution is dependent on the signal bandwidth through the resolvable difference between the direct and the reflected paths propagated distances. That is, the path difference at the center of the specular point, Δl, can be expressed as

$$\Delta l = d_{SP} - d_x = d_{SP}(1-\cos(2\phi_\varepsilon)) = 100 \text{ m} \tag{4.7}$$

which is also corresponding to a difference in delay of 333 ns, while the path difference resolution δ_l is defined from the signal bandwidth B as

$$\delta_l = \frac{c}{2B} \approx 4.54 \text{ m}, \tag{4.8}$$

where c is the speed of light. Assuming the distance from the receiver to the specular point center d_{SP} to be much larger than the slant range resolution δ_τ, the slant range resolution (along d_{SP}) dependence on the path difference resolution can be approximated around the specular point centre by rearranging Equation 4.7 and inserting Equation 4.8 in place of d_{SP} as

$$\delta_\tau \approx \frac{\delta_l}{1-\cos(2\phi_\varepsilon)}, \approx 13.0 \text{ m} \tag{4.9}$$

which can be used to compute the ground range bandwidth limited resolution according to

$$\delta_{GR,B} = \frac{\delta_\tau}{\cos\phi_\varepsilon} \approx 14.3 \text{ m}. \tag{4.10}$$

By following a very similar chain of arguments, the beamwidth-limited cross range resolution $\delta_{CR,B}$ can, using the illustration in Figure 4.5 (b), be derived and calculated from the path difference resolution δ_l as

$$\delta_{CR,B} \approx \sqrt{\delta_l^2 + 2\delta_l d_{SP}} = 51.2 \text{ m} \tag{4.11}$$

Also, it can be worth noting that a number n of resolved delay-lines in ground range is possible for an antenna beam-width θ_A of at least

$$\theta_A(n) = 2\sin^{-1}\left(\frac{n\delta_{GR}\sin\phi_\varepsilon}{\sqrt{d_{SP}^2 + (n\delta_{GR})^2 - 2d_{SP}n\delta_{GR}\cos\phi_\varepsilon}}\right), \tag{4.12}$$

assuming that the antenna beam footprint border closest to the receiver along the ground plane is limiting the ground range number of delay lines resolved and that the sum of resolved distance along the ground range is much smaller than that of the distance from the receiver to the specular point.

To summarize, the resolution cell is bandwidth-limited in the ground range and beam-limited in the cross range respective dimensions. Some computed values of the parameters covered in this section are concluded in Table 4.3.

Table 4.3: Values of some experiment resolution cell parameters.

Parameter	Value	Description
Δl	100 m	Dir. & refl. path diff.
δ_l	4.54 m	Path diff. res.
δ_τ	13.0 m	Slant range res.
δ_{GR}	14.3 m	Ground range res.
δ_{CR}	14.5 m	Cross-range res.

4.2.3 Propagation losses

The main contributors to the signal propagation losses are seen to be that of the free-space propagation loss and the absorption loss due to water vapour and oxygen content in the troposphere. The direct path signal from the satellite Astra 4A to the receiver is affected by a free-space loss, $L_{fs,GA}$, and an atmospheric absorption loss, L_a. Similarly, the reflected path signal from the satellite to the specular point is also affected by a free-space propagation loss, $L_{fs,SPA}$, and an about equal absorption loss, since the Grimeton radio station antenna tower height of 120 m is approximately at ground level when compared to the height of the troposphere (which is assumed to about 10 km). Additionally, the reflected path signal is affected by a second free-space loss, $L_{fs,SP}$, when after reflection propagating from the specular point to the receiver antenna.

To start with, the free-space loss formula is given as

$$L_{fs} = (\frac{4\pi d}{\lambda})^2, \tag{4.13}$$

where d is the propagated distance of the signal from its source and λ the wavelength. The three free-space propagation losses $L_{fs,GA}$, $L_{fs,SPA}$ and $L_{fs,SP}$ can thereby be calculated. The first two of those can be approximated as equal due to their relatively similar distance to the satellite, which gives

$$L_{fs,GA} \approx L_{fs,SPA} \approx (\frac{4\pi d_{GA}}{\lambda})^2 = 205.65\ dB, \tag{4.14}$$

and the last one is calculated as

$$L_{fs,SP} \approx 4\pi d_{SP}^2 = 60.1\ \text{dB}, \tag{4.15}$$

where the term $4\pi/\lambda^2$ is left out since this path loss component (effective antenna area) is already included in the connected $L_{fs,SPA}$ part.

Moving on to the last component, the atmospheric absorption loss for Earth-space paths with elevation angles ϕ_ε from 5° up to zenith can be approximated as

$$L_a = 10^{A/(10 \sin \phi_\varepsilon)}, \tag{4.16}$$

where A is the zenith tropospheric attenuation in dB due to oxygen and water vapour content γ_o and γ_w given as

$$A = h_{trop}(\gamma_o + \gamma_w), \tag{4.17}$$

for an assumed troposphere height of h_{trop} of about 10 km. ITU recommendations on the calculation of Earth-space atmospheric propagation loss suggest a total zenith attenuation A of 0.23 dB to be expected for frequencies around 11.9 GHz [31]. This implies the result, using equation 4.16, $L_a \approx 0.55$ dB. Some computed values of the parameters covered in this section are concluded in Table 4.4.

Table 4.4: Values of some experiment propagation losses parameters.

Parameter	Value	Description
$L_{fs,GA}$	205.65 dB	GA FS-loss
$L_{fs,SPA}$	205.65 dB	SPA FS-loss
$L_{fs,SP}$	60.1 dB	SP FS-loss
L_a	0.55 dB	Atm. prop. loss

4.2.4 Surface reflection losses and effects

The total outgoing by incoming power ratio of an EM wave being reflected off a rough soil surface can be modelled as

$$R = \rho_r^2 \cdot R_0, \tag{4.18}$$

where ρ_r is a factor modelling the surface scattering effects and R_0 is the power reflection coefficient, which is also dependent on the considered wave polarization. The reflection loss is hence described as

$$L_r = R^{-1}. \tag{4.19}$$

The following subsections aim to clarify expressions or derive good enough approximations of these factors to enable an evaluation of the experiment prospects.

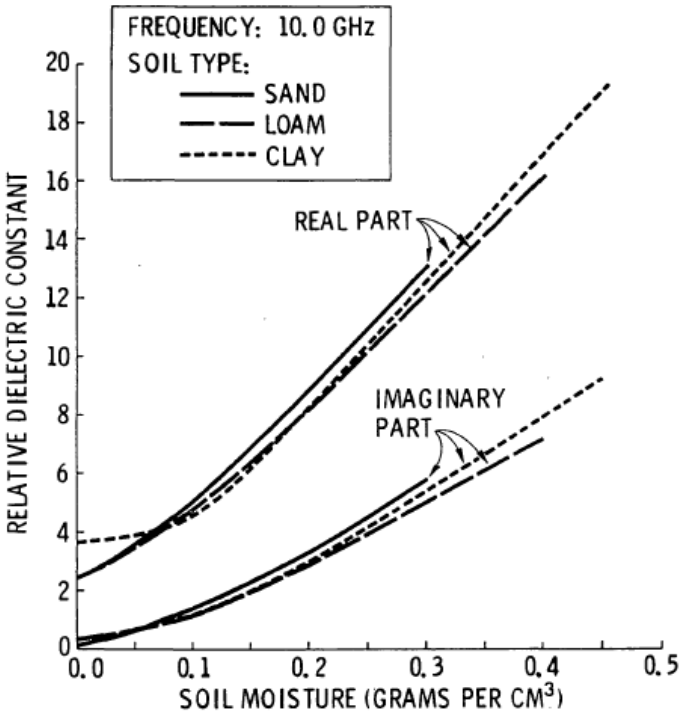

Figure 4.6: Graph describing the relative dielectric constant for different soil types as a function of soil moisture. Figure is taken from [32] and is used with permission from Professor Ulaby and NASA [32].

4.2.4.1 Soil dielectric properties

Results of the relative permittivity of soil as dependent on its water content by weight can be seen in Figure 4.6. It is seen to be relatively independent of common soil types and as of frequencies within the range of 0.13 GHz to 37 GHz [32]. Also, the permittivity itself is seen to almost linearly increase for soil water content by volume percentages from 0 % to 47 %, within the interval

$$\varepsilon_{soil} \in [2.5 + j0.2, 20 + j9]. \tag{4.20}$$

A rough approximate of the soil relative permittivity ε_{soil} for the frequency 11.9 GHz as dependent on moisture content $\eta_w \in [0, 0.47]$ can then be modelled as

$$\varepsilon_{soil}(\eta_w) \approx 2.5 + j0.2 + \eta_w \cdot \frac{(19.8 + j8.8)}{0.47}. \tag{4.21}$$

Representative values of the relative permittivity for higher soil moisture levels are not presented in the study, but it should increase until it eventually approaches that of water $\varepsilon_{water} \approx 60 + j33$ (which would indicate flooding). The details of this behaviour can be further looked into, but the values presented are considered as good enough approximations for the purpose of determining the overall prospects of the experiment.

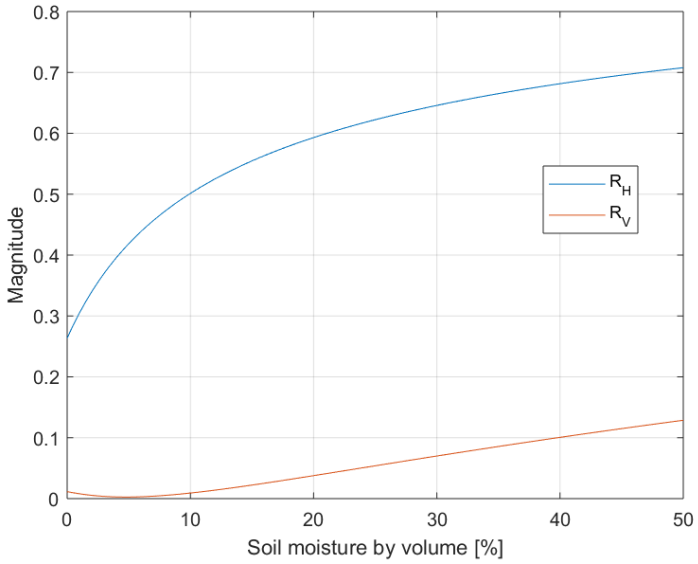

Figure 4.7: The horizontal and vertical power reflection coefficients, R_H and R_V respectively, are shown as a function of soil moisture by volume. An elevation angle of 24.7° is assumed to obtain this result.

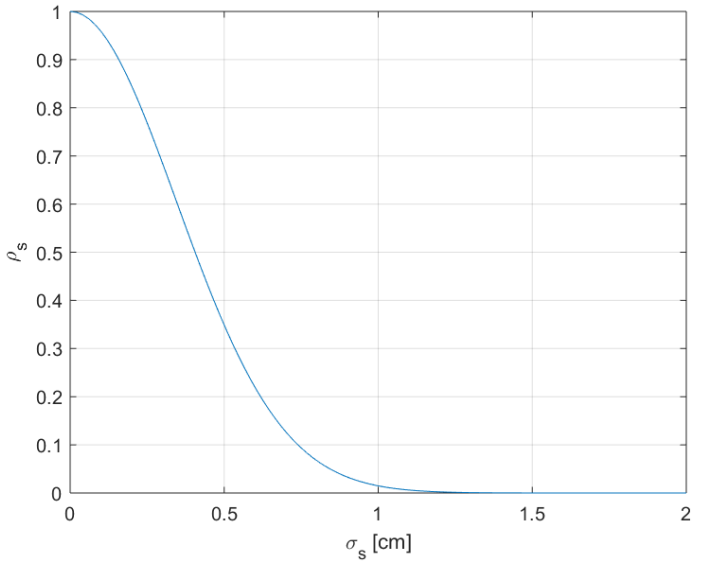

Figure 4.8: A model of the specular scattering factor ρ_s as a function of the surface height standard deviation around the local mean σ_s for a frequency of 11.9 GHz.

4.2.4.2 Power reflection coefficient

Given the relative dielectric constant ε of a material, the ratio of the incident and reflected power of an EM wave, assuming a perfectly smooth surface, is given by the Fresnel equations as

$$R_{0,H} = \left| \frac{sin(\phi) - \sqrt{\varepsilon - cos(\phi)^2}}{sin(\phi) + \sqrt{\varepsilon - cos(\phi)^2}} \right|^2 , \tag{4.22}$$

$$R_{0,V} = \left| \frac{\varepsilon \cdot sin(\phi) - \sqrt{\varepsilon - cos(\phi)^2}}{\varepsilon \cdot sin(\phi) + \sqrt{\varepsilon - cos(\phi)^2}} \right|^2 , \tag{4.23}$$

where ϕ is the elevation angle of the incident wave to the surface plane. These reflection power coefficients are shown in Figure 4.7 as a function of soil moisture according to the model derived for the relative dielectric constant presented in Equation 4.21. Using the elevation angle to the satellite Astra 4A ϕ_ε as ϕ in the Fresnel equations and assuming a soil moisture by volume content of 0 % results in about $R_{0,H} = 0.264$ and $R_{0,V} = 0.011$, which clearly indicates that the horizontal polarization component should be used for measurements in the experiment.

4.2.4.3 Surface scattering

When the surface upon which the EM wave is reflected is not perfectly smooth, a reflection factor ρ_r can be introduced to model the resulting effects on the reflected power. An overview of EM wave surface reflection and scattering effects by ITU can be found in [33]. When considering reflection off rough surfaces, a simple model suggests defining the specular as well as the diffuse reflection factors, ρ_s and ρ_d, as the two contributing factors to the total reflected field RMS power ratio $< \rho_r >^2$ as

$$< \rho_r >^2 = < \rho_s >^2 + < \rho_d >^2 . \tag{4.24}$$

The specular reflection factor ρ_s is the coherently reflected part of the signal in the plane of incidence, which is complex to determine exactly. Although, a common quantitative approximation is

$$\rho_s = e^{-1/2g^2}, \tag{4.25}$$

where g is the Rayleigh roughness criterion. This is defined as

$$g = 4\pi(\sigma_s/\lambda)sin(\phi), \tag{4.26}$$

where σ_s is the surface height standard deviation in relation to its local mean within the first Fresnel zone (i.e. the area within which the signal path difference from the middle to the edge is below about $\lambda/2$), λ is the wavelength and ϕ is again the elevation angle. A common guideline is that a surface can be considered smooth when $g < 0.3$ (which also implies $\rho_d \approx 0$). ρ_s as a function of σ_s for a frequency of 11.9 GHz according to Equation 4.25 is shown in Figure 4.8. It can be noted that the model implies the specular reflection factor to die off for surface roughness standard deviations larger than about 0.5 cm.

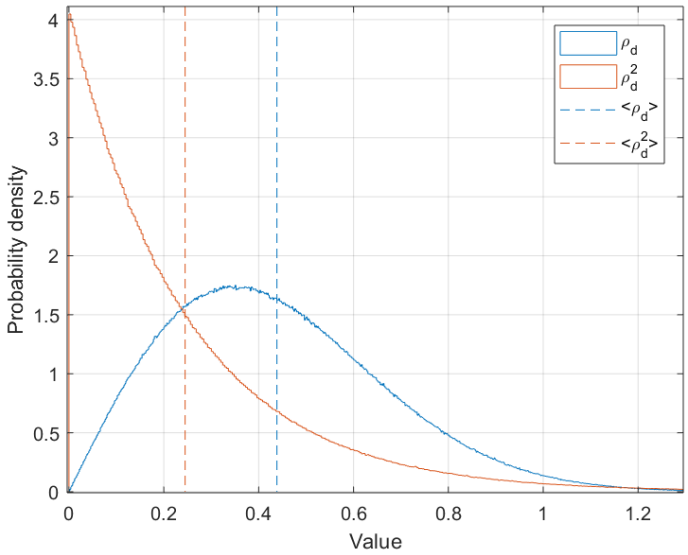

Figure 4.9: The diffuse scattering factor ρ_d PDF given that it behaves as a Rayleigh distribution with a mode of 0.35 and its squared transform PDF ρ_d^2 computed by a Monte Carlo simulation using 10^7 samples. The means of the distributions are illustrated with the dashed lines of corresponding colours.

The diffuse reflection factor ρ_d is even more complex to determine precisely than the specular one, since it depends heavily on the specific resolved surface topology. It is more appropriately defined as a statistically random parameter belonging to a Rayleigh distribution. Measures of ρ_d for low directivity antennas (the resolved area is much larger than the first Fresnel zone) over very rough bare ground and sea surfaces indicates it to vary in between 0.2 (-14 dB) and 0.4 (-8 dB), with a most probable value of 0.35 (-9.1 dB) [33]. Mind that the ρ_d linear value is a magnitude while the dB values are in power (i.e. square it in the transform). This implies the diffuse reflection factor in this case can be describe as

$$\rho_d \sim Rayleigh(\sigma_R)|_{\sigma_R=0.35}, \tag{4.27}$$

where σ_R is the Rayleigh mode, and hence its resulting power ratio according to an exponential distribution as

$$\rho_d^2 \sim Exp(\frac{1}{2\sigma_R^2})|_{\sigma_R=0.35}, \tag{4.28}$$

with a mean value of

$$\mathbb{E}\{\rho_d^2\} = 2\sigma_R^2 \approx -6.1 \text{ dB}, \tag{4.29}$$

Although, bear in mind that

$$\mathbb{E}\{\rho_d\}^2 = (\sigma_R\sqrt{\pi/2})^2 \approx -7.2 \text{ dB}, \tag{4.30}$$

is the power of the Rayleigh distributed mean, while the most probable reflection factor power ratio is still $\rho_d^2 = \sigma_R^2 = -9.1$ dB. The corresponding distributions and their means are shown in Figure 4.9.

This reflected signal observation effect is commonly referred to as speckle noise. If either the transmit antenna, receiver antenna or the resolved area are moved enough, ρ_d becomes uncorrelated relative to its previous value. Multi-look techniques can be used to combine independent observations to suppress this effect for the purpose of inferring the underlying reflectivity of the surface material.

Some computed values of the parameters covered in this section are summarised in Table 4.5. It is obvious from the computed values of the power reflection coefficients presented that the experiment should aim to use the horizontal polarisation of the reflected signal.

Table 4.5: Values of some experiment surface reflection effects parameters.

Parameter	Value	Description
$R_{0,H}$	-5.79 dB	0 % SM
...	-2.27 dB	20 % SM
...	-1.67 dB	40 % SM
...	-0.86 dB	100 % SM (water)
$R_{0,V}$	-19.4 dB	0 % SM
...	-14.2 dB	20 % SM
...	-10.0 dB	40 % SM
...	-4.94 dB	100 % SM (water)
σ_R	0.35	Rayleigh mode of ρ_d

4.2.5 The bi-static radar system

The power of the reflected signal behind its receiver antenna can be described by the bi-static radar equation as

$$P_r = \frac{EIRP \cdot G_r \cdot \sigma_{RCS}}{L_{SP} \cdot L_{SPA}} = \frac{EIRP \cdot G_r \cdot \sigma_{RCS}}{L_{fs,SP} \cdot L_{fs,SPA} \cdot L_a}, \tag{4.31}$$

where $EIRP$ is the equivalent isotropicallt radiated power of the transmitter, G_r the receiver antena gain„ σ_{RCS} the radar cross section of the resolved area and L_{SPA} and L_{SP} the propagation losses from the specular reflection point to the transmitter satellite Astra 4A and the receiver respectively. All parameters but the radar cross section and receiver antenna gain are previously covered and the antenna gain is a chosen hardware component property. Therefore only the radar cross section σ_{RCS} remains to be calculated. Its dependence can be described as

$$\sigma_{RCS} = R \cdot A_{RC}, \tag{4.32}$$

where R is the surface power reflection and A_{RC} the area of the resolution cell. While this expression can seem simple, its components might prove tedious to compute accurately. First, the power reflection R is (as covered in the previous

section) both of a probabilistic nature and might be dependent on the difference in angle to the receiver for different points in the resolution cell. Also, the resolution cell itself introduces some implications dependent on if it is beam-limited or not in any dimension, since the resolved area of the resolution cell then is not too simple to determine in a more exact sense. In addition to this, since the receiver antenna beam width defines the resolution cell area in the beam-limited case, variations of the antenna gain G_r will be seen for different points in the resolution cell area (and some power contribution might come from outside of the area), which further complicates the determination of the received power level P_r.

For the case where diffuse scattering is the dominant reflection factor R while the resolution cell area A_{RC} also is beam-limited in the cross-range dimension only a hopefully sufficient (neither too sceptical nor too optimistic) approximation for obtaining the specular point resolution cell area would be proposed as the following. As is interesting as it seems to be the case for this experiment. Defining the resolution cell area $A_{RC,0}$ as the area enclosed within an ellipse with a ground range radius defined by the bandwidth-limited ground range resolution of the system and the cross-range radius defined from the specular point to the 3-dB cross-range beam-width line. It would then be described as

$$A_{RC,0} \approx \pi \cdot \delta_{GR} \cdot \delta_{CR} \approx 652 \text{ m}^2, \tag{4.33}$$

where δ_{GR} and δ_{CR} are the ground-range bandwidth-limited and the cross-range 3-dB beam-limited resolutions respectively. How these are obtained is described in the resolution cell calculations section. This implies the approximated area to actually be smaller than the true one since the edges are cut off. In the case of a fairly narrow beam, the true area could even prove to be more of a rectangular shape. Anyway, the thought of this obviously sceptical approximation is that it would then approximately account for some of the power loss due to the antenna gain variation close to the edges of the area as compared to a model using a fixed such.

Combining this result with the expected power reflection coefficient R for an assumed 0 % soil moisture, as is derived in the previous surface reflection effects section, yields the expected radar cross section

$$\mathbb{E}\{\sigma_{RCS}\} = R_{0,H} \cdot \mathbb{E}\{\rho_d^2\} \cdot A_{RC,0} \approx 42, \tag{4.34}$$

but keep in mind that ρ_d is an exponentially distributed random variable and hence prone to vary greatly. Computed values of the parameters covered in this section are summarised in Table 4.6.

Table 4.6: Values of some experiment bi-static radar system parameters.

Parameter	Value	Description
$A_{RC,0}$	652 m^2	Ellipse approx.
$\mathbb{E}\{\sigma_{RCS}\}$	42	Calculated

4.2.6 The receiver front-end

The receiver front-end system design is covered in detail in section 4.3 and it is shown in Figure 4.13. But for now, it is seen as enough to simply characterise it by its resulting total noise figure F_{Rx}. This can be approximated as the noise figure of the first few high-gain components of the signal chain, i.e. the low-noise block (LNB) and the first line amplifier. The resulting noise figure of the RF front-end system, F_{Rx} is hence calculated as

$$F_{Rx} = F_{LNB} + \frac{F_{LineAmp} - 1}{G_{LNB}} + ... \approx 1.2\,\text{dB}, \tag{4.35}$$

where F_{LNB} and $F_{LineAmp}$ are the LNB and line amplifier respective noise figures and G_{LNB} the gain of the LNB.

Furthermore, the total system gain G_{Rx} for each signal chain is adjustable such that the voltage levels inputted to the sampler should be on the order of some mV. The gain settings are dependent on the sum of the signal and noise power at each sampler input channel, of which the resulting voltages can be calculated as

$$V = \sqrt{\frac{N+P}{Z}} = \sqrt{\frac{G_{Rx}(N_{in}F_{Rx} + P_{in})}{Z}}, \tag{4.36}$$

where N is the noise power, P the signal power and Z the system impedance, all at the input of the sampler. N_{in} and P_{in} are the respective input noise and signal power levels on the input to the RF front-end, then propagating through the system signal chains to the sampler. Since there are two signal chains, one for the direct path signal ("d"-subscript) and one for the reflected path signal ("r"-subscript), there are four power level components at the input to the sampler: N_d, P_d, N_r and P_r. They are calculated as

$$N_d = N_{d,in}F_{Rx}G_{Rx,d}, \tag{4.37}$$

$$N_r = N_{r,in}F_{Rx}G_{Rx,r}, \tag{4.38}$$

$$P_d = P_{r,in}G_{Rx,d}, \tag{4.39}$$

$$P_r = P_{r,in}G_{Rx,r}, \tag{4.40}$$

in terms of the four input powers to the receiver system, $N_{d,in}$, $P_{d,in}$, $N_{r,in}$ and $P_{r,in}$, which are to be derived in the following two sections.

4.2.7 Noise power calculations

The noise power observed behind the receiver direct path and reflected path antennas can be described using their respective noise temperatures, T_d and T_r. The direct path noise temperature is calculated as

$$T_d = \eta_A \cdot T_{sky,observed} + (1 - \eta_A) \cdot T_{sys}, \tag{4.41}$$

and similarly the reflected path noise temperature as

$$T_r = \eta_A \cdot T_{ground} + (1 - \eta_A) \cdot T_{sys}, \tag{4.42}$$

where η_A is the antenna efficiency, T_{sys} the receiver system temperature, $T_{sky,observed}$ the observed sky temperature by the direct path antenna and T_{ground} the observed temperature by the reflected path antenna (since it is aimed at the ground). In turn, $T_{sky,observed}$ is calculated as

$$T_{sky,observed} = T_{sky} \cdot L_a^{-1} + T_a \cdot (1 - L_a^{-1}) + T_{leak}, \tag{4.43}$$

where $T_{sky} = 8$ K is the clear sky temperature, L_a is the atmospheric absorption loss, $T_a = 275$ K is the tropospheric water vapour and oxygen temperature and $T_{leak} = 20$ K is a term compensating for some ground noise temperature expected to leak in through the direct signal path antenna side-lobes [31]. The resulting direct path noise temperature T_d is then 156 K and that of the reflected path, T_r, is 300 K

Given these noise temperatures, the noise power at the receiver system respective direct and reflected signal path inputs, $N_{d,in}$ and $N_{r,in}$, can then be calculated using the Rayleigh-Jeans approximation as

$$N_{d,in} = k_B T_d B \approx -131.5 \text{ dBW}, \tag{4.44}$$

and

$$N_{r,in} = k_B T_r B \approx -128.6 \text{ dBW}, \tag{4.45}$$

where k_B is the Boltzmann constant and B the noise bandwidth, here assumed to be that of the signal since the values are to be used later for expected SNR analysis of the filtered signal. Hence, the true total noise power at the input is much larger. Some computed values of the parameters covered in this section are summarised in Table 4.7.

Table 4.7: Values of some experiment system noise power parameters.

Parameter	Value	Description
η_A	0.6	Assumed antenna efficiency
T_{sky}	8 K	Clear sky temp.
T_a	275 K	Trop. H_2O & O_2 temp.
T_{leak}	20 K	Ground leakage temp.
$T_{sky,observed}$	59.7 K	Observed sky temp.
T_{Ground}	300 K	Ground temp.
T_{sys}	300 K	System temp.
T_d	156 K	Direct path noise temp.
T_r	300 K	Reflected path noise temp.
$N_{d,in}$	-131.5 dBW	Direct path input noise power
$N_{r,in}$	-128.6 dBW	Reflected path input noise power

4.2.8 Signal power calculations

Connecting the models covered in the previous sections, the receiver system direct and reflected path signal power levels can be summarised as

$$P_{d,in} = \frac{EIRP \cdot G_d}{L_{fs,GA} L_a L_{dp}}, \tag{4.46}$$

as well, as previously described by Equation 4.31, as

$$P_{r,in} = (4.31) = \frac{EIRP \cdot G_r \cdot \sigma_{RCS}}{L_{fs,SP} \cdot L_{fs,SPA} \cdot L_a}, \tag{4.47}$$

where $L_{fs,GA}$ is the free-space loss from the measurement setup to Astra 4A, L_a is the atmospheric absorption loss, G_d and G_r are the direct and reflected signal paths respective antenna gains, σ_{RCS} the radar cross section and the additional path loss of the reflected signal from the specular point to the receiver $L_{fs,SP}$. L_{dp} is an added de-pointing loss, which is a human factor (due to us not being too confident in our antenna aiming skills), and it is estimated as 1 dB.

Some computed values of the parameters covered in this section are summarised in Table 4.8. Worth noting is that the reflected signal path receiver input power $P_{r,in}$ is not increasing one-to-one with its antenna gain G_r, while that is the case for the direct signal path power $P_{d,in}$ as dependent on the antenna gain G_d. This is due to a higher gain implying a narrower antenna beam-width, which in turn decreases the resolution cell area in the cross-range direction and hence lowers the collected power, assuming fully diffuse scattering.

Table 4.8: Values of some experiment system signal power parameters.

Parameter	Value	SM	$G_{d/r}$	θ_A
$\mathbb{E}\{P_{d,in}\}$	-129 dBW	...	29 dBi	...
...	-123 dBW	...	35 dBi	...
...	-119 dBW	...	39 dBi	...
$\mathbb{E}\{P_{r,in}\}$	-178 dBW	0 %	19 dBi	16°
...	-176 dBW	0 %	23 dBi	9.9°
...	-172 dBW	0 %	29 dBi	5.8°

4.2.9 Digital coherent integration

The digital coherent integration is performed according to

$$s_c(n,l) = \frac{1}{K_i} \sum_{k=n-K_i}^{n} v_d(k-l) v_r^C(k), \tag{4.48}$$

where n is the current sample, l the delay in samples, K_i the number of samples integrated, v_d the sampled direct path channel and v_r the sampled reflected path channel. v_r and v_d can each be further modelled as a sum of their respective signal and noise components, s_r, s_d, n_r and n_d. The assumption is made that, within a coherence time, all four components can be modelled as Gaussian random variables,

where s_d and s_r are fully dependent at delay l (s_r is just a copy of s_d at delay l affected by a constant offset in phase and amplitude) while n_d and n_r are independent. Their powers are P_d, P_r, N_d and N_r respectively. The expression can then be expanded to include the signal and noise components, such that

$$v_d(k) = s_d(k) + n_d(k), \tag{4.49}$$

and

$$v_r(k) = s_r(k) + n_r(k). \tag{4.50}$$

It can then be stated that

$$(4.48) = \frac{1}{K_i} \sum_{k=n-K_i}^{n} (s_d(k-l) + n_d(k-l))(s_r(k) + n_r(k))^C, \tag{4.51}$$

$$(4.51) = \frac{1}{K_i} \sum_{k=n-K}^{n} (s_d(k-l)s_r^C(k) + s_r^C(k)n_d(k-l) + s_d(k-l)n_r^C(k) + n_d(k-l)n_r^C(k)). \tag{4.52}$$

By observing this expression, there can be stated to be four significant power components - one signal and three noise factors. The proper derivation is a bit tedious, but it can be summarised as

$$|(4.52)|^2 \propto G_i P_d P_r + P_r N_d + P_d N_r + N_d N_r, \tag{4.53}$$

where the coherent integration gain is

$$G_i = B \cdot T_i, \tag{4.54}$$

for a set coherent integration time T_i and signal bandwidth B. Mind that the signal bandwidth and the noise bandwidth might differ depending on filtering techniques. As a side note, the derivation of the integration gain expression results in this signal-bandwidth limit due to two reasons. First, a larger bandwidth increases the noise power, which reduces the SNR gain. Secondly, the noise will start adding up coherently if the sampling time is smaller than the coherence time of the noise (which is the inverse of its bandwidth) since the noise samples will start being correlated in time. Hence, oversampling the signal will not improve the gain. Also, the needed number of coherent samples stored, K_i, to perform the integration can be calculated as

$$K_i = Ti \cdot f_s, \tag{4.55}$$

in terms of the system sampling rate f_s. For a stationary measurement setup, this will limit the coherent integration gain if the sampler has a limited sample memory depth.

Connecting back to Equation 4.53, the signal power S_c consists of

$$S_c = G_i P_d P_r, \tag{4.56}$$

and the noise power N_c is the sum of the remaining terms

$$N_c = P_r N_d + P_d N_r + N_d N_r, \tag{4.57}$$

Worth noting is that two of the noise power terms scale with the signal power terms. This implies that the gain of increasing the signal power, by e.g. using a larger gain antenna, of only one of the direct or reflected signal paths is saturated at a certain point. With this in mind, the expected SNR, as the ratio of the coherent integration signal and noise powers S_c and N_c respectively, resulting from the coherent integration can thus be expressed in terms of the four powers at the input of the sampler as

$$\mathbb{E}\{\frac{S_c}{N_c}\} = \mathbb{E}\{\frac{G_i P_d P_r}{P_r N_d + P_d N_r + N_d N_r}\}, \tag{4.58}$$

Then, if it can be assumed that $P_d >> P_r$, $P_d >> N_r > N_d$ and also that the soil surface scattering is diffuse such that $\rho_r = \rho_d$, the expected SNR expression simplifies to

$$(4.58) \approx \frac{G_i\,\mathbb{E}\{P_r\}}{N_r} = \frac{G_i G_r EIRP A_{RC,0} R_{H,0}\,\mathbb{E}\{\rho_r^2\}}{N_r L_{fs,GA} L_a L_{fs,SP}} = \frac{G_i G_r EIRP A_{RC,0} R_{H,0} 2\sigma_R^2}{F_{Rx} N_{r,in} L_{fs,GA} L_a L_{fs,SP}}, \tag{4.59}$$

Similarly, since ρ_r^2 is the only significantly random factor affecting the signal power average during a coherent integration time interval, the signal power S_c can be viewed as an exponential random variable with a standard deviation expressed as

$$\sigma_{S_c} = \mathbb{E}\{S_c\} \approx G_i G_r EIRP A_{RC,0} R_{H,0} 2\sigma_R^2, \tag{4.60}$$

Some computed values of the parameters covered in this section are summarized in Table 4.9.

Table 4.9: Values of some experiment system coherent integration parameters.

Parameter	Value	SM	T_i	G_r
G_i	45.2 dB	...	1 ms	...
...	55.2 dB	...	10 ms	...
...	62.2 dB	...	50 ms	...
$\mathbb{E}\{\frac{S_c}{N_c}\}$	1.5 dB	0 %	1 ms	29 dBi
...	11.5 dB	0 %	10 ms	29 dBi
...	18.5 dB	0 %	50 ms	29 dBi

4.2.10 Digital non-coherent integration

A number M of coherent integration observations can be combined non-coherently for the purpose of suppressing the speckle noise and thus yield a more accurate mean signal power level estimate. The non-coherent integration can then be performed

by averaging the power of the coherent integration result $s_c(n, l)$, given in Equation 4.48, as

$$S(l) = \frac{1}{M} \sum_{i=1}^{M} |s_c(iN_c, l)|^2, \tag{4.61}$$

where N_c is at least the number of samples within a channel coherence time T_c (the samples affected by speckle noise should be uncorrelated), hence

$$N_c \geq T_c f_s. \tag{4.62}$$

For a static soil moisture measurement experiment setup, the coherence time might be very long. Independent speckle noise samples will then have to be forced by either moving the receiver slightly to the side or changing the resolved area by aiming the reflected signal path antenna differently. This would then need to be done for each non-coherent sample to be obtained.

As M increases, the resulting distribution approaches that of a Gaussian (as can be seen in Figure 4.10) with a standard deviation shrinking as the square-root of M. This is expected according to the law of large numbers. The resulting signal power PDF is seen to centre around its mean with the speckle noise standard deviation decreasing according to

$$\sigma_S = \frac{\sigma_{S_c} + \sigma_{Nr}}{\sqrt{M}}. \tag{4.63}$$

Hence, if it is sought for to improve the precision to e.g. 10 % compared to that of one signal power observation, an M of at least 100 is required. In turn, the mean signal power of the non-coherent integration result is

$$\mathbb{E}\{S\} \approx \mathbb{E}\{S_c\} + N_r = (4.60) + N_r. \tag{4.64}$$

But this is just looking at the effect of the scattering. To see how the dominant noise term N_r affects this result, some uncorrelated observations i of the coherent integration $s_c(i)$ can be modelled as

$$s_c(i) = \sqrt{\frac{\mathbb{E}\{S_c\}}{2\sigma_R^2}} \rho_r(i) + n_r(i), \tag{4.65}$$

where $n_r(i)$ are independent samples drawn from a zero-mean Gaussian distribution of power N_r and $\rho_r(i)$ that from an assumed diffuse scattering. The resulting PDF by running a Monte Carlo simulation of this signal model as an input for Equation 4.61 for some different M and SNR expectations is shown in Figure 4.11. It can be seen that the observed mean power level is offset by the noise power level.

4.2.11 Expected system performance

To conclude, the system is expected to observe an average SNR of about 18.5 dB at the coherent integration output. This value makes it look promising to perform soil moisture measurements using the Astra 4A opportunity signals. Motivated by

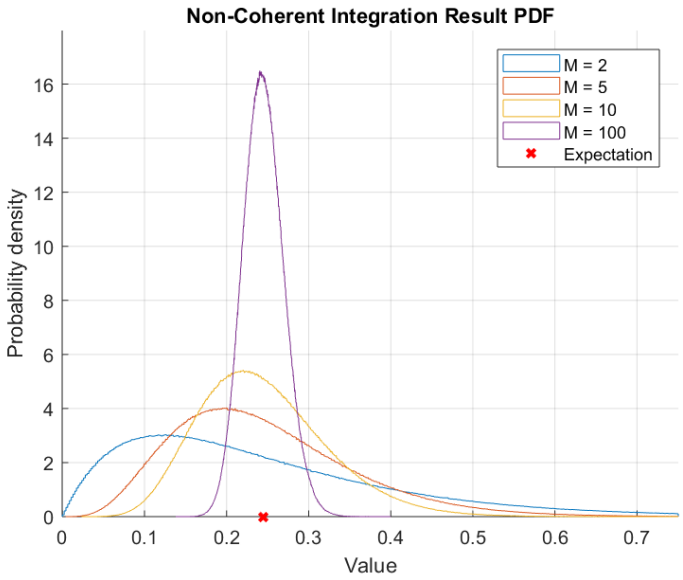

Figure 4.10: Signal power non-coherent integration result PDFs for some different numbers of M independent observations integrated. The PDFs were obtained with Monte Carlo simulations using 10^7 samples drawn from the distribution of ρ_d as shown in Figure 4.9. The expected mean signal power is marked with a red cross (setting all components in P_r to one except for the random term ρ_r).

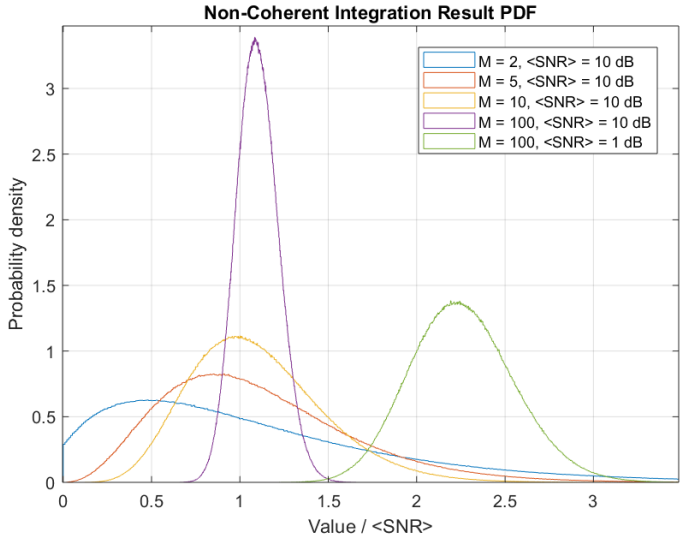

Figure 4.11: Signal power non-coherent integration result PDFs for some different numbers of M independent observations integrated and SNR values. The PDFs were obtained with Monte Carlo simulations using 10^7 samples drawn from the model described in Equation 4.65.

this, an attempt of implementing the passive reflectometry system and performing the experiment is considered worth a shot.

4.3 System Hardware Design

In order to process the SOOP from ASTRA 4A some hardware is required to sample it before the signal can be processed in the digital domain. The design-phase resulted in the hardware block diagram shown in Figure 4.13 and the specific hardware presented in Table 4.10. The hardware block is split into three main parts; *Up in the Tower*, *Down from the Tower* and *On the Ground*. Looking at the images shown in Figure 4.12 they intend to illustrate these different areas, where Figure 4.12a show the communication tower structure, Figure 4.12b show the hardware setup installed in the communication tower and Figure 4.12c show the laboratory on the ground.

Table 4.10: Showing the list of hardware used during all phases of the experiment.

Component block or description	**Name**	**Source**
HPF	NHP-1000+	Minicircuits
Mixer	ZX05-43-S+	Minicircuits
HPF	SLP-50+	Minicircuits
Mixer	ZFL-500+	Minicircuits
Power spliter	ZAPD-2-252-S+	Minicircuits
Power spliter	ZAPD-2-252-N+	Minicircuits
150 meter cable (Eco-flex 10)	101086	Mauritz Electronics
N-connector (female)	1230386	Mauritz Electronics
N-connector (male)	1220386	Mauritz Electronics

The objective of the hardware is to receive the two Ku band signal from ASTRA 4A at 11.881 GHz and 11.919 GHz and fold them on top of each other with during the down-mixing. A set of design rules where set up around the requirements of the system to help optimize the hardware design. First of all the antenna size is directly limited by the beam width and minimum SNR behind it, which sets an interval of acceptable antenna sizes. Next, in order to avoid the signals decorrelating due to phase drift the two low-noise block down converter (LNB) blocks will be synchronized and the mixers will use the same local oscillator (LO). Finally, the hardware is supposed to avoid deteriorate the SNR and Friis formulas for noise is used to analyse the system to archive this together with putting amplifiers before any notable losses in the system.

First section of the hardware block is the *Up in the Tower* section in Figure 4.13, it consists of three main parts; an antenna, an LNB and an Line amplifier. The antenna had three main requirements; a wave guide connector (WR-75) due to the LNB and limitations to the size due to minimum SNR and minimum area the beam illuminates. The requirements regarding the SNR both limit the size on the antenna setting a lower (minimum SNR) and upper (minimum beam size) diameter allowed, this was described in more detail in Section 4.2. Getting the type of antennas required was solved with the help of our sponsor Leax Arkivator Telecom

(a) An image of the third antenna tower at Grimeton Radio Station, the one used for the experiment. The tower is 127 meter high and is part of a long wave tranmitter antenna.

(b) An image from the top of the third tower at Grimeton Radio Station, where the hardware setup from the experiment can be seen. Credit to Julian and Oskar for the image, whom helped us with installing the antennas through days of microwave ghosts and random issues.

(c) An image of the horse trailer also known as the lab, which served as a base for the ground-software and equipment. Big thanks to our supervisor Jacob Christensen for letting us borrow it.

Figure 4.12: Images from Grimeton Radio Station during the experiment expedition.

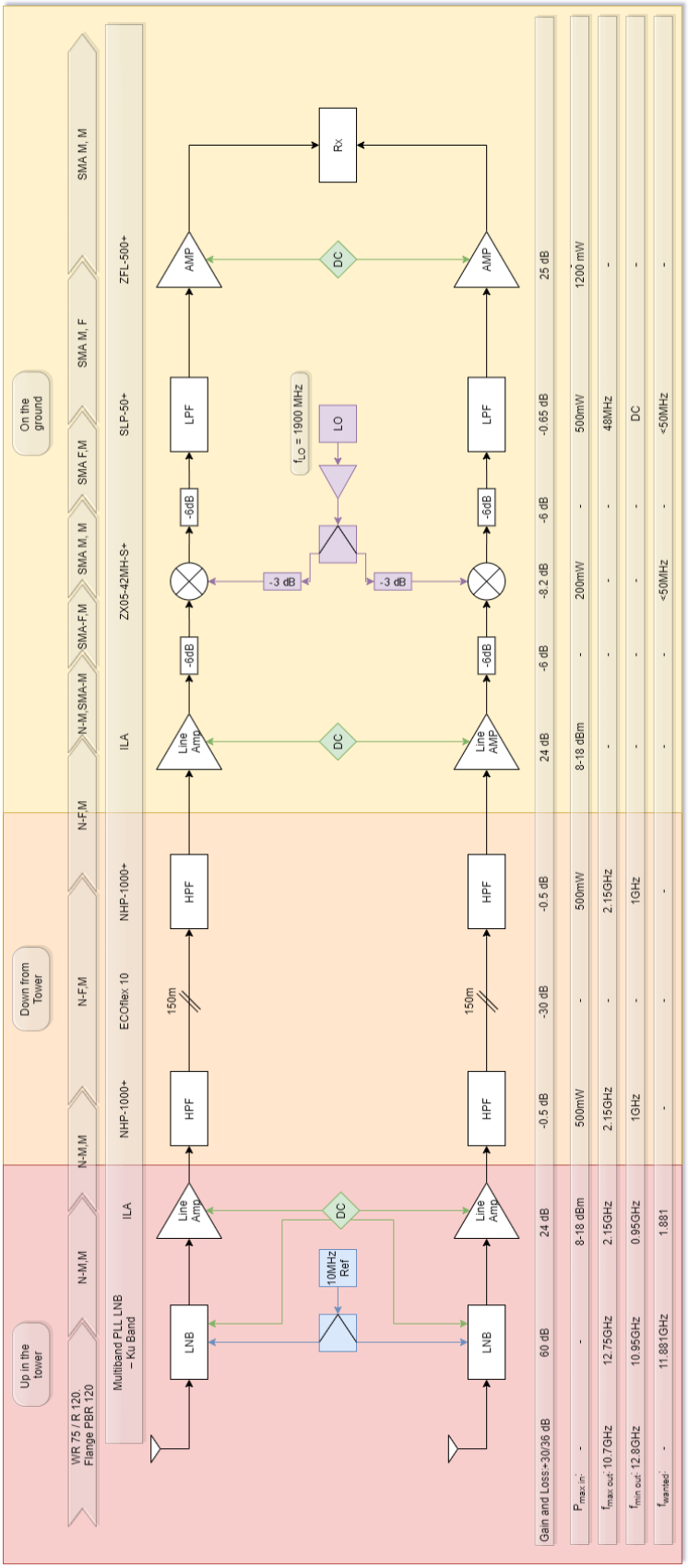

Figure 4.13: Block diagram of the hardware design, separated by the background colour in three areas: *Up in the tower*, *Down from the tower* and *On the ground*.

AB who sponsored us with two dish antennas. The next hardware part was the LNB that was used to amplify the Ku-band signal and mix it down to L-band, besides this it also had an external clock reference to phase synchronise the two signal chains to avoid decorrelating them. A Ku-band LNB with an external reference clock is not an conventional component but was supplied to us by Swedish Microwave AB (SMW). Besides the LNB SMW also provided us with line amplifiers, these was used to amplify the signal before to the 150 meter cable to avoid deteriorating the signal.

Next considering the *Down from the Tower* section of the block in Figure 4.13, it consists of mainly two parts; a 150 meter cable and two high-pass filter (HPF). First of all, the cable is a 50 Ω transmission line down from the tower and it was chosen to minimize cable loss and have a large isolation due to potential electromagnetic compatibility (EMC) issues at Grimeton Radio Station. Next, the HPF was another precation to avoid EMC issues due to large electic or magnetc fields from the Grimeton Radio Station. This was considered to be a possible issue as Grimeton Radio Station is an active radio station that continuously transmits at high power levels but at low frequencies.

Finally considering the *On the Ground* section of the block in Figure 4.13, it consists of five main parts; a line amplifier, a mixer, a low-pass filter (LPF), a low-noise amplifier (LNA) and a sampling source. Starting with the line amplifier, it is placed there to amplify the signal before losses due to the mixer. Next, a mixer was used to move the signal from L-band to base-band (BB). By recommendation we placed an attenuateor at each connection around the mixer to avoid issues due reflections mixing over and over causing issues. The LPF block attenuates the unwanted signal above 50 MHz to avoid aliasing it in to the desired signal when sampling it. This is important as a lower sampling rate is desired due to large datasets but it also lowers the Nyquist frequency causing lower frequencies to be aliased. Following the LPF is the LNA that amplifies the signal one last time to optimize it according to the dynamic range of the sampling source. This was important since the oscilloscope used for sampling is not designed for the low energy levels of a communication system. The last block is the Rx which is the sampling source used, in this project a oscilloscope (Teledyne Lecrow Waverunner 606 Zi) was used. Regarding the sampling source there were several important notes but the main ones was; memory depth, connectivity and sampling rate. Memory depth governs how many samples you can save, at high sample rates this can be a large limit to the coherent integration time. Connectivity was important as the goal was to make the system automated, which requires a stable connection and possible steering from the computer. Lastly, the sampling rate governs how long we can sample, where our anti-aliasing filters should be and how broad band we can collect.

4.4 System Software Design

Some crucial parts of the system is implemented in software, both for computational and control needs. This section describes the digital signal processing (DSP) system design and implementation specifics. It also covers that of a system control and automation application.

4.4.1 Digital signal processing implementation

Block diagrams of the DSP system design principle is shown in Figures 4.14 and 4.15 and it is implemented in MATLAB on a PC provided by RUAG Space. The oscilloscopes functions is controlled from the MATLAB script through combining its remote instrument driver with the MATLAB Instrument Control Toolbox. Setup and streaming of up to a chunk of $32 \cdot 10^6$ consecutive and simultaneous samples (the oscilloscope sample memory depth) per channel over an ethernet cable to the PC is thereby done, when commanded from the script.

Worth noting, before diving into the specific operations, is that MATLAB represents each sample of these two as most 32 MS chunks as a floating point number (and not an 8 bit integer, which is what it really is). It is crucial to heed the complexity this implies on different mathematical operations. Just by converting the two signals data to a complex format is making them into a gigabyte sized array. Even though the PC has 48 GB of RAM and a number of formidable processor cores, performing the delay correlation processing as a convolution matrix operation is way too heavy for it to handle. The processing time for a measurement was managed to be reduced to minute-time-scale by replacing convolutions (squared complexity) with frequency domain FFT multiplications (logarithmic complexity) and so on. Also, the MATLAB Parallel Computing Toolbox proved very useful since it allowed for parting the very demanding coherent integration block computation in between the processor cores, significantly speeding up the process as they could simultaneously run through different delay or frequency correlation taps. A C or FPGA implementation would be able to perform the computations incredibly more efficiently, even in real-time, but MATLAB is a convenient tool in this case for its simplicity of implementation and agility in analysis of the results. Also, a more dedicated such implementation is beyond the resources of this thesis.

Describing the implementation seen in the figures, the principle is the following. Starting at the sampler block, which represents the use of the oscilloscope, the reflected and direct path signals are simultaneously sampled on two of the oscilloscopes channels at a sample rate of 100 MS/s into two 32 MS data chunks. Each of the two signals are then digitally mixed down to complex baseband, with the NCO frequency set to the signal IF frequency at 19.2 MHz. Then the both signal chains are low-pass filtered around the two-sided signal bandwidth of 33 MHz, where after the direct path signal is split into different delay and frequency taps while the reflected path signal is complex conjugated (to cancel out the phase of the signal, i.e. extract that of the effects on the signal, in the later coherent correlation result).

The two signal paths are then fed to the coherent integration block, as shown in Figure 4.15, which just multiplies each sample at each time of the delay and frequency taps of the direct path signal with the reflected path signal. The number of store sample blocks, z^{-1}, are set by the number of samples acquired within a coherent integration time interval. The output of this block is a DDM (delay-doppler map), but using just either delay or frequency taps makes it easier to present as a time-delay or time-doppler map, showing the signals correlation at a given delay or frequency offset over the sampled signal chunk time length (32 MS data implies a 320 ms time interval at the sampling rate of 100 MS/s). Although, in practice the operation is performed by translating the process into FFT operations due to

the complexity of the multiplication-and-sum operation (which can be viewed as a convolution).

Anyhow, the resulting DDM is then down-sampled in time by a factor of about 10^5, since the result is expected to be coherent and thus approximately constant during many millions of samples - all of those are not interesting to observe. The resulting DDM of a signals sample data chunk is then saved to an external terabyte hard drive and the file is tagged with the time of the measurement. The following power transform simply extracts the power (squared amplitude) of each of the complex elements in the coherent DDM. The middle sample of the DDM is then used as input to the non-coherent integration block, which is just averaging a number of DDM results if wanted to do so. This sequence of coherent DDM middle-samples, separated by a measurement time interval, are also collected in a non-coherent larger time-scale DDM for the purpose of analysing measurement time series.

4.4.2 Measurement control and automation app

For organisational and efficiency purposes, as well as just the fun of it, a PC application was constructed to both control and automate the DSP system, which is described in the previous subsection, to obtain coherent and non-coherent integration time-delay map results. The application interface can be seen running in-action in Figure 4.16, at a verification test described in later sections. To the left is the settings section. In the middle is the coherent integration time-delay map result shown (a large correlation peak at zero delay over a time span of 50 ms is seen in this case), some command buttons and lamps (e.g. run, stop, reset) with a software output command window. To the right is a non-coherent time-delay map, showing a larger time scale (minutes between samples) and beneath it the direct and reflected path raw sampled signals are presented. Looking under the interface hood of the application, a couple of timer callback functions are handling the measurement automation as well as the storage and labelling of raw and result data. They are also initializing and keeping up e.g. oscilloscope and PC communications and the parallel computing environment.

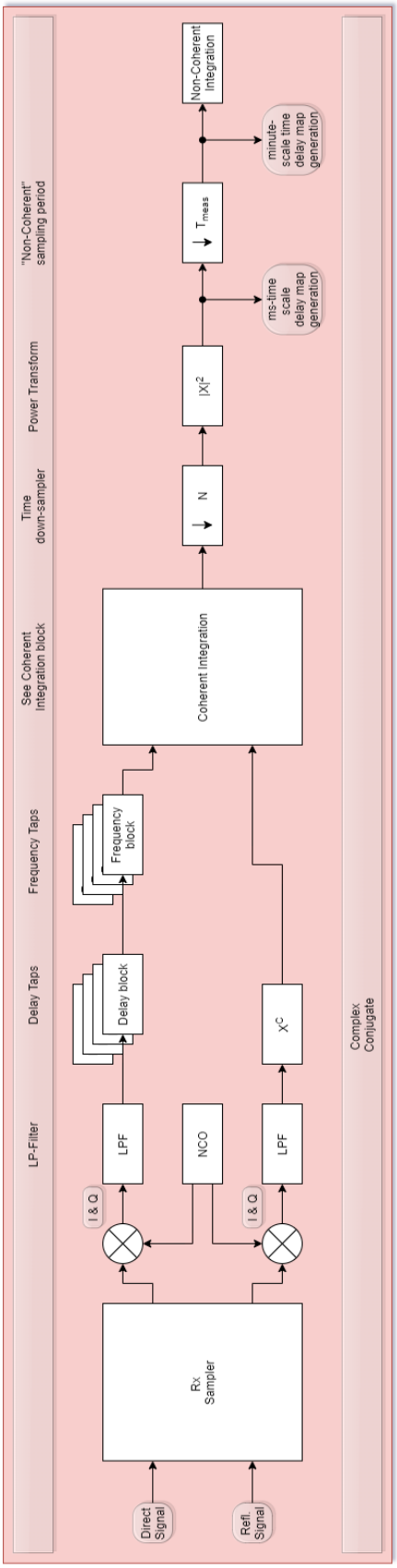

Figure 4.14: Block diagram of the DSP system design.

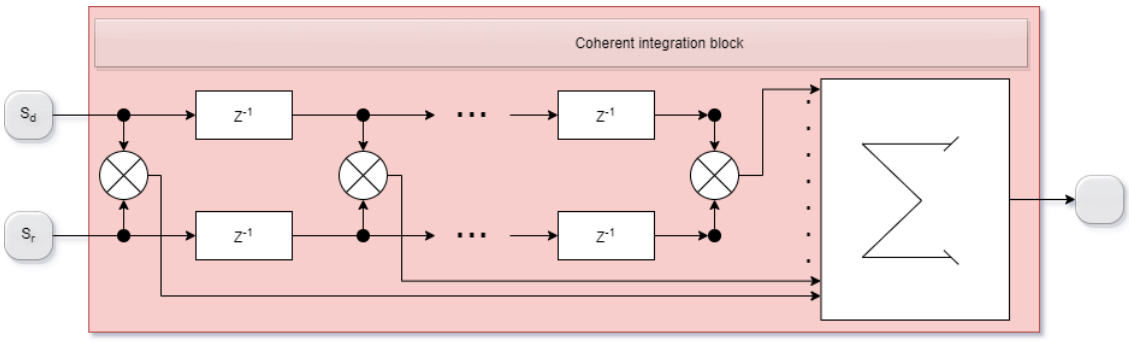

Figure 4.15: Block diagram of the coherent integrator block from the DSP system described by the block diagram in Figure 4.14.

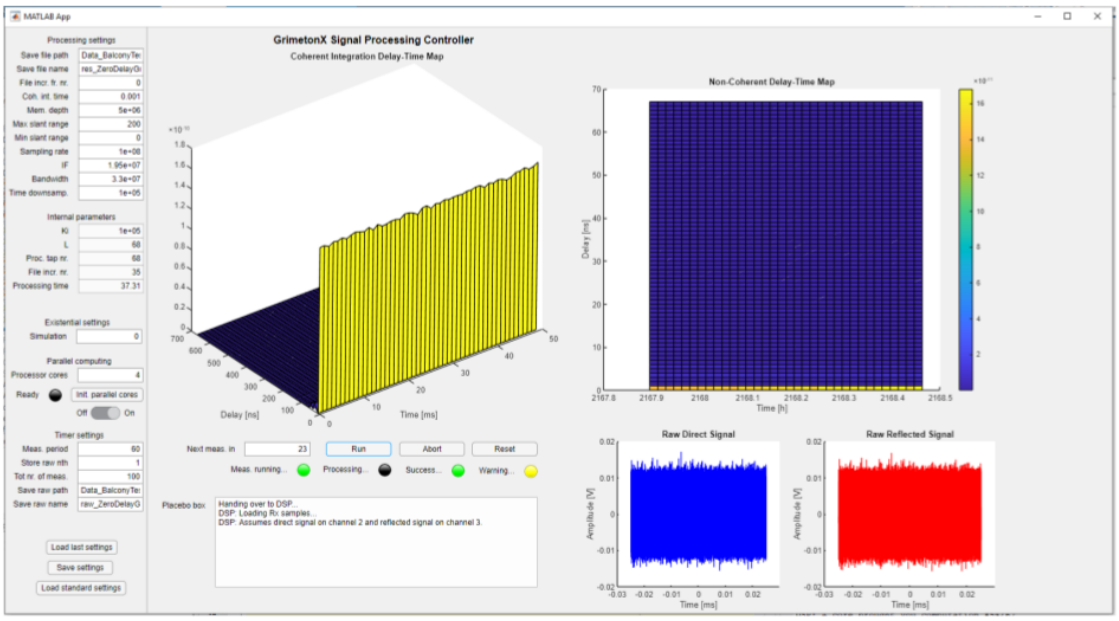

Figure 4.16: The measurement control and automation application interface in action. More specifically, this screenshot is taken during the Balcony expedition zero-delay test described in Section 4.5.4. As a disclaimer, the app was constructed solely for the purpose of efficient verification and automation of measurements - not as a user friendly interface.

4.5 System Verification

Before putting the system to the test at any experiment, it is of importance to verify the system to be properly functioning. There are many reasons to perform thorough system verification. It is advantageous to identify errors and problems early in the system implementation process, to make sure that each part of the system works as intended. If not, it is of relevance to identify to what extent that affects the system end product. Just so, it is wanted to indicate the performance of the final system, then providing reason to carry on further with the experiment. This is also important for motivating further investments in performing the experiment from RUAG Space as well as sponsor contacts.

The system verification process is carried out in four main parts. First, laboratory hardware tests are performed to verify the expected function of components and the RF front-end as a whole. Meanwhile, in parallel to the first test, the function of the DSP software is evaluated by stimulating the system with simulated expected input signals. When both these tests are accomplished, the hardware-software signal chain interaction is verified by inputting a single tone to the RF front-end and observing the processed result. Lastly, to evaluate the final system in a real situation, an expedition is done to a balcony where the system is installed and tested with both antennas collecting the actual Astra 4A signal.

4.5.1 Laboratory hardware verification tests

Verifying the hardware in a lab environment was done using a sweep-generator to generate signals over a span corresponding to the intended input to any given block. The frequency ranges was set according to a slightly wider window than the expected input to each block, as to ensure that the block worked properly for all input frequencies. Another important verification test was made to verify the system for different power levels. These tests was made in three steps; very low power, expected power and higher than expected power. These power tests was to ensure that the system could handle a range of voltages without failing.

Considering Figure 4.17 they show the first four hardware verification setups performed in the laboratory. The first figure illustrates the idea behind the testing, starting the testing with one component and then adding one component per test to always have verified the previous components. In order, this block shows the verification tests for LNA, LPF, mixer and line amplifier where each part was tested for three power levels and a frequency band slightly wider than the intended input.

Considering Figures 4.18 and 4.19 they show the fifth and sixth hardware verification setups performed in the laboratory. First, Figure 4.18 show the verification test for the LNB, note that some amplifiers have been removed since the previous line amplifier test. This was performed using a *WR-75 to SMA* adapter to connect the sweep-generator to the LNB. The reason for removing the amplifiers is due to the minimum power of the sweep-generator being too high (-80 dBm) in comparison to the intended input. Finally Figure 4.19 show the verification test for the 150 meter cable. An important reason for this test is that the cable was home-made and there was a risk of errors due to inexperience.

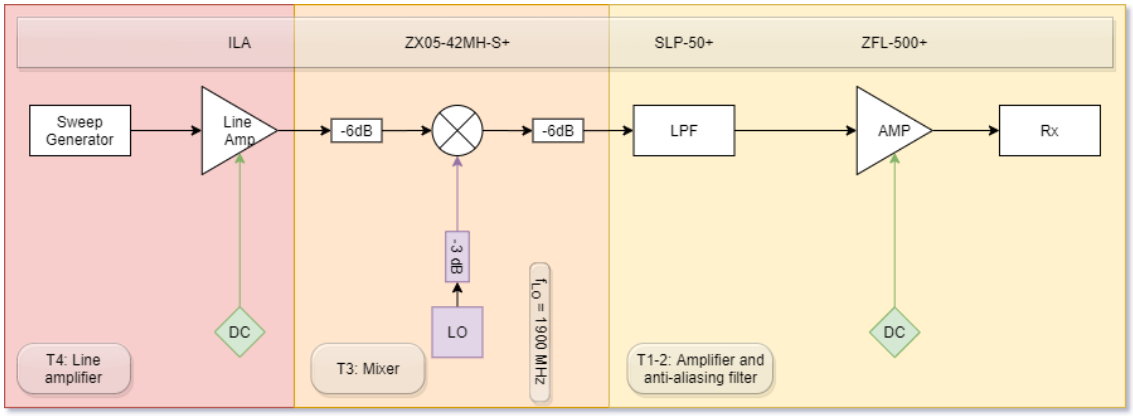

Figure 4.17: Block diagram of the first three hardware verification tests for the amplifier and anti-analysing filter, the mixer and the line amplfier.

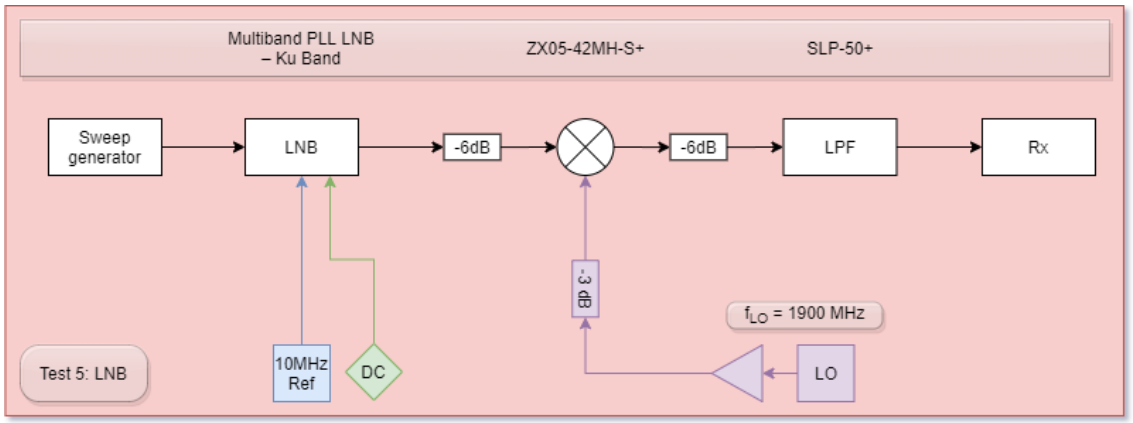

Figure 4.18: Block diagram of the hardware verification test for the LNB.

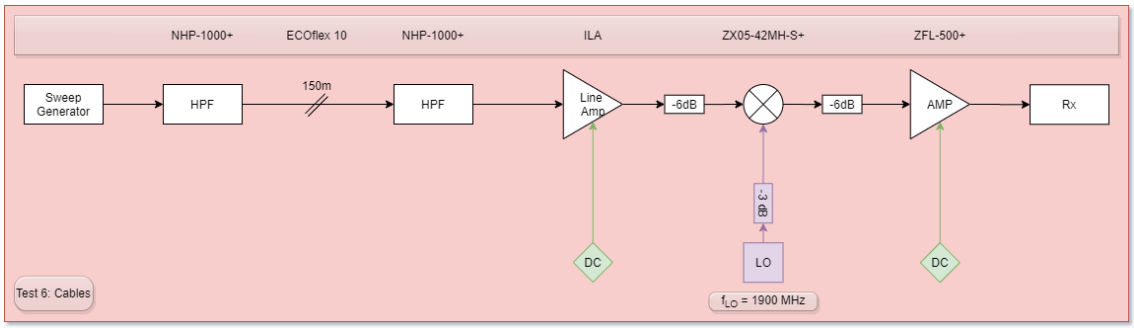

Figure 4.19: Block diagram of the hardware verification test for the 150 m cable.

4.5.2 Software input signal simulation test

To make sure that the DSP and application software worked as intended, an approximation of the expected sampled input signal was simulated. This was done by generating three sequences of Gaussian noise, each corresponding to the signal, the direct path noise and the reflected path noise respectively, and filtering them around a bandwidth equal to that of the Astra 4A signal (i.e. 33 MHz). The direct sampled signal is then compiled, simply enough, by scaling the Gaussian signal sequence approximation with the modelled received direct path signal power and adding it with the generated direct path noise sequence (also scaled according to its modelled power level). The reflected path signal was compiled similarly, but with the difference that the Gaussian signal sequence approximation is delayed in samples corresponding to about 300 ns, which is about what is expected at Grimeton according to the models when observing the specular point.

The result of running the processing on this simple input signal simulation is shown in Figure 4.20. 300 ms of signal was simulated (it is shorter in the figure since filter edge-effects are cut away) and a coherent integration time of 50 ms was used, providing a theoretical expected SNR of about 18.5 dB. It is seen in Figure 4.20b that the peak energy is about 18 dB above that of the noise floor, corresponding well to the expected result. A slightly more complex signal simulation case was also implemented, taking into account the effect of several present delay resolution cells, but the results are then of a more statistical nature and thus not as controllable. In short, the simple simulation can be said to resemble the effect of a specular reflection but at a resulting SNR corresponding to that expected from purely diffuse scattering. Hence, the simple simulation result as shown in the figure is considered more suitable for verification purposes as well as providing a foundation for expected system performance at Grimeton.

4.5.3 Laboratory single-tone test

The function of the system signal chain, excluding the LNBs and antennas, was verified in a laboratory environment by splitting a generated single tone into both the inputs of the system. The processed result TDM of such a test should be very constant in time and show periodic energy peaks in delay, following (if viewed in delay "time") the energy of a cosine (since zero delay should give a maxima) with a frequency the same as that at the sampler (oscilloscope) inputs. The resulting TDM of such a test is shown in Figure 4.21 and the previously described behaviour is clearly seen. This particular test used an input CW tone to the two system inputs of 1.881 GHz, which thereby was mixed down to 10 MHz at the sampler. This result indicates that the oscilloscope is properly sampling the both channels simultaneously as well as the signal making it through the RF front-end as intended, not being obviously distorted.

4.5.4 Balcony expedition zero-delay test

To verify the final full system function (now including the LNBs and antennas) and as a preparatory exercise for the Grimeton experiment, an expedition was carried out

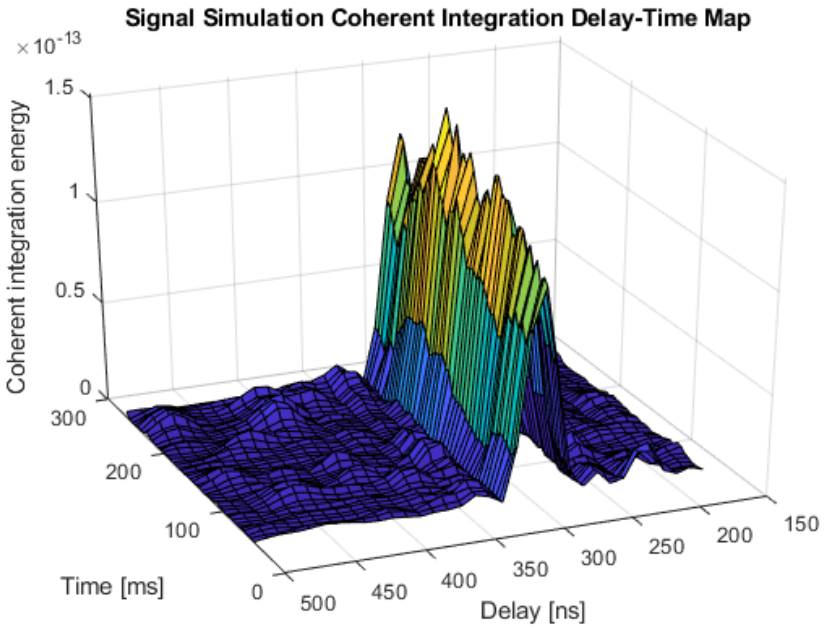

(a)

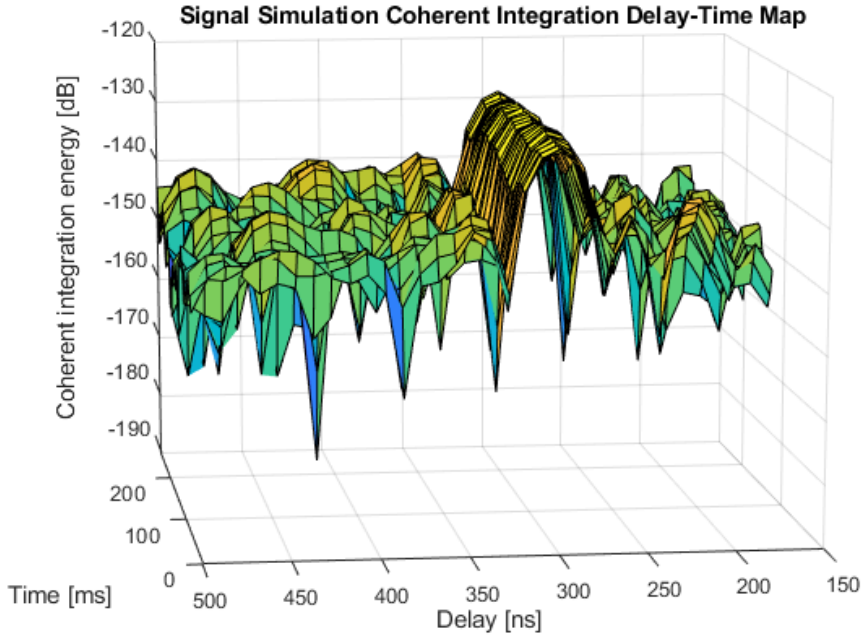

(b)

Figure 4.20: The delay-time map result of a DSP input signal simulation test, in (a) and (b) shown in linear and dB scale respectively. A coherent integration time of 50 ms was used to obtain this result. The signals and noise is simulated according to expected delay and (relative) power levels derived from the Grimeton experiment setup modelling. Note that the energy value is relative and not calibrated, hence it is not being presented in dBm.

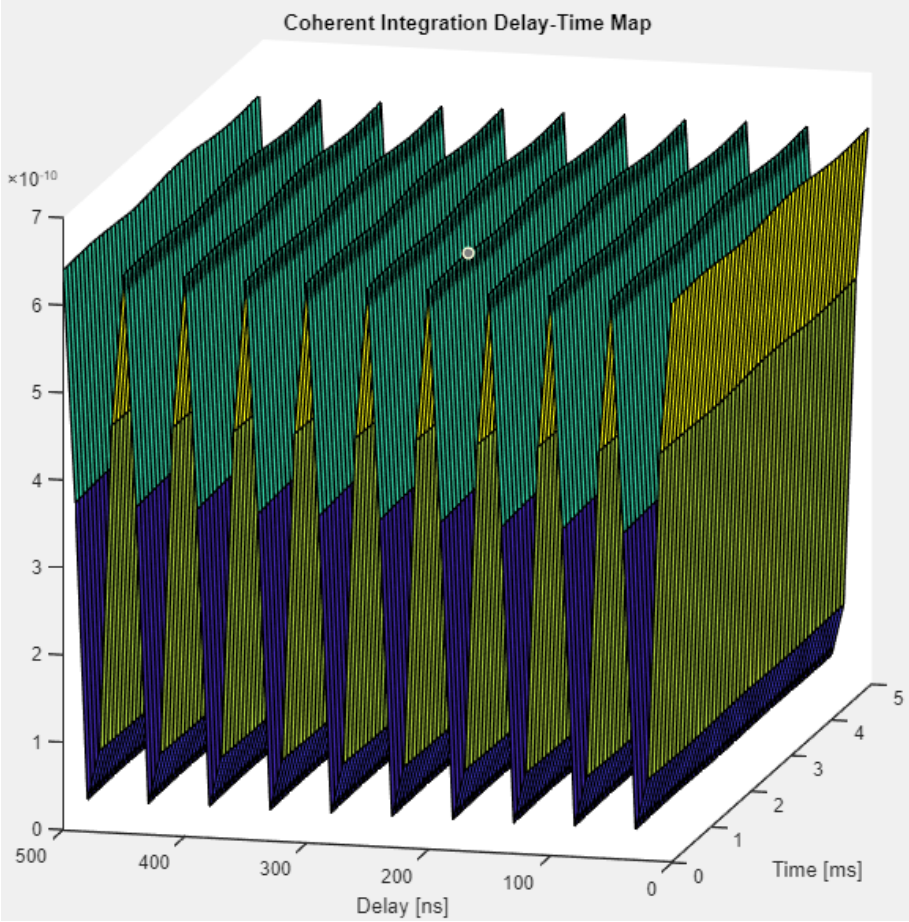

Figure 4.21: The laboratory single-tone test resulting coherent integration time-delay map. A CW input of the frequency 10 MHz at the sampler and a coherent integration time of 1 ms was used to obtain this result. Note that the figure is showing the energy of the correlation result, hence there being two peaks present per 100 ns delay (i.e. a 10 MHz period time).

Figure 4.22: The balcony expedition zero-delay verification test antenna setup. Both antennas are aimed directly at the GEO TV-DBS Astra 4A. Special thanks to Vanessa and Per for letting us borrow their apartment and especially spacious balcony for experiments during the day of their wedding.

to a balcony where the system was installed and a zero-delay test was performed. The principle of the zero-delay test was such that the both antennas are aimed directly at the source Astra 4A, which should result in a very strong correlation peak at the zero delay line (since the both signal paths are of the same length) in the processed result TDM. Also, the peak should be very constant in time and die off in delay, until there was only noise floor. Although, there might be some small peaks due to reflections on nearby buildings or other environment. The hardware installation block diagram is illustrated in Figure 4.23 and the antenna setup at the balcony is presented in Figure 4.22.

The resulting TDM of this zero-delay test is shown in Figure 4.24. The processing was done using 10 ms of sampled signals and a coherent integration time of 1 ms. Worth to observe is that there is indeed an obvious peak prominent at the zero delay line. The peak is also very constant in energy, but there can be noted a small perturbation at the top as seen in figure (a). Also, as can be observed in the dB-scale figure (b), the strong peak is leaking energy in correlation side-lobes up to about 200 ns delay until it descends down beneath the noise floor. There are most probably some reflections from the nearby environment as well, causing e.g. the small energy bump at about 150 ns delay. It is concluded from this verification test that the system seem to work well enough to carry on with the Grimeton experiment.

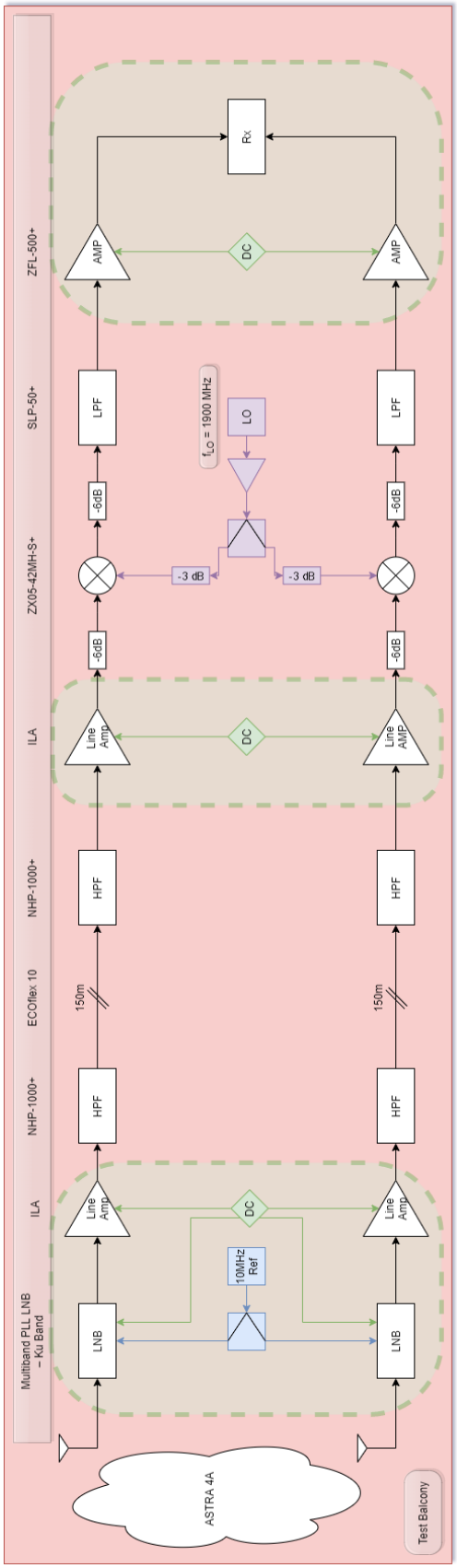

Figure 4.23: Block diagram of the hardware system used at the balcony expedition zero-delay verification test.

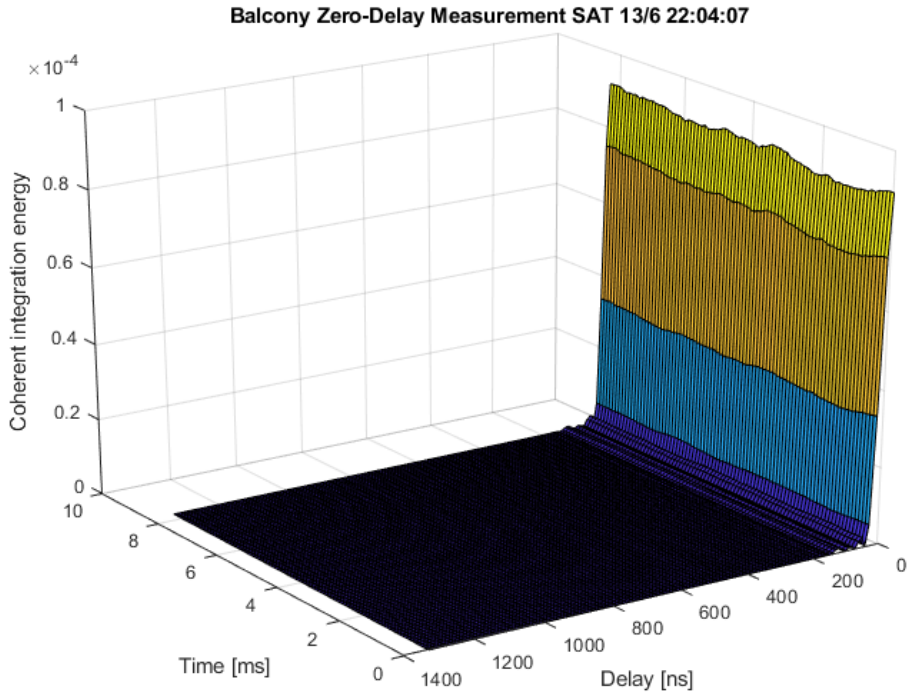

(a)

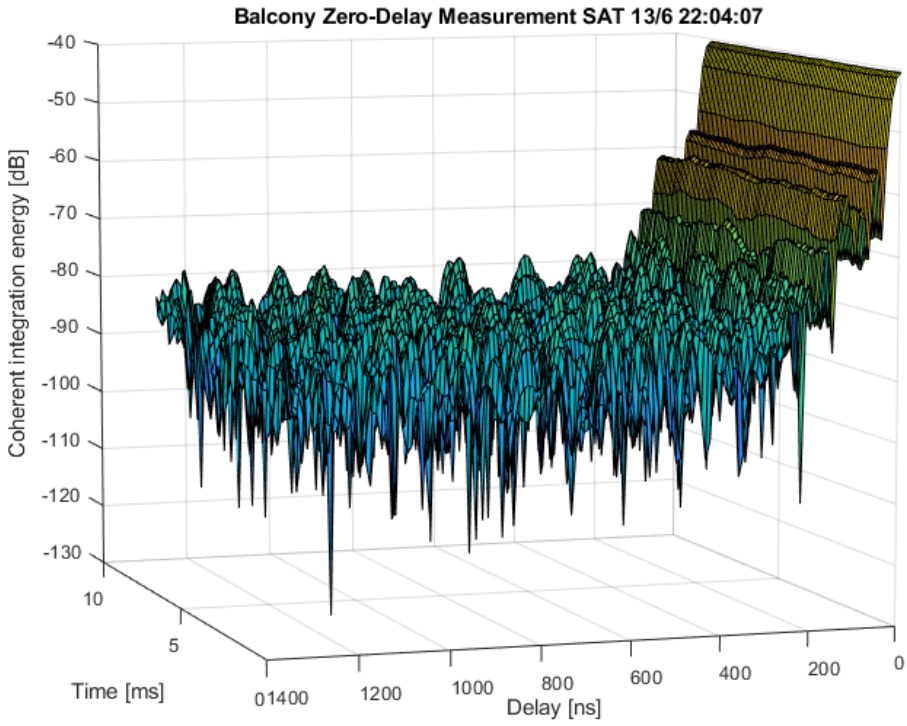

(b)

Figure 4.24: The delay-time map result of the Balcony zero-delay test using both antennas, in a) and b) shown in linear and dB scale respectively. A coherent integration time of 1 ms was used to obtain this result. Note that the energy value is relative and not calibrated, hence it is not being presented in dBm.

4.6 Grimeton Expedition Results

The experiment expedition at World Heritage Grimeton Radio Station was performed during four days, from Monday 15:th of June to Thursday 18:th of June. To evaluate the prospects of agriculture soil moisture measurements by observing signals from the Ku-band TV-DBS Astra 4A, two main investigations were performed throughout the experiment. The first aimed at investigating the scattering environment of the signal. This includes determining if any signal is detected at some different points of interest - and if that is the case, how e.g. the signal strength and coherence time varied with the angle to the point of interest in question (i.e. how diffuse or specular the scattering is). The second investigation aimed at detecting any relative soil moisture changes over time at a point of interest. This was done by acquiring a time series of measurements at the specular point, preferably extending over at least two days and nights since the main change was expected at dawn. This was due to neither rain nor too windy weather unfortunately being a requirement for the very brief installation of the measurement setup. But before the main investigations were performed, the function of the system was verified and analysed by an initial zero-delay test, similarly as was done at the balcony expedition.

Although problems were expected to introduce themselves, the fist two days and nights was unfortunately spent chasing microwave ghosts until the system was properly running. The lost time forced us to prioritise just a few especially important and time-efficient sets of measurements to perform. Then, also a power outage occurred during the last night and interrupted the time series measurements. Further details about these and other encountered problems are covered in the later discussions section. Still, results were acquired as presented in the following subsections.

4.6.1 Initial zero-delay test

The zero-delay test was performed mainly to verify a correct system installation, but also to observe some present noise and correlation properties. An acquired zero-delay test delay-time map is shown in Figure 4.25. As seen in the figure, there is a clear coherent correlation peak at zero delay as expected. When comparing the peak energy level relative to that of the noise floor (correlation far in delay), which can be estimated to about -105 dB from the dB-scaled map in Figure 4.25b, the SNR is about 60 dB. Given the coherent integration time of 50 ms, this corresponds well to theoretical calculations which suggests an instant SNR of about 0 dB to be expected with an additional 62 dB gain from the coherent integration. The noise floor also looks to be at a very similar level as that of the balcony expedition zero-delay test results of Figure 4.24, given that an increase of the integration time of a factor 50 from 1 ms to 50 ms would theoretically lower the noise floor an additional 17 dB.

Also, it is seen in Figure 4.25b that a separation of at least about 250 ns delay is required to suppress the power of the zero-delay line sidelobes below that of the noise floor. This required delay is presumably lower when not aiming both antennas directly at the signal source, due to the antenna directivity. Although, even then, direct path leakage is expected at about the same order of magnitude as that of the theoretical average reflected path signal correlation.

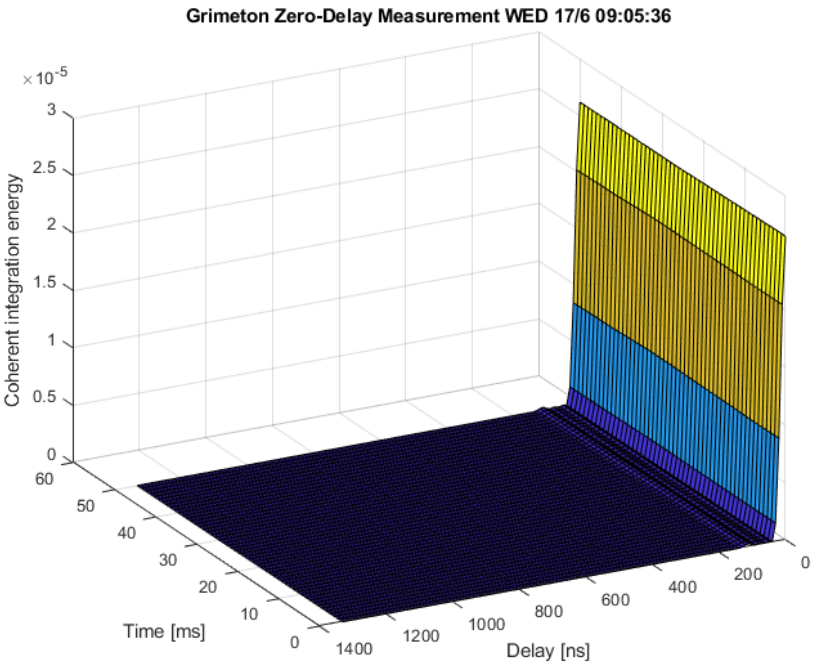

(a)

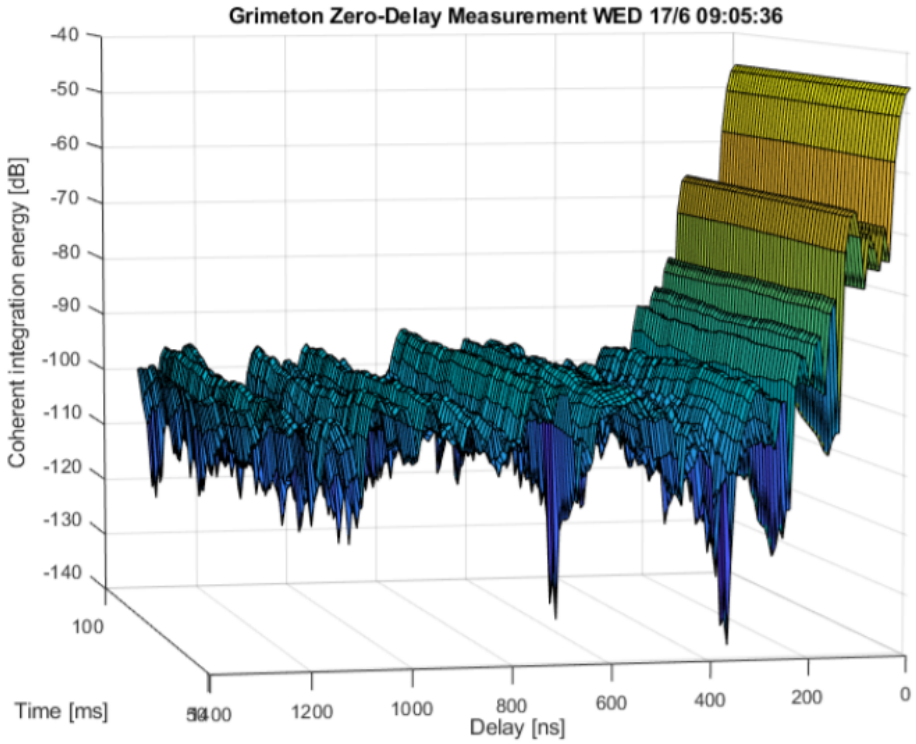

(b)

Figure 4.25: The delay-time map result of the Grimeton zero-delay test, in a) and b) shown in linear and dB scale respectively. A coherent integration time of 50 ms was used to obtain this result. Note that the energy value is relative and not calibrated, hence it is not being presented in dBm.

4.6.2 Scattering environment measurements

To determine whether a reflected signal can be detected or not using the PARIS implementation setup and if so, then, how well it is suited for soil moisture measurements, four measurement investigation points were defined. They were named by short, where "P" stands for "point", as P1, P2, P3 and P4 and their locations were chosen as shown in Figure 4.26. The points locations are chosen such as to indicate to what extent the signal was affected by specular or diffuse scattering. Then, when observing a detected signal, properties such as the SNR, coherence time and present delay-lines were interesting to determine.

Of course many more points are preferable to obtain, in total covering as large of an area as possible, allowing for extensive non-coherent integration and analysis of the measurement statistics. Also then, observing areas to both the east and west, or even trying to detect a signal via back-scatter from the north direction. Although, the setup was limited to $\pm 15^\circ$ movement of each antenna in the horizontal plane and it needed to be manually adjusted by the hired high-altitude work personnel. The time available for measurements requiring the personnel was therefore limited to a couple of hours during an afternoon (since this was done during the third day of the expedition and the morning was spent on installation and the zero-delay test), hence just the four simple investigation points being prioritised.

The first point, P1, is the specular reflection point, which is seen as a good starting point to measure at since a strong signal is expected from the region if the scattering has a distinct specular component. Then also, even if the scattering is strongly diffuse, a signal is expected. The point was located 9.1° south-west and 24.7° down from the receiver antennas at the radio station tower platform, at a ground range of about 260 m. An acquired time-delay map of a P1 measurement is shown in Figure 4.28. A few things can be noted from the figure. First and foremost, a strong correlation is indeed seen at the 330 ns delay line and some less prominent energy is also detected at what corresponds to the second or even third delay line. This corresponds exactly to the theoretically expected delay and resolved area. Also, there is direct path leakage at the zero delay line of about an equal power as that of the reflected path correlation. Additionally, the coherence time is larger than 200 ms. From a couple of such measurements, collected in a short time series seen in Figure 4.28a, the SNR is seen to vary about in between 15 to 24 dB. It can from there also be indicated that the signal seemed to be quite coherent for about 2 to 5 minutes, but the SNR is then clearly prone to change.

The second point, P2, was located straight to the south of the receiver. It is hence also referred to as the 0° south point. It was obtained by turning the reflected path antenna 9.1° to the east direction along the horizontal plane compared to that of point P1. Thus the ground range was still about 260 m (it is located on the radius of the specular point), which should ensure a similar path loss as for P1. An acquired time-delay map of a P2 measurement is shown in Figure 4.29. Especially interesting in this figure are the two clearly resolved correlation peaks present in between 330 ns and 430 ns delay. Both their magnitudes are about the same as that of the specular point, P1, correlation seen in Figure 4.28. Although a short time series, which is shown in Figure 4.28b, indicates the SNR to be varying in between about 12 to 23 dB with a coherence time of about 2 to 5 minutes.

Figure 4.26: A Google Maps overview of the third Grimeton Radio Station tower, which is encircled in red, where the reflectometry experiment was performed. The measurement points P1, P2, P3 and P4 are marked by the yellow circles, but note that the marked areas are just approximately covering the central resolution cell area at each point [34].

The third point, P3, was obtained by turning the reflected path antenna even 15° further to the east of P2 (since the antenna could not turn any further without rebuilding the installation), hence it also being referred to as the 15° south-east point. It was still, just as P2, located on the same radial ground distance from the receiver as the specular point, thus the ground range to the point being about 260 m. An acquired time-delay map of a P3 measurement is shown in Figure 4.30. As can be seen, there are two clearly resolved high correlation delay lines present in between about 350 ns and 450 ns delay. The delay was expected to increase as compared to that of P1 as the path to the point from Astra 4A is longer to P3 than to P1. Their magnitude is still about the same as that of the correlation of the reflected signal detected in both P1 and P2. A short time series at this point, as can be seen in Figure 4.28c, suggests the SNR to vary in between about 10 to 24 dB with a coherence time of about 2 to 5 minutes.

The fourth and final point, P4, was obtained by aiming the reflected path antenna in the specular point direction (9.1° west of the southern line) and then down 47°. It is hence referred to the 47° down point as well. The thought was to see how the vertical plane angle difference affects the measurement result. The ground range distance to this point was about 112 m. An acquired delay-time map of a P4

measurement is shown in Figure 4.31. Compared to the other points, a rather large correlation peak is as seen. The signal correlation is expected to be stronger (about 5 dB) due to the decreased path loss from the reflected area to the receiver. About two delay lines seem to be resolved and detected. A short time series, shown in Figure 4.28d, suggests this particular measurement to be some kind of extreme superposition of the signal. For this point, it is hard to determine any direct indications on the coherence time from this set of measurements.

In general, to summarise, the signal scattering environment is seen from the measurements to indicate some important main results. First and foremost, a clear signal was actually observed at all investigated measurement points. At the specular point, P1, one main correlation peak was seen, while at the diffuse points P2 and P3 two delay lines were resolved with about the same order of signal power each. This indicates the scattering to be partly specular with a largely diffuse component, i.e. that measurements are possible to do even when not observing areas in the purely specular direction. Although, more measurements would be required to verify this for scattering to the of the sides of a point or even back to the (in this case) southern direction. Another result is the fact that the observed SNR of the measurements is in the ballpark of what was concluded theoretically in the experiment pilot study (distributed around 12 to 24 dB). Also, the delay of all observed measurements corresponds very well to that expected from the models. This implies the modelling to not be too inaccurate. Lastly, the signal seemed to be coherent for at least 200 ms (in this stationary setup), with the short time series indicating the correlation signal power to change on the order of 2 to 5 minutes.

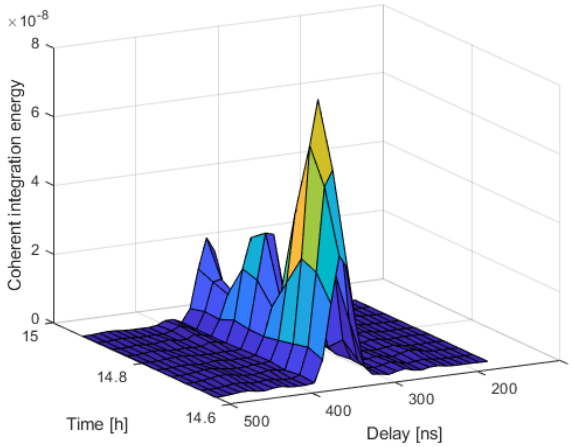

(a) Specular point, P1, result for 10 measurements using a 2 min measurement period.

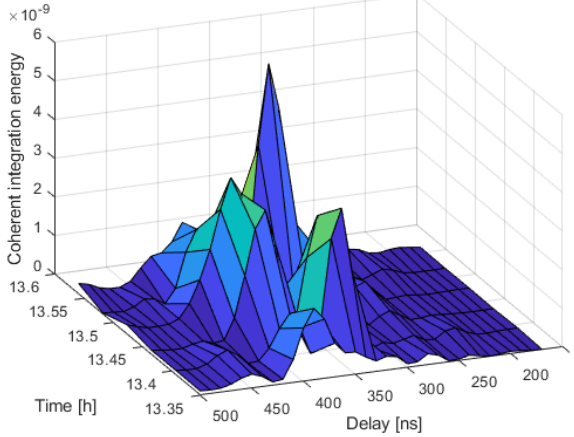

(b) 0° south point, P2, result for 6 measurements using a 2.5 min measurement period.

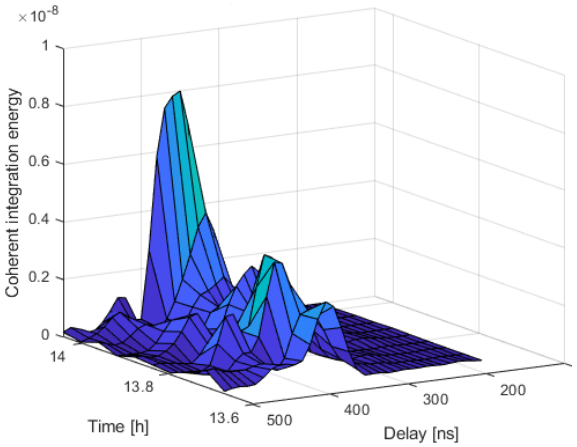

(c) 15° south-east point, P3, result for 10 measurements using a 2.5 min measurement period.

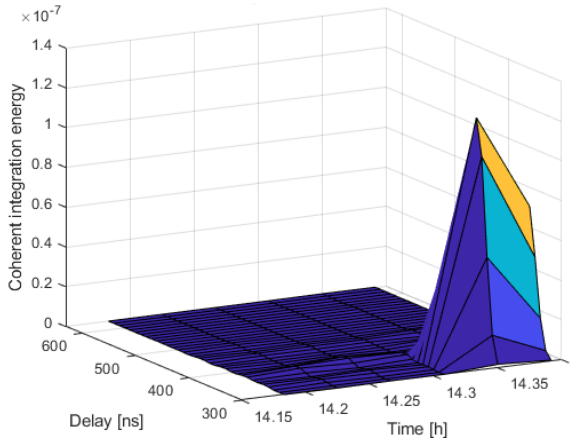

(d) 47° down point, P4, result for 6 measurements using a 2.5 min measurement period.

Figure 4.27: Time-delay map short time series of the measurement points P1, P2, P3 and P4. All measurements were obtained using a coherent integration time of 50 ms. Mind the time and delay axes directions and note the differences in energy of the plots, especially that of (d). The first four measurements of (d) also contain correlation energy output on the order of 10^{-9} for about the same delay as the dominating large peak of its last measurements.

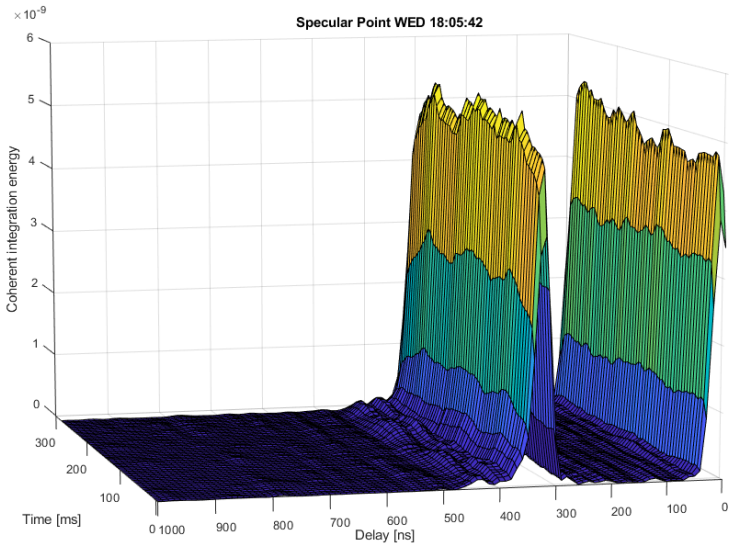

(a)

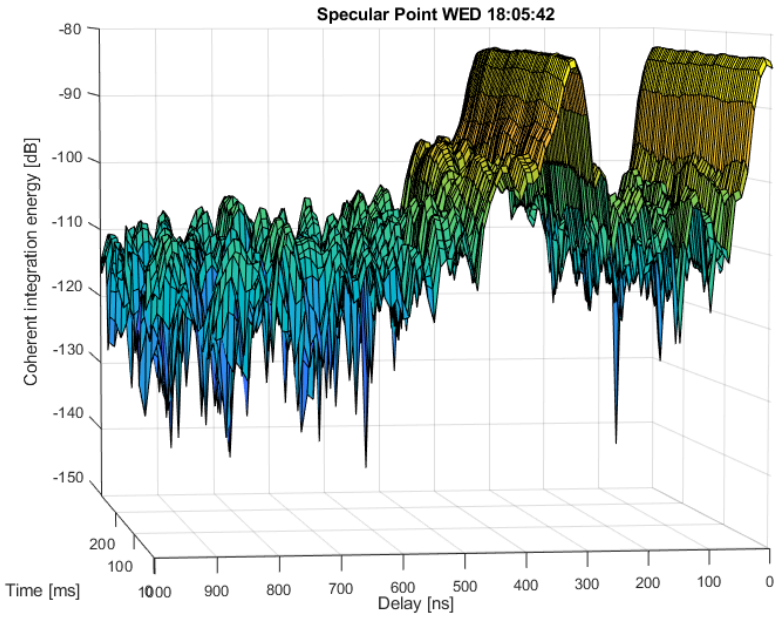

(b)

Figure 4.28: The delay-time map result of the Grimeton P1 (specular point) scattering environment measurements, in a) and b) shown in linear and dB scale respectively. A coherent integration time of 50 ms was used to obtain this result. Note that the energy value is relative and not calibrated, hence it is not being presented in dBm.

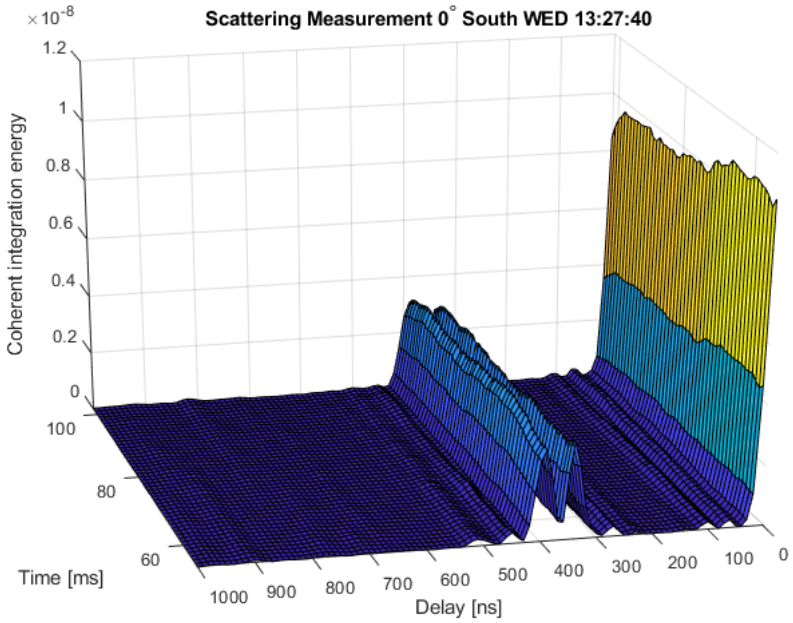

(a)

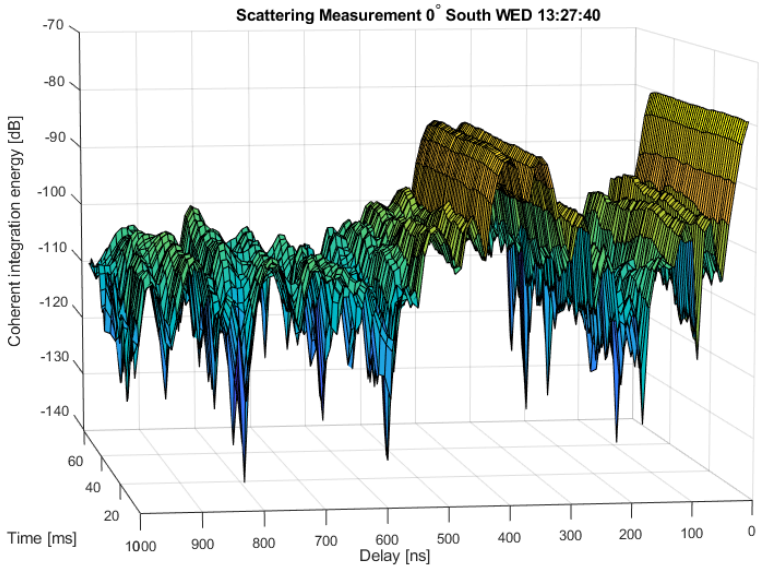

(b)

Figure 4.29: The delay-time map result of the Grimeton P2 (0° south point) scattering environment measurements, in a) and b) shown in linear and dB scale respectively. A coherent integration time of 50 ms was used to obtain this result. Note that the energy value is relative and not calibrated, hence it is not being presented in dBm.

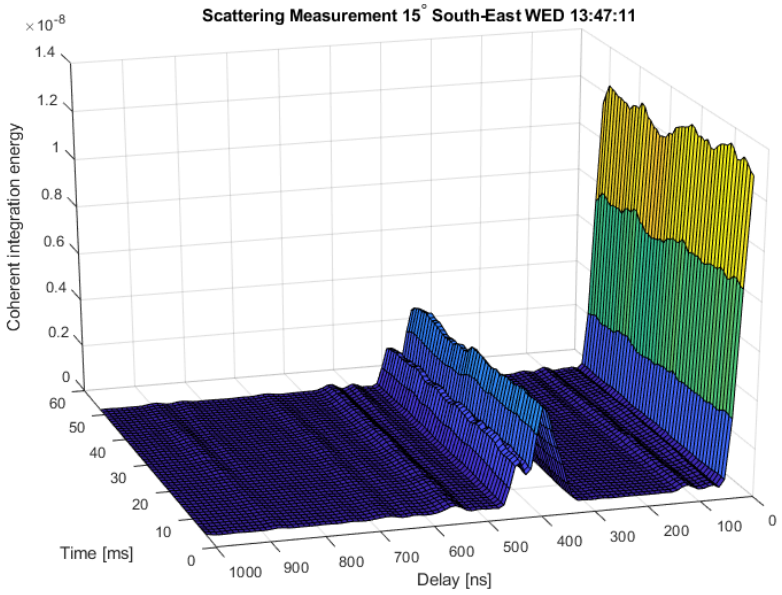

(a)

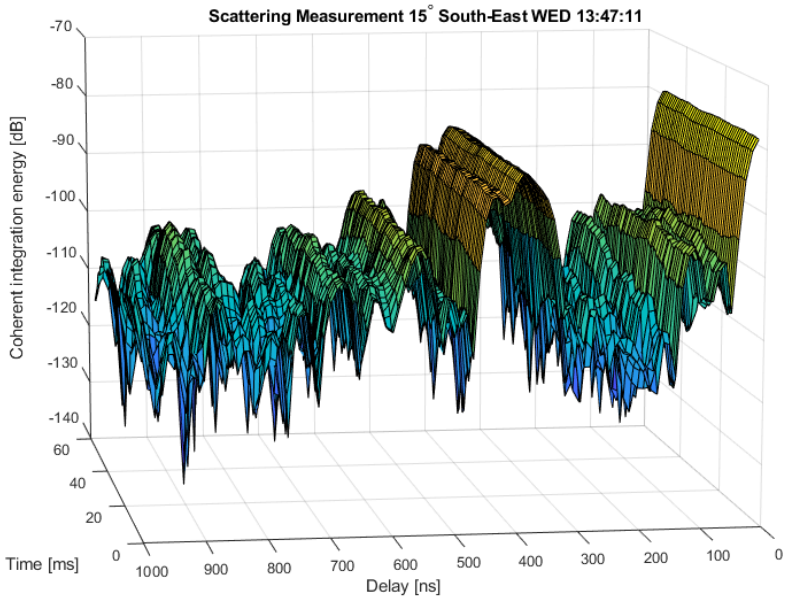

(b)

Figure 4.30: The delay-time map result of the Grimeton P3 (15° south-east point) scattering environment measurements, in a) and b) shown in linear and dB scale respectively. A coherent integration time of 50 ms was used to obtain this result. Note that the energy value is relative and not calibrated, hence it is not being presented in dBm.

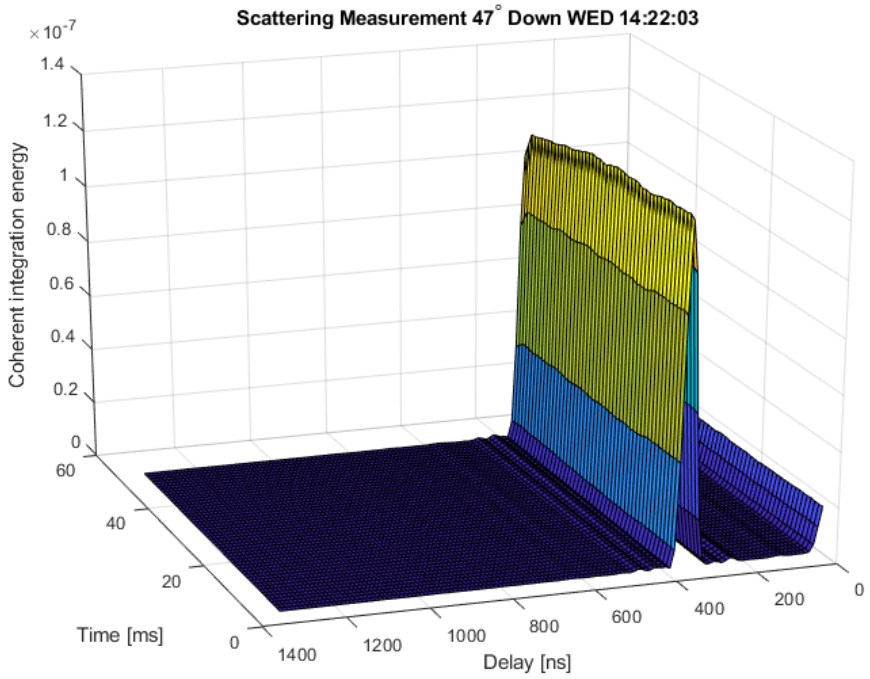

(a)

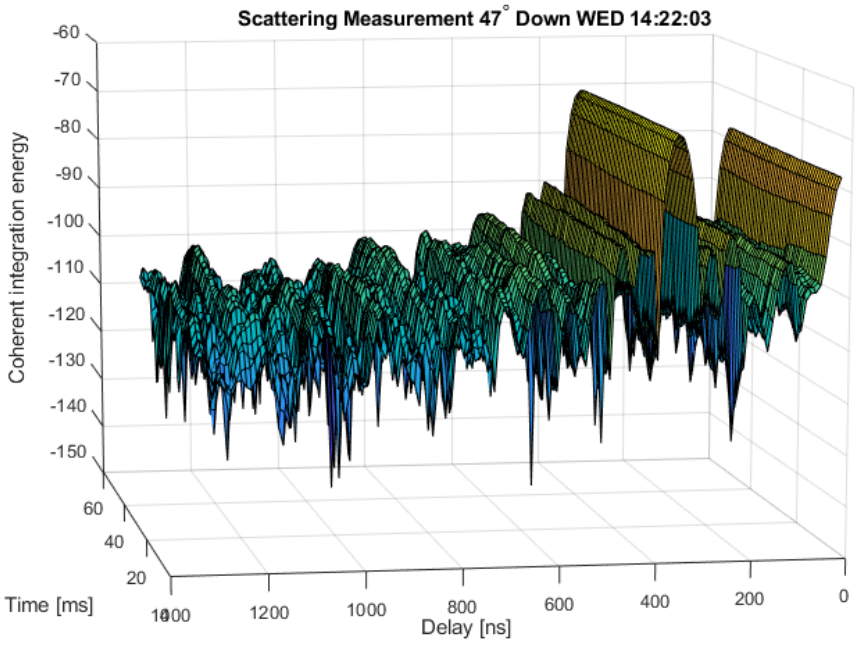

(b)

Figure 4.31: The delay-time map result of the Grimeton P4 (47° down point) scattering environment measurements, in a) and b) shown in linear and dB scale respectively. A coherent integration time of 50 ms was used to obtain this result. Note that the energy value is relative and not calibrated, hence it is not being presented in dBm.

4.6.3 Specular point measurement time series

Measurements taken at many different points, or during a continuous sweep of the antenna beam over the field, would have been preferred to be acquired to infer statistical certainty of the relative soil moisture by non-coherent integration. But this would have required convenient control and movement of the antenna setup, which was outside of the scope of the resources available for this experiment. Also, the high-altitude workers could not work during both day and night due to decent work rights and experiment budget limitations. In addition to this, any change in soil moisture levels was expected to occur at a quite slow (hours) rate and its main relative difference between day and night. Therefore, it was decided that a point measurement time series should be performed to try to detect any relative changes in soil moisture at that very point (or rather area) of interest. The point was chosen as the specular point P1, which was described in the previous subsection. It is worth mentioning that at least two days of time series was planned for, but due to unknown initial problems with the installation during the first two of the four days of the expedition only one day and night could be measured. As if this was not enough, a power outage unfortunately occurred slightly after midnight, interrupting the measurement. Additionally, this stationary point time series measurement may reveal behaviours of the system worth analysing to indicate its performance.

The collected specular point time series measurements are shown in Figure 4.32. As can be seen in the figure, it is compiled from five measurement time series chunks. A clear signal is prominent at the expected delay line of 330 ns and it is seen to change over time. Due to the time series measurements over all being short and incomplete, it is hard to extrapolate any actual soil moisture dependence of the correlation peak energy from this result. This especially since the weather was steadily clear during the time interval of the measurements and that the dawn hours, where morning dew was suspected to affect the signal, was lost due to the power outage. Although, what is still of interest to observe in this context is the energy peak's behaviour over time. Figure 4.34 presents the real and imaginary parts, respectively amplitude time-delay maps from the third measured time series. It indicates at least one or possibly two frequencies that affects the correlation magnitude, since a suspicious sinusoidal signature with a period of 30 minutes is visible. A Fourier transform of the 330 ns delay line (i.e. that of the peak) confirms this behaviour, as shown in Figure 4.34a, where a present frequency of about 2 rotations per hour is detected. Also, a frequency-time map centred around the 330 ns delay line, shown in Figure 4.34b, indicates the oscillations to not be present due to Doppler effects (e.g. by the sway of the tower causing periodical velocity alternations). The cause of this rotation is up for discussion, if it was some hardware effect or due to some environmental reason such as multi-path and the sway of the tower.It is required to understand and model or avoid the cause of this kind of interference to be able to extract any calibrated soil moisture measurements using this kind of point time series. This might not be a problem for a measurement system in movement sweeping over and combining many resolution cell areas.

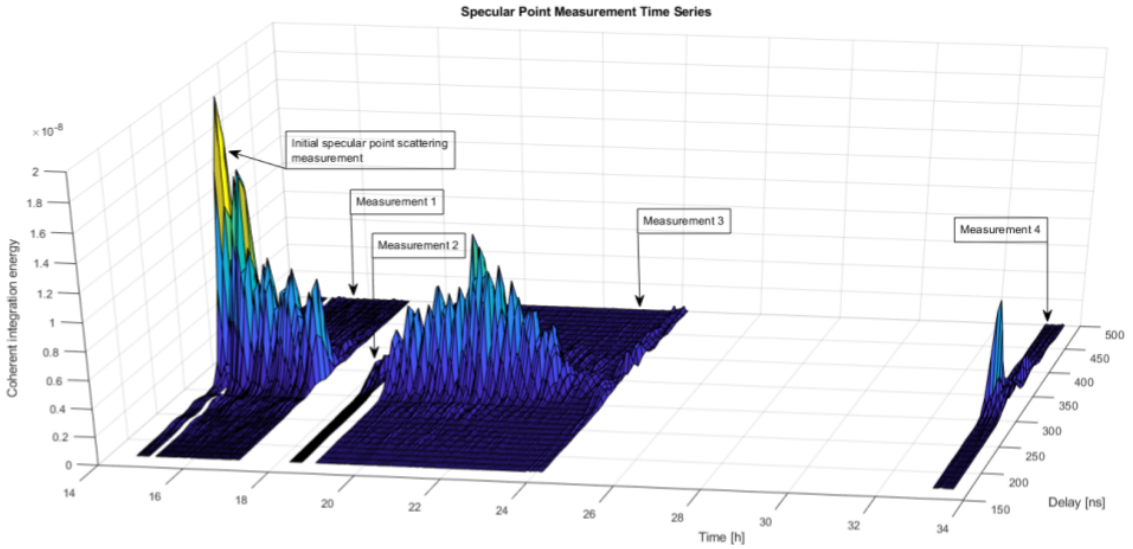

Figure 4.32: The delay-time map result of the collected specular point time series measurements at Grimeton, shown in linear scale. Unfortunately, a power outage at midnight interrupted the measurements.

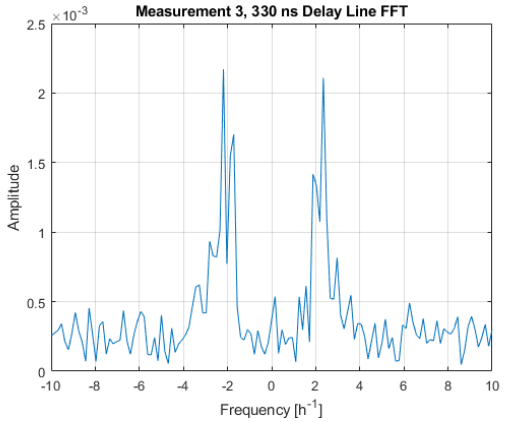

(a) FFT result of the 330 ns delay line.

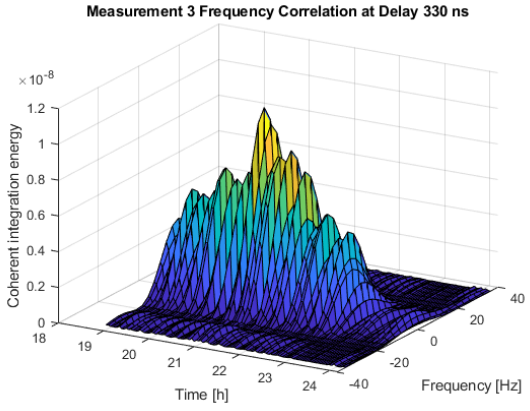

(b) Doppler-time map computed on the 330 ns delay line.

Figure 4.33: Frequency analysis of the Measurement 3 time series 330 ns delay line, as extracted from the data shown in Figure 4.34.

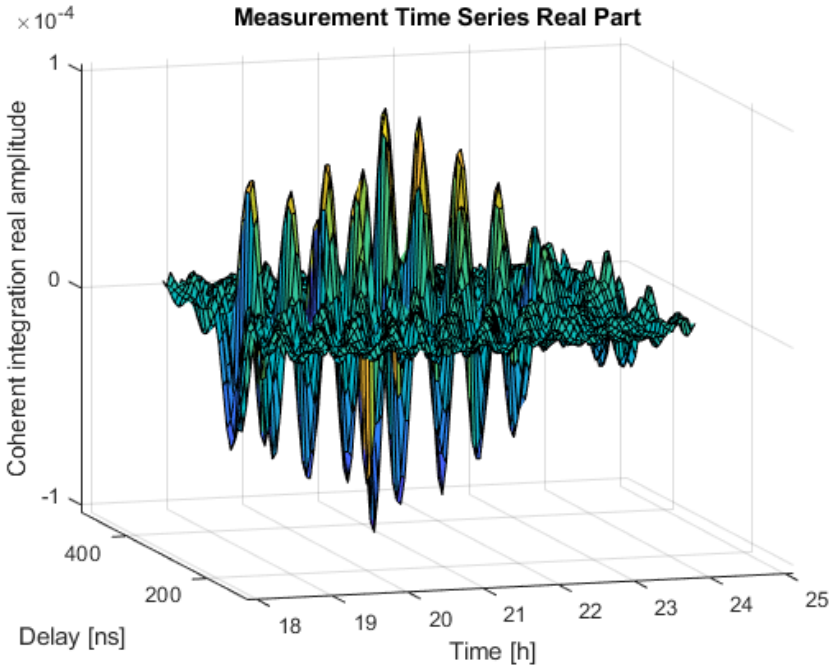

(a)

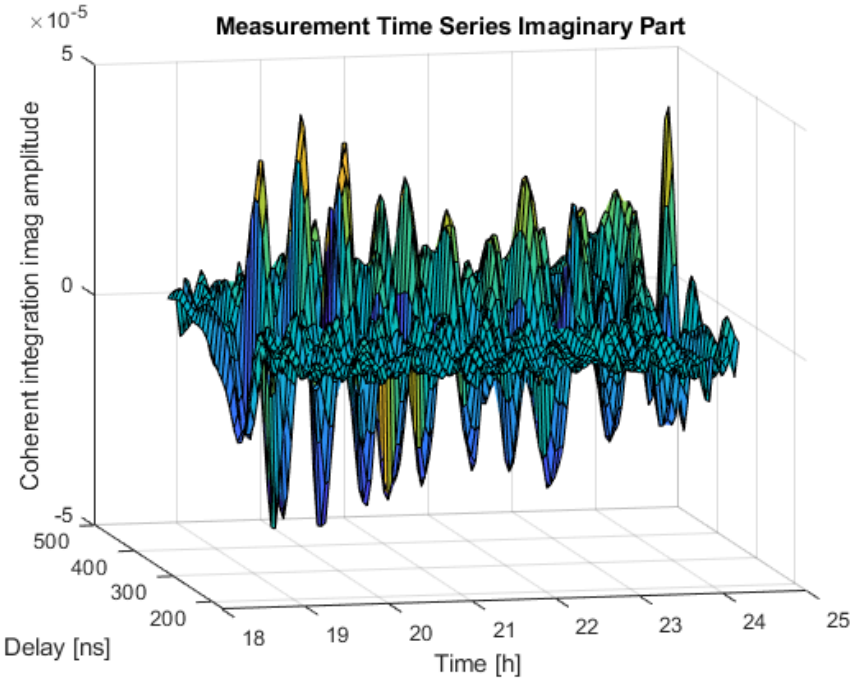

(b)

Figure 4.34: The delay-time map amplitude of the Grimeton measurement 3 time series, figures a) and b) shows the real and imaginary parts respectively. A coherent integration time of 50 ms was used to obtain this result.

5

Discussion of Results and Future Prospects

5.1 Experiment Discussion

The experiment system implementation performance, models validity and measurement results are discussed in this section. This is also connected to argue the prospects of potential future Ku-band TV-DBS PARIS products. This section can be seen as a direct continuation of the content presented in the previous chapter.

5.1.1 Performance of the implemented system

It is of relevance to discuss to what extent the designed system works as intended in practise. First and foremost, a real signal was indubitably detected by the system in the both zero-delay tests as well as at each of the measurement points P1, P2, P3 and P4. The fact that the signal was detected at the expected delay line region for each of the measurements and that no sporadic energy peaks on a similar order of magnitude was seen in the measurement time series is supporting this conclusion. The possibility of this being caused by the system detecting a false signal, in that case due to reflections or coupling of the direct path signal inside of the hardware or some error in the software processing, can hence be neglected with evident certainty. The results of the laboratory and simulation system verification tests are also supporting this conclusion, since they showed the function of each of the system components as well as the system as a whole to not deviate noticeably from that intended.

However, the considerably slow oscillation of the signal peak, which is clearly seen in the time series measurement, is raising some alarming signs since the cause of its presence is not obvious. The important question it raises is if it is caused either by internal effects in the measurement system or by some unforeseen environmental effects, such as multi-path of the signal in combination with a small sway of the antenna tower. If the first case is true, i.e. that the signal should not actually contain this periodic behaviour in these measurements, the system implementation suffers of some serious problem. Anyway, the about half an hour time series of the balcony expedition zero-delay test result shown to the right in the screenshot of the software control and automation application (Figure 4.16) does not show any large change of the signal peak during that time period. This indicates the signal oscillation to not be caused by internal effects of the system itself. Hence, it is seen as more probable to be caused by external environmental effects, but more extensive testing would be required to fully verify this. It could e.g. be that the oscillation is

actually faster than that of the measurement period, but that it due to aliasing effects appears to be slow. It would then need to be slow enough to look approximately constant on the scale of 300 ms, since it is not seen in the small time-scale coherent delay-time maps of the measurements. The measurement period was faster at the balcony zero-delay test than at the Grimeton expedition time series measurements (since the coherent integration time was smaller and hence the processing faster), which then could cause the oscillation to alias to an approximately constant level in the time span of half an hour. This is a bit far-fetched, but the possibility still cannot be excluded. Unfortunately, time series measurements of some different points of interest, such as the more diffuse scattering points P2 and P3, could not be done due to time and budget resource limitations. While that would have been interesting to perform for many reasons, it could also have provided clues to determining the source of the oscillations.

Anyway, another aspect of the designed system is the efficiency of both the hardware and software implementation. There can be quite some improvement made regarding both of these when considering moving on to a more dedicated reflectometry system product. The hardware implementation is very spacious and it requires quite some instruments and availability of power outlets to run properly. In addition to this, the setup of the antennas is not very agile, which is limiting the area possible to measure at. Redirecting the antennas is also required to be done manually, which is a limiting factor since it is sought for to sweep over an area to obtain many independent measurements. This then especially if regularly occurring autonomous measurements of an area was wanted. It can also be noted that smaller (less directive) antennas most probably can be used and still acquire a good signal. The coverage of the measurements would then be improved. The use of the oscilloscope for just sampling the signals is not optimal either. It limits the coherent integration capabilities by its channel memory depth (even if it proved enough to detect a good signal) and its communication speed with the PC is definitely a bottle-neck. On the other hand, the software processing implementation in MATLAB is an even more limiting factor in terms of processing time, then limiting the rate of possible measurements. A micro-controller or FPGA implementation of the signal sampling and processing would greatly improve the measurement rate. To summarise, the implementation could with advantage be improved by: designing a dedicated PCB with all the hardware components, which then also might run on a battery; constructing an agile and preferably autonomously sweeping platform for the reflected path antenna; implementing the DSP system on a microcontroller and/or FPGA(s).

5.1.2 Validity of the theoretical system models

The experimental results are within the ballpark of what is expected from the theoretical models, which is improbable to be just a coincidence. Their similarity to the output observed from the signal input simulation verification test, as seen in Figure 4.20, is evident. The theoretical models are hence considered to overall characterise the experiment setup quite well. However, it is important to note that the theoretical models (as presented in the pilot study) was based on quite some assumptions and

approximations for the simple case of performing a measurement when observing the specular reflection point.

The models could with advantage be extended to include more precise approximations and assumptions, to provide proper energy scaling factors for the non-coherent integration of measurements. This might be required due to the resolution cell areas differing in size dependent on distance and angle to the measurement point, the receiver antenna radiation pattern providing different gain depending on the angle to the point and the surface scattering being (on average) stronger in the forward direction than in the other directions. Resolution cell area computations would then also need to be included for several delay line cells and not just the one in the centre.

The main effect that is of especial importance to characterise well in the models is that of the surface scattering. This is also one of the trickiest effects to model accurately, while being crucial for the system measurement capabilities. The assumption of purely diffuse scattering being present does not seem to hold for what can be seen at the measurement points, but the scattering is still far from specular. This is indicated by the results seen at the specular reflection measurement point P1, where a single dominant energy peak is observed at the delay corresponding to that of the specular point centre, compared to that of measurement points P2 and P3, where two peaks of similar energy is seen within a delay corresponding to that of the illuminated area of the antenna. The scattering is from these few measurements hence seen to act as a combination of specular and diffuse sorts, but with a possibly considerable diffuse part. Although, further measurements would be required to evaluate the scattering characteristics properly when observing a point from any direction.

5.1.3 Prospects of a Ku-band TV-DBS agriculture soil moisture PARIS

There are no indications that a dedicated soil moisture measurement PARIS using Astra 4A opportunity signals should not be possible to implement. On the contrary, the observed signal strength in the results makes it actually seem promising. Then, of course, more questions remain to answer than what has been found out through this experiment. The main inquiry is to determine how well relative soil moisture levels are measurable using this technique, then including an extensive analysis of the measurement uncertainty. This would be accomplished by performing such measurements experimentally and presenting the results, which was unfortunately not successfully done in this experiment due to the circumstances. But as noted, the results presented are still pointing in favour of relative soil moisture measurements being possible.

While the specific system implemented in this experiment is aimed for an initial proof-of-concept study solely, further developments of the design could create a foundation for future products using this technique. Three main thought product area approaches could be a stationary installation on a high point overlooking the area it should monitor, a drone-based (possibly constellation) measurement system and a spaceborne LEO small-satellite reflectometry constellation. Each of these

product areas has their pros and cons regarding limitations in the measurement capabilities of the technology as well as the scientific and industry market interests. If allowing one self to speculate in the prospects of these product areas, some general implications can be argued for.

First, a stationary PARIS installation would be considerably easy to install on e.g. a radio/TV mast or even wind turbine, then also requiring low maintenance. It would thus be cheap to start up, especially in comparison to launching a satellite constellation. This stationary installation would allow for few limitations regarding the use of antennas, technology and power consumption, but a portable-friendly and energy self-sufficient product is of course advantageous. Small wide-beam antennas might be used since the absence of movement in the system would allow for very long coherent integration times and hence a large such gain. Although, for the same reason there would be no Doppler lines present and hence fewer resolution cells per area and measurement compared to a what could be obtained by a system in movement. The system would allow for continuous monitoring of a specified area, but on the other hand have a limited coverage on the order of some kilometres radius from the receiver. Possible stakeholders for this kind of system are seen as either individual farmers investing in their own monitoring system or governmental departments responsible for e.g. flooding disaster warning in areas prone to such risk.

Secondly, a drone-based soil moisture measurement PARIS would put more demands on the technology implementation. For the system to be carried by drones, it would be limited to using considerably small antennas, having a reasonable power consumption as well as being lightweight, agile and compact. The start-up cost of this system would be greater than that of a stationary installation, due to the both larger maintenance demands and technological complexity of the system. The measurement capability would be quite large in coverage (depending on possible flight distances) with a monitoring rate at the order of hours or daily basis, depending on the demands. The relatively slow movement of the drones (as compared to that of a satellite) could allow for a relatively large coherent integration time and hence gain, while still providing Doppler lines enabling a large number of resolution cells per area and measurement. The main stakeholder for this kind of system is seen to be the agriculture industry.

Indications of how promising this system case is can be acquired by extrapolating the reflectometry system models of the Grimeton experiment to approximate that of an imagined drone setup flying at 1 km height at a speed of 50 m/s. If assuming a sought ground footprint sweep width of about ± 1 km, this could be achieved by using a 10 dBi gain antenna, which thus has a beam width of about 50 °, and aiming it at a 25 ° depression angle. Then, if a coherent integration time of 0.2 s and a resolution cell area of approximately a radius of 100 m is allowed, the resulting expected SNR would be about 6 dB. Worth noting is that the size would be very small for this kind of Ku-band antenna (on the order of a centimetre) and a single drone might thus potentially carry several antennas or a phased array antenna, allowing for digital sweeping of the ground footprint. This product does thus actually seem quite realistic. Of course, additional signal processing tricks might be possible to implement to improve the signal strength or measurement statistics even more

(since many TV-channel bands are available from the same signal source and thus might be exploited to yield independent measurements simultaneously of an area if they are separated in frequency by at least a coherence bandwidth). This especially when combining resolution cells in the signal processing to create larger resolution cells, gaining SNR on having a larger radar cross section area, which is needed in this product case, also essentially wasting perfectly good bandwidth.

Lastly, a thought spaceborne LEO small satellite reflectometry constellation would work very similarly to the imagined drone case in terms of measurement capabilites, but at a much larger scale. The main gain of such a system product would be a very large coverage of measurements and possibly fast revisit times, depending on the number of satellites in the constellation and their orbit. The implementation of the product, including antennas, should fit and run on a small satellite and are thus limited in size and power consumption. The start up cost of the system would be very expensive, but surely still far from as expensive per satellite as a traditional active reflectometry system. The seen stakeholders would again for this product case be the agriculture industry, governmental departments responsible for e.g. flooding disaster warning or insurance companies.

It is also of relevance to indicate how realistic this product case is, which again can be done by extrapolating the Grimeton experiment models. Assuming an orbit at a 500 km height above the Earth surface and a speed of about 10 km/s and a sought resolution cell area corresponding to a radius of 10 km, a coherent integration time of 0.5 s and a 19 dBi gain antenna aimed in at a depression angle of 70 °, the resulting expected SNR would be 5 dB. The antenna would then have a size on the order of 8 cm and a beam width of about 18 °, resulting in a ground sweep footprint of about ±84 km. Although, it can be argued how realistic such a long integration time is for a system moving at this large speed. While the resolution in this case is far from fantastic, the system might very well be implementable. Again, a phased array antenna might prove advantageous, while the antenna does definitely need to be larger than that of a drone product. Also again, some further thought could be put into possible signal processing tricks preferably exploiting the available bandwidth of the signal.

5.1.4 Encountered problems - solutions and limitations

While designing and performing the experiment there was a number of issues encountered and in a manner solved. To review all of them is not plausible but the most relevant details are briefed in this section.

When designing the hardware one of the first issues noted was due to the mixer, filters and sampling, as the signal needs to sampled around base-band. Due to the mixer being a physical (*real*) mixer the signal cannot be complex (i.e. asymmetric in frequency domain) and hence the signal was to be filtered to remov lower frequencies to avoid issues from this. Also, the higher frequencies have to be filtered to avoid aliasing when sampling. The anti-aliasing filtering was not a big issue but since the wanted signals after the LNB where at 1.881 GHz and 1.919 GHz it was not possible to make a sharp enough filter to remove the lower frequencies before the mixer.

The implemented solution was to construct a double-conversion superheterodyne

receiver but to place the two frequency bands on top of each other in the output IF. This was confirmed both in theory and simulation to not have any notable negative effect on the correlation. By doing this the unwanted frequencies ended up in the rejection band of the anti-aliasing filter prior to the sampling. Also, an SNR loss was thus avoided due to the signal at the output IF being the sum of two signals and noise bands and not just one signal and two noise bands (at best, if no other interfering signal than from Astra 4A would be present).

As the hardware partially had to be installed at a high altitude 120 m we got a high-altitude climbing certificate, but during the training we were made aware of the rules regarding employer responsibility which complicated things legaly. Hence the solution was to hire high-altitude personnel (Oskar and Julian), which we were allowed to do thanks to Patrik Sandin having faith in our experiment. This provided the ability to install the equipment up in the towers. Julian and Oskar did great even though they did not have any prior knowledge of microwave hardware, which was challenging when we had to perform troubleshooting by phone from ground to tower.

Once the installation was in place the hardware was not fully functional for the first two days. At first neither of the two signal sources provided any signals, one of them had a faulty cable that was easily fixed. After this was fixed one signal chain provided with a signal while the other did not even affect the noise floor. After carefully looking through every part of the system it was deemed to be the larger antenna or LNB, it was solved by taking down both antennas to the ground, swapping the LNBs and wrapping the LNBs in tin-foil. It is unknown what helped, as neither action should have made a difference but after doing this it worked. In conclusion, it was caused by "microwave ghosts".

After the troubleshooting the system was fully operational and it was clear that the system was not only working but also performed well. This lasted until about midnight, where a short power outage unfortunately occurred (which is very rare). This triggered the residual-current circuit breaker in the tower thus cutting the power to the system. This caused the main part of the time-series to be cut. Sadly there was no time to redo this part of the experiment, but the collected data still provided a lot of useful information.

These previous issues all where direct and something we encountered while working, but the most challenging part was clearly the scope of the experiment which was somewhat large for a thesis. As we wanted to perform the experiment, we were forced to divide the work and trust that other to perform the tasks. Responsibility of budget management, contacts and hardware was left to Frans-Erik while the pilot-study, physics, signal processing and software was left to Patrik. This worked out well in the end, but the amount of times where the sheer amount of work almost proved too challenging was not few.

5.2 Connecting passive reflectometry applications prospects to seen demands/needs

The main applications considered in this thesis revolve around altimetry, soil-moisture, vegetation parameters (height and bio-mass), cryospheric applications and ocean wind. Among these the soil-moisture was chosen as an application with large room for improvement, possible market (albeit possibly many costumers) and a wide array of possible demands that could be met. But there was another reason for soil-moisture measurements was chosen as such systems often uses approaches where it identifies the permittivity, which makes the data usable for other applications too.

Next considering the possibilities, there are a lot of reports showing the possibilities of P-RAS and for some applications such as soil-moisture there are signs that show a potential demand for the data too. A conclusion that a ground or air based system could meet some of those demands can be made using our experiment results but to make the same conclusion with any assurance for a satellite based system would as previously stated require a more through survey. A satellite based system could provide large improvements in coverage and possibly have a good revisit time, this could have an edge towards a drone or ground based-system as the system once in orbit could provide with a large amount of data.

In the case where a satellite based Ku-band system would not be possible a SOOP with lower carrier frequency would solve the issue. The prospects of each system are heavily dependent on the amount of sources available but there could be interesting opportunity sources in the S-band, which could provide an interesting alternative to the current GNSS-R systems.

5.3 Regarding exploitation of sub-orbit opportunity signals

Telecommunication constellations like the 7500 planned V-band very low Earth orbit (VLEO) Starlink satellites was an interesting source to investigate if it might be possible to utilize for reflectometry purposes. This is due to the so far scarcely populated and hence interesting V-band frequencies, the considerably large bandwidth of those signals and also of course the pure number of signal source satellites just flying around, waiting to be exploited.

Although, there are complications towards sub-orbit opportunity signals and the fact that the satellite constellation is located at a lower orbit than that thought suitable for a reflectometry mission implies the interferometric approach to simply be impossible to apply, since there will be no direct path signal. This leaves the regenerative approach, but this requires the signal and its precise time of transmission (to solve the position in space of transmission) to be known. If the signal preamble is known, as it might very well be, for each Starlink satellite it might be used for regenerative detection. Also, if the SNR is good enough as well as the frequency response of the reflection considerably flat or possible to equalize, its pilot message might be demodulated and its information used to identify the source satellite. All

good and speculative so far, but the pilot information message will probably not contain precise (if any) signal transmission time stamp. The transmitting satellite position then cannot be solved for and the reflectometry measurement then not be mapped to resolution cells on the Earth surface. Furthermore, the telecommunication satellite signals are of a bursty nature and the signal may therefore not be tracked continuously to yield a solution.

Reflectometry using this setup does hence not seem fruitful if the unknown time of transmission parameter cannot be solved for somehow. Although, if the concept of a constellation consisting of many small reflectometry satellites can be allowed to play with, there might be a more or less possible solution. The proposal is namely this - if two or more reflectometry satellites both detect the same signal, they can combine their correlation peak delay measurements using a common time reference to yield a delay difference which may solve for the unkown time of transmission. With more reflectometry receiver satellites, an arbitrary number of delay difference measurements might be used to more precisely solve for this parameter. This method is, as said, a mere speculation, but in the prospects of a small satellite reflectometry mega constellation system it might be of interest to consider the possibilities of such techniques.

5.4 Interesting further studies

As this was a simple Master thesis project it left large parts unexplored and hence there are possibilities for further studies that complement these points. Due to the time and resource limitations, there was not much optimization done besides initial estimations and calculations. This could be furthered by optimizing some parts of the system such as antenna size, optimize the SNR and illuminated area. Another optimization point could be choice of carrier frequency with regards to depth of interests depending on the applications, since penetration depth is frequency dependant.

One large simplification was that the project did not implement it with the goal of making it fully real, there were three main points missing. Firstly, all digital signal processing in post-processing (in contrast to a real time system (RTS)), due to the immense raw-data-size a real system would real-time process the data to reduce the size. Such an implementation could be realised by using a software defined radio (SDR) with an inbuilt field programmable gate array (FPGA), this would solve most of the hardware requirements.

Also, no complete forward and retrieval models were derived, to extract the physical characteristics from the measurements, i.e. measure soil moisture. This could be relatively complex as the system have many parameters, but using known soil-moisture points as calibration for the system would simplify it largely.

Lastly on the path of building a real-system would be using a non-static system, i.e. having moving parts to introduce a Doppler shift. This could be done in multiple ways; using a moving source or placing the recorder on an air- space- borne platform.

To test many general opportunity signal sources prospects for soil moisture measurements, an experiment could be defined as the following. On top of two towers at a significant height (more than 60 meters) and distance in between each other,

a transmitter and receiver could be installed respectively. The transmitter could be designed such that it generates a sought opportunity signal copy to investigate and reflect it on the ground area in between the towers. The distance in between the towers should then preferably be such that to resolve a significant area in the processing. This would allow for testing of the signal prospects in a more controlled environment, but testing the real source directly would of course be more desirable in a proof-of-concept campaign.

6
Conclusion

6.1 Literature Study Conclusion

A literature study has been performed of the principles, techniques, applications and needs of passive reflectometry and scatterometry. The principles can be concluded to consist of some opportunity signal source families identified (GNSS, DBS, mobile communications satellites and speculatively also active remote sensing systems) as well as a compilation of signal properties, EM wave propagation and scattering effects, bi- and multi-static radar theory, geometry and the DDM result. It also summarises some noise and interference issues. Following this, four identified techniques are concluded - the regenerative, reconstructive, interferometric and partial interferometric approaches respectively. Furthermore, the altitude, soil moisture, vegetation parameter and cryosphere measurement applications are covered. The seen needs of such applications are mainly based on soil-moisture applications. Some of those needs are forest fire, drought and flood early warnings together with soil-moisture mapping for agriculture and insurance purposes.

6.2 Experiment Conclusion

A passive reflectometry experiment has been defined and performed. The subject of the experiment was an agriculture soil moisture PARIS using Ku-band TV-DBS Astra 4A opportunity signals. The system was installed at 120 meter height in an antenna tower at the World Heritage Grimeton Radio Station measuring at the surrounding agricultural fields. Before performing the experiment, its expected results were estimated by modelling the measurement setup and the PARIS was designed, implemented and its function verified. The system design and implementation included hardware-wise a RF front-end and software-wise a digital signal processing system and a measurement control and automation application. The system verification included laboratory, simulation and field tests, which assured the expected function. The experiment results show that a clear signal is indeed detected at all of the four measurement points investigated with a SNR of 10 to 24 dB, where an average SNR of 18.5 dB was expected theoretically. Those results also indicated the signal scattering to contain both a significant specular and diffuse part, suggesting that soil moisture measurements might be possible to perform of an area from any direction of observation. The prospects of three main Ku-band TV-DBS soil moisture PARIS products are discussed. Namely, a stationary installation on a height, a drone-carried system and a LEO small satellite constellation. They are all indicated

to be possible to implement, but the third product is considered the most sceptical.

Bibliography

[1] ESA-Science Office, *Mega-constellation coverage*, https://www.esa.int/ESA_Multimedia/Images/2019/11/Mega-constellation_coverage, [Online; accessed 15-July-2020], 2019.

[2] W. Emery, A. Camps, and M. Rodriguez-Cassola, *Introduction to Satellite Remote Sensing: Atmosphere, Ocean, Land and Cryosphere Applications*. Elsevier Science, 2017, ISBN: 9780128092590. [Online]. Available: https://books.google.se/books?id=sZLUDQAAQBAJ.

[3] C. Ruf, C. Chew, T. Lang, M. Morris, K. Nave, A. Ridley, and R. Balasubramaniam, "A new paradigm in earth environmental monitoring with the cygnss small satellite constellation", *Scientific Reports*, vol. 8, Jun. 2018. DOI: 10.1038/s41598-018-27127-4.

[4] M. Martin-Neïra, M. Caparrini, J. Font-Rossello, S. Lannelongue, and C. S. Vallmitjana, "The paris concept: An experimental demonstration of sea surface altimetry using gps reflected signals", *IEEE Transactions on Geoscience and Remote Sensing*, vol. 39, no. 1, pp. 142–150, Jan. 2001, ISSN: 1558-0644. DOI: 10.1109/36.898676.

[5] A. Dielacher, H. Fragner, O. Koudelka, P. Beck, J. Wickert, E. Cardellach, and P. Høeg, "The esa passive reflectometry and dosimetry (pretty) mission", in *IGARSS 2019 - 2019 IEEE International Geoscience and Remote Sensing Symposium*, 2019, pp. 5173–5176.

[6] H. Fragner, A. Dielacher, M. Moritsch, F. Zangerl, P. Beck, O. Koudelka, P. Høeg, J. Wickert, E. Cardellach, M. Wenger, A. Hörmer, R. Zeif, F. Teschl, M. Neíra, M. Semmling, and R. Walker, "Recycling gps signals and radiation monitoring: The two payloads onboard pretty", Aug. 2019, p. 18. DOI: 10.1117/12.2530806.

[7] M. Martin-Neíra, "A passive reflectometry and interferometry system (paris): Application to ocean altimetry", *ESA Journal*, vol. 17, pp. 331–355, Jan. 1993.

[8] J. S. Subirana, J. J. Zornoza, and M. Hernández-Pajares, *GNSS Data Processing Volume I: Fundamentals and Algorithms*. ESA Communications, 2013, ISBN: 978-92-9221-886-7 (two volumes plus CD).

[9] Wikipedia contributors, *Geostationary orbit — Wikipedia, the free encyclopedia*, https://en.wikipedia.org/w/index.php?title=Geostationary_orbit&oldid=975003807, [Online; accessed 29-August-2020], 2020.

[10] Lyngsat. (2020). [Online; accessed 25-July-2020], [Online]. Available: https://www.lyngsat.com/Astra-4A.html.

[11] Wikipedia contributors, *Amazon (company) — Wikipedia, the free encyclopedia*, https://en.wikipedia.org/w/index.php?title=Amazon_(company)&oldid=969193273, [Online; accessed 25-July-2020], 2020.

[12] ——, *Starlink — Wikipedia, the free encyclopedia*, https://en.wikipedia.org/w/index.php?title=Starlink&oldid=969399373, [Online; accessed 25-July-2020], 2020.

[13] W. Rees, *Physical Principles of Remote Sensing*. Cambridge University Press, 2013, ISBN: 9781107004733. [Online]. Available: https://books.google.se/books?id=rAAEAqnzWtsC.

[14] A. Goldsmith and K. (Firm), *Wireless Communications*, ser. Cambridge Core. Cambridge University Press, 2005, ISBN: 9780521837163. [Online]. Available: https://books.google.se/books?id=n-3ZZ9i0s-cC.

[15] J. Anderson, *Digital Transmission Engineering*, ser. IEEE Series on Digital & Mobile Communication. Wiley, 2006, ISBN: 9780471733652. [Online]. Available: https://books.google.se/books?id=VW7%5C_F8qBsEUC.

[16] R. Sullivan, *Radar Foundations for Imaging and Advanced Concepts*, ser. SciTech radar and defense series. Institution of Engineering and Technology, 2004, ISBN: 9781891121227. [Online]. Available: https://books.google.se/books?id=2rjWVC9fZv4C.

[17] G. Box, U. of Wisconsin–Madison. Mathematics Research Center, and W. U.-M. M. R. CENTER., *Robustness in the Strategy of Scientific Model Building*, ser. MRC technical summary report. Defense Technical Information Center, 1979. [Online]. Available: https://books.google.se/books?id=B4jMtgAACAAJ.

[18] National Aeronautics and Space Administration, *Why space radiation matters*, https://www.nasa.gov/analogs/nsrl/why-space-radiation-matters, [Online; accessed 16-July-2020], 2019.

[19] P. Teunissen and O. Montenbruck, *Springer Handbook of Global Navigation Satellite Systems*, ser. Springer Handbooks. Springer International Publishing, 2017, ISBN: 9783319429281. [Online]. Available: https://books.google.se/books?id=93goDwAAQBAJ.

[20] C. Elachi, *Spaceborne radar remote sensing: Applications and techniques*. 1988.

[21] M. Skolnik, *Introduction to Radar Systems*, ser. Electrical Engineering Series. McGraw-Hill, 1980, ISBN: 9780070579095. [Online]. Available: https://books.google.se/books?id=YvsiAAAAMAAJ.

[22] R. K. Raney, T. T. Freeman, R. W. Hawkins, and R. Bamler, "A plea for radar brightness", *Proceedings of IGARSS '94 - 1994 IEEE International Geoscience and Remote Sensing Symposium*, vol. 2, 1090–1092 vol.2, 1994.

[23] H. Carreno-Luengo and A. Camps, "First dual-band multiconstellation gnss-r scatterometry experiment over boreal forests from a stratospheric balloon", *IEEE Journal of Selected Topics in Applied Earth Observations and Remote Sensing*, vol. 9, no. 10, pp. 4743–4751, Oct. 2016, ISSN: 2151-1535. DOI: 10.1109/JSTARS.2015.2496661.

[24] R. Norris, C. Ruf, E. Loria, and A. O'Brien, "Comparison of wide bandwidth conventional and interferometric gnss-r techniques for possible cygnss follow-on mission", in *IGARSS 2018 - 2018 IEEE International Geoscience and Re-*

mote Sensing Symposium, Jul. 2018, pp. 4277–4280. DOI: 10.1109/IGARSS.2018.8517480.

[25] S. Ribó, J. Arco, S. Oliveras, E. Cardellach, A. Rius, and C. Buck, "Experimental results of an x-band paris receiver using digital satellite tv opportunity signals scattered on the sea surface", *IEEE Transactions on Geoscience and Remote Sensing*, vol. PP, pp. 1–8, Jan. 2014. DOI: 10.1109/TGRS.2013.2292007.

[26] P. Ferrazzoli, L. Guerriero, N. Pierdicca, and R. Rahmoune, "Forest biomass monitoring with gnss-r: Theoretical simulations", *Advances in Space Research*, vol. 47, no. 10, pp. 1823–1832, 2011, GNSS Remote Sensing-2, ISSN: 0273-1177. DOI: https://doi.org/10.1016/j.asr.2010.04.025. [Online]. Available: %5Curl%7Bhttp://www.sciencedirect.com/science/article/pii/S0273117710002863%7D.

[27] T. van der Wal and J. Verschoore, *Gnss-r technology: Market analysis*, http://www.mistrale.eu/Publications/reports, [Online; accessed 17-August-2020], 2017.

[28] C. Chew, J. Reager, and E. Small, "Cygnss data map flood inundation during the 2017 atlantic hurricane season", *Scientific Reports*, vol. 8, Dec. 2018. DOI: 10.1038/s41598-018-27673-x.

[29] Wikipedia contributors, *Astra 4a — Wikipedia, the free encyclopedia*, https://en.wikipedia.org/w/index.php?title=Astra_4A&oldid=963912534, [Online; accessed 7-August-2020], 2020.

[30] Unesco, *World heritage grimeton radio station*, https://whc.unesco.org/en/list/1134/, [Online; accessed 16-July-2020].

[31] ITU, *Recommendation itu-r p.676-12 (08/2019) - attenuation by atmospheric gases and related effects*, https://www.itu.int/rec/R-REC-P.676-12-201908-I/en, [Online; accessed 6-August-2020], 2019.

[32] J. Cihlar and F. T. Ulaby, "Dielectric properties of soils as a function of moisture content", 1974.

[33] ITU, *Reflections from the surface of the earth*, [Online; accessed 6-August-2020], 1990. [Online]. Available: %5Curl%7Bhttps://www.itu.int/dms_pub/itu-r/opb/rep/R-REP-P.1008-1-1990-PDF-E.pdf%7D.

[34] Google, *Google maps*, https://www.google.se/maps/@57.1068528,12.3938183,715m/data=!3m1!1e3, [Online; accessed 17-August-2020].